Manuscript in preparation for *Journal of Geophysical Research: Solid Earth*
Special Issue "Ten years after the Wenchuan earthquake: new insights into the geodynamics of the eastern Tibet"

Competing effects of mountain uplift and landslide erosion over earthquake cycles

Gen Li[1*], A. Joshua West[1], Hongrui Qiu[1]

[1]Department of Earth Sciences, University of Southern California, Los Angeles, CA 90089, USA

[*]Corresponding author: Gen Li

Present address:
Division of Geological and Planetary Sciences, California Institute of Technology, Pasadena, CA 91125, USA

Email: ligengeo@gmail.com; ligen@caltech.edu

Key points:

1. Develop a generalized modeling framework evaluating earthquake volume balance considering seismic deformation, landslide erosion and erosion-induced isostacy

2. Comprehensive consideration of earthquake volume balance across varying topographic and seismotectonic conditions

3. Evaluate the overall topographic effect of earthquake cycles in the eastern Tibetan region to be constructive

Abstract

Large earthquakes construct mountainous topography by inducing rock uplift but also erode mountains by causing landslides. Observations following the Wenchuan earthquake show that landslide volumes can match seismically induced uplift, raising questions about how the actions of individual earthquakes accumulate to build topography. Here we model the two-dimensional surface displacement field generated over a full earthquake cycle accounting for co-seismic deformation, post-seismic relaxation, landslide erosion, and erosion-induced isostatic compensation. We explore the related volume balance across different seismotectonic and topographic conditions and revisit the Wenchuan case in this context. The ratio (Ω) between landslide erosion and uplift is most sensitive to parameters determining landslide volumes (particularly earthquake magnitude M_w, seismic energy source depth, and failure susceptibility, as well as the seismological factor responsible for triggering landslides), and is moderately sensitive to the effective elastic thickness of lithosphere, T_e. For a specified magnitude, more erosive events (higher Ω) tend to occur at shallower depth, in thicker-T_e lithosphere, and in steeper, more landslide-prone landscapes. For given landscape and seismotectonic conditions, the volumes of both landslides and uplift to first order positively scale with M_w and seismic moment M_o. However, higher M_w-earthquakes generate lower landslide and uplift volumes per unit M_o, suggesting lower efficiency in the use of seismic energy to drive topographic change. With our model, we calculate the long-term average seismic volume balance for the eastern Tibetan region and find that the net topographic effect of earthquakes in this region is constructive rather than erosive. Overall, destructive events are rare when considering processes over the full earthquake cycle, although they are more likely if only considering the co-seismic volume budget (e.g. the 2008 Wenchuan earthquake where landsliding substantially offsets co-seismic uplift). Irrespective of the net budget, our results suggest that the erosive power of earthquakes plays an important role in mountain belt evolution, including by influencing structures and spatial patterns of deformation, for example affecting the wavelength of topography.

1. Introduction

Mountain ranges are among the most conspicuous landforms at the Earth's surface, and they have global-scale effects including on atmospheric circulation (Molnar and England, 1990; Avouac, 2007; Boos and Kuang, 2010) and the long-term carbon cycle (Raymo et al., 1988; Galy et al., 2007; Torres et al., 2014). The geological processes that build mountainous topography have remained hotly debated (e.g., Kelsey, 1990; Clark and Royden, 2000; Tapponier et al., 2001; Avouac, 2007; Elliott et al., 2016; Whipple et al., 2016). At collisional plate boundaries, thrust-faulting earthquakes are thought to be a major driver of mountain uplift via repeated vertical displacement (e.g., Avouac, 2007; Meade, 2010). However, large earthquakes also cause widespread landslides that collectively generate large volumes of clastic sediment and facilitate erosion of mountains (Keefer et al., 1994; Hovius et al., 2011; Wang et al., 2015; Li et al., 2016; Tanyas et al., 2017). Observations from the 2008 M_w7.9 Wenchuan earthquake revealed that in some cases, the volume of earthquake-triggered landslides can be comparable to or even exceed that of co-seismically induced rock uplift (Parker et al., 2011; Li et al., 2014), demonstrating the significant erosive power of large earthquakes and raising fundamental questions about how seismotectonic activity builds mountainous topography.

These observations from Wenchuan, and similar work focused on the 1999 Chi-Chi event (Hovius et al., 2011), have stimulated efforts to develop a generalized understanding of earthquake volume balance, i.e., the balance between earthquake-induced uplift and landslide erosion. Recent studies by Li et al. (2014) and Marc et al. (2016a) considered how this "co-seismic" balance might vary for earthquakes of different magnitude (M_w), using models for co-seismic uplift and landslide erosion as a function of M_w (e.g., Keefer et al., 1994; Cohen et al., 1996; Malamud et al., 2004; Leonard, 2010; Marc et al., 2016b). Marc et al. (2016a) additionally showed that other factors modulating the total volume of earthquake-triggered landslides, for example landscape steepness and seismic energy source depth, influence the overall volume balance of a single event. Understanding the role of earthquakes in mountain building requires systematically quantifying these dependencies, since the cumulative work of multiple earthquakes contributes to building topography. However, topography responds not only to co-seismic processes (uplift and landsliding), as considered in the work of Li et al. (2014) and Marc et al. (2016a), but also to post-seismic relaxation following co-seismic deformation and isostatic compensation to erosional mass removal (King et al., 1988; Watts, 2001; Molnar, 2012; Huang et al., 2014), as well as inter-seismic processes (Cattin and Avouac, 2000; Vergne et al., 2001; Godard et al., 2004, 2009; Dal Zilio et al., 2019).

Previous studies have quantified the effects of earthquake cycle processes using physical solutions for the mechanical behavior of dip-slip fault systems with layered structures of different rheological properties (e.g., King et al., 1988; Cattin and Avouac, 2000; Simpson, 2014; Dal Zilio et al., 2019). These studies have been able to describe how first-order topographic forms can emerge from repeated earthquake sequences, but they lacked quantitative constraints on earthquake-triggered erosion. This gap can be filled by recent understanding of the earthquake balance problem (Parker et al., 2011; Hovius et al., 2011; Li et al., 2014; Marc et al., 2016a), informed by models describing landslide volumes (Marc et al., 2016b) and observations that landslides are a dominant contributor to orogenic erosion (Keefer, 1994; Malamud et al., 2004; Li et al., 2017). Using this foundation to constrain the erosional term in models akin to that developed by King et al. (1988) promises a holistic, seismologically-based description of topographic growth associated with seismic activity and affords the opportunity for a more complete consideration of the volume balance problem over full earthquake cycles. Such an approach is specifically targeted at resolving questions about the role of earthquakes in building topography, e.g., as expected in settings with high seismic coupling, recognizing that in other settings aseismic processes may also contribute significantly to topographic development (e.g. Vita-Finzi, 2000).

In the present study, we develop a generalized model building on the framework of King et al. (1988) and parameterizing erosion based on a seismological description of landslide volume (Marc et al., 2016b). This model simulates the two-dimensional (2-D) surface displacement field caused by seismic processes over full earthquake cycles, focusing on the end-member case where inter-seismic tectonic loading occurs in the far field and causes minimal transient deformation of the fault zone, as may be the case along the eastern margin of the Tibetan Plateau (see below). We consider that future work could extend our framework to consider settings where inter-seismic loading is important. As developed here, our model allows us to (i) test the sensitivity to relevant seismological and topographic parameters, (ii) distinguish the role of co-seismic deformation, post-seismic relaxation, landslide erosion and erosional unloading-induced isostatic response, and (iii) evaluate how different processes affect the spatial patterns of mass redistribution and thus general topographic form. We are further able to re-evaluate the question of earthquake volume balance across events of different magnitudes, specifically considering the importance of assumptions about the seismological factors most responsible for landslide triggering as well as the importance of the spatial window over which volume balance is calculated (e.g., Densmore et al., 2012). We can evaluate the efficiency of seismic processes in doing geomorphic work, in other words how much of the released seismic moment converts to uplifting or eroding topography, as well as the relative importance of earthquake events with varying magnitudes in the total volume budget. Finally, we contextualize these model results by presenting an analysis of how the volume balance for the Wenchuan event depends on the spatial integration boundaries and seismotectonic conditions. In the context of the Wenchuan event, we model the long-term volume balance over multiple seismic cycles to examine the role of earthquakes in mountain belt evolution at the eastern margin of the Tibetan Plateau. This paper thus links seismicity to landscape evolution, promising better understanding of how fault systems and associated earthquake cycles drive orogenic growth.

2. Model summary, approximations and simplifications

Here we summarize our model setting, framework, and the major assumptions and simplifications taken in this work.

2.1. Fault implementation

We model the lithosphere-asthenosphere system (Figure 1) as an elastic plate (thickness T_e, density ρ_L 2700 kg m^{-3}, Young's modulus E 70 GPa, Poisson ratio ν 0.25) overlying a viscoelastic half space (density ρ_A 3300 kg m^{-3}). Following King et al. (1988), the fault is implemented as a plane (dip θ) extending through the elastic plate into the viscoelastic half space. The upper part of the fault in the lithosphere behaves in an elastic-brittle manner during earthquake ruptures, whereas the lower part of the fault in the viscoelastic half space is set to be ductile over the long term, but acts similarly as the upper part in an elastic-brittle fashion when earthquakes occur (as in King et al., 1988). In our model, we consider that all earthquake events rupture to the surface, and the rupture dimensions and fault displacement are determined using empirical scaling relations with earthquake magnitude M_w (Leonard, 2010). As all earthquakes rupture to the surface, the depth of an earthquake event is then at the bottom of the rupture plane and determined as the product of rupture width and sin(θ). To allow an extensive exploration of earthquakes of different magnitudes, we assume that the fault plane is large enough to accommodate earthquakes over a wide range of magnitudes (up to M_w = 8-9 in this study). We acknowledge that, because earthquake depth varies as a function of M_w and is independent of T_e, there are scenarios in our model when earthquakes occur at depth deeper than the conventional seismogenic zone. Whether these scenarios are physically realistic is debatable. Although it is widely accepted that earthquakes mostly occur in the seismogenic zone (e.g. Scholz, 2002), recent studies (e.g. Jiang and Lapusta, 2016) suggest that large earthquakes can rupture deeper than the seismogenic zone, as the deeper fault extensions into the creeping zone may dynamically localize and weaken under seismically induced shear heating and strain-rate effects. Validating the deep penetration of large earthquakes is beyond the scope of this study, as our main purpose is to provide a setting where the effects of relevant parameters (e.g. T_e) can be fully explored. Thus in our model, we allow earthquakes to occur at depth independent of T_e, recognizing that some deep-penetrating events may or may not be physically realistic – but also realizing that the deepest earthquakes are likely to be least relevant to landslide triggering (see below). This setting allows us to use a computational simple analytical solution that approximates post-seismic deformation (Savage and Gu, 1985).

2.2. Processes operating over earthquake cycles

Our modeling framework accounts for tectonic uplift, landslide erosion, and erosion-induced isostatic compensation over full earthquake cycles. Tectonic uplift is driven by inter-seismic loading and expressed as seismic and aseismic deformation (King et al., 1988; Cattin and Avouac, 2000; Avouac, 2007; Simpson, 2015). The seismic component of deformation is a combination of the deformation caused by strain release during earthquakes (co-seismic) and the corresponding lithospheric rheological adjustment (post-seismic relaxation and isostatic response to co-seismic deformation) over inter-seismic periods (King et al., 1988; Simpson, 2015). Aseismic deformation is conceptualized as ductile creeping and loading along the fault plane at a relatively constant long-term rate (Savage et al., 1983; Simpson, 2015). Landslides are triggered co-seismically, and landslide debris is gradually removed out of mountain ranges by rivers between earthquake cycles (Hovius et al., 2011; Wang et al., 2016; Croissant et al., 2017). This landslide-induced erosional unloading causes isostatic response, which operates over inter-seismic time periods and works to compensate volume loss (Molnar, 2012). These processes are all time-dependent; for example, export of landslide-derived sediment and isostatic response are not instantaneous but occur over timescales of thousands of years or longer. In our model, the overall volume budget of these processes is calculated after multiple earthquake cycles (>1000s years to Myrs), to reflect timescales relevant to mountain belt evolution, so we consider only the "end state" and ignore any path-dependency. For computational simplicity and efficiency, we make five further major approximations and simplifications.

Firstly, we simplify the effect of inter-seismic tectonic loading and aseismic slip. Specifically, our model does not account for inter-seismic tectonic loading. The effects of loading on the fault zone depend on its mechanism and spatial scale (Cattin and Avouac, 2000; Johnson, 2005; Simpson, 2015). Finite element modeling of time-dependent viscoelastic deformation shows that when inter-seismic loading is applied from far field at regional scales, there is negligible influence on surface vertical deformation (Simpson, 2015). In this scenario, co-seismic deformation and post-seismic relaxation should accurately describe vertical deformation over earthquake cycles. Our model represents this scenario, for example in the Longmen Shan mountains at the eastern margin of the Tibetan Plateau where the Wenchuan earthquake occurred but limited active shortening was observed from before the earthquake (Zhang et al., 2004; Burchfiel et al., 2008). For regions where inter-seismic loading operates at scales comparable to fault dimensions (e.g. creeping at the fault root below the locking depth) and causes significant surface deformation (e.g., Taiwan and the frontal Himalayas, Cattin and Avouac, 2000; Johnson et al., 2005; Stevens and Avouac, 2015), our model can only constrain the co-seismic and post-seismic components and the related volume balance, but lacks the inter-seismic component related to loading. Future work could add modeling of these inter-seismic processes (e.g. Cattin and Avouac, 2000; Simpson, 2015; Dal Zilio et al., 2019) into our framework, but is beyond the scope of this study.

Besides tectonic loading, we also simplify the influence of aseismic slip during the inter-seismic time period by introducing a deformation partitioning coefficient f that quantifies the proportion of seismically versus aseismically induced deformations over earthquake cycles (Section 3.1; and see Figure 2). We explicitly distinguish this aseismic component because our main goal is to investigate topographic development by seismic processes, and for our purposes, the main distinction is that aseismic processes do not directly trigger landslides while seismic processes do.

Secondly, we calculate the two-dimensional (2-D) deformation fields using analytical solutions that are originally derived for faults with infinite length (Savage and Gu, 1985; King et al., 1988; and Cohen, 1996 and references therein). Such 2-D approaches to model seismic deformations have been applied to several fault-impacted landscapes, for example, the western and central United States and Taiwan, and to subduction zones in Japan (e.g., Savage and Gu, 1985; Stein et al., 1988; Johnson et al., 2005). However, 2-D approaches may lead to uncertainties for real faults with finite length. Notably, King et al. (1988) show that when applying 2-D flexural isostacy models to settings with finite strike extent, the results are accurate within a few percent if fault length is about 10 times of T_e. High magnitude earthquakes should satisfy this rule, for example, a M_w8 reverse fault-earthquake (surface rupture length ~270 km, according to the M_w-fault dimension scaling relation in Leonard, 2010) occurring in a region with a common T_e value of 20 km (Burov et al., 1995; Maggi et al., 2000; Jordon and Watts, 2005; Fielding and McKenzie, 2012). Applying 2-D approaches to single, smaller magnitude earthquakes with shorter fault length may cause larger uncertainties. However, the cumulative deformation of these smaller magnitude events over multiple earthquake cycles may make them suitable for using 2-D models. Specifically, if each smaller event ruptures a different segment of a fault (e.g., the Himalayan main thrust front; Bollinger et al., 2014), over the long-term, the rupture length of each smaller event can add up to reach the full fault length. This scenario can be demonstrated quantitatively, by comparing the cumulative rupture length to the fault length, or the rupture length of the maximum-magnitude event. To do this, we can use the recurrence time of earthquakes of different magnitudes using the Gutenberg-Richter frequency-magnitude relation (Eq.1, Gutenburg and Richter, 1954):

$$\mathrm{Log}_{10}N = a - bM_w \qquad \text{(Eq. 1)}$$

where N is the number of earthquakes with magnitude $\geq M_w$ within a defined time period (taken as 100,000 yr here), and a and b (b chosen as the global average value, 0.9, Malamud et al., 2004 and references therein) are scaling parameters. We then calculate the total rupture length, i.e. the product of earthquake recurrence time and the rupture length for specified magnitude, for each earthquake magnitude bin (ΔM_w = 0.1). The results (Figure 3) indicate that, over the course of 10 cycles of the maximum-magnitude event (assuming maximum M_w = 8, rupturing the full fault length), smaller-magnitude earthquakes can produce a total rupture length 10-60 times of the full fault length, suggesting that cumulatively these smaller events can work to rupture the full fault and form structures with sufficient length, making them suitable to modeling using 2-D approaches.

Thirdly, we assume (near)complete post-seismic deformation over multiple earthquake cycles. Real post-seismic deformation is time-dependent, and assuming the asthenosphere behaves as a Maxwell material, a standard timescale metric is the Maxwell relaxation time τ, typically around 10-100 years (Johnson et al., 2005; Simpson, 2015). Previous studies assume post-seismic deformation approaches completion after ~10-50τ (so ~100-5000 years; e.g., Thatcher and Rundle; 1984; Savage and Gu, 1985; Johnson et al., 2005). Although this timescale may exceed one earthquake cycle, it is well within the range of our timescale of interest over multiple earthquake cycles (1000s years-Myr), so we argue that post-seismic deformation can be considered as (near)complete in our modeling framework. The (near)complete assumption also allows us to take advantage of the analytical solution derived by Savage and Gu (1985), who take a plate flexure approach to approximate the complete time-dependent relaxed-asthenosphere solution of Thatcher and Rundle (1984).

Fourthly, we assume co-seismic landsliding and subsequent fluvial removal of landslide debris are the major mechanisms by which earthquakes drive erosion and we neglect transient changes in landslide propensity and landscape erodibility caused by seismic processes in post-earthquake time periods. Recent studies show that in seismically active landscapes, material strength and its spatiotemporal variations are important in determining spatial and temporal patterns of landslide occurrence (Scheingross et al., 2013; Gallen et a., 2015; Marc et al., 2015). Material strength is a complex function of geological, climatic and seismotectonic conditions. Earthquakes can alter strength, thus modulating landslide propensity and landscape erodibility in post-seismic time periods. For example, Scheingross et al. (2013) found that in the San Andreas fault system, inter-seismic slow-moving landslides cluster near the creeping section but are rare in earthquake-shock parts, suggesting that earthquakes may preferentially remove weak material via landsliding. Thus post-earthquake landslide propensity may be decreased in this scenario. Other studies have observed enhanced landsliding rates after large earthquakes (e.g. in Taiwan, Japan, Paupa New Guinea and Sichuan), suggesting the reduction of material strength following earthquakes. Although landsliding rate increases in those settings, the post-seismic landslides amount to a limited addition (<10%) to the total co-seismic landslide volumes (Zhang et al., 2014; Marc et al., 2015; Li et al., 2016; Fan et al., 2018). Studying landslides caused by two historic earthquakes (1929 and 1968) in New Zealand, Parker et al. (2015) propose that earthquakes can cause damage in landscapes that persists longer than decadal post-earthquake time periods, preconditioning hillslopes for failure in next earthquakes. However, the longer-term (>100s years) effects remain unclear. Geophysical surveys suggest that the weakening and recovery of substrate strength occurs relatively rapidly, i.e., within around 1-10 years following the mainshock, as inferred from changes in seismic velocity (e.g., Brenguier et al., 2008; Gassenmeier et al., 2016). We also acknowledge that earthquakes may affect landscape erodibility (Vanmaercke et al., 2017) and non-landsliding erosional flux, but we expect a minor influence given the dominant role of landslides in sustaining long-term erosional flux in steep mountains (Keefer, 1994; Hovius et al., 1998; Li et al., 2017; Marc et al., 2019). Overall, we expect these factors contribute a minor part to the total earthquake-caused erosional budget compared to co-seismic landslides, but we recognize that they are also important mechanisms by which earthquakes may affect erosion.

Fifthly, we assume complete removal of landslide debris between earthquake cycles. This assumption is mainly supported by observations of suspended sediment load and by modeling studies of bedload transport which both show relatively rapid removal of landslide debris compared to typical earthquake return times (Hovius et al., 2011; Wang et al., 2015; Croissant et al., 2017). Notably, a recent modeling study (Croissant et al., 2017) systematically explored a range of controlling factors on landslide evacuation time in post-earthquake landscapes, including landslide characteristics (e.g. volume, grain size, landslide dam stability, and connectivity to channels), earthquake magnitude, climatic and hydrologic conditions (e.g. mean runoff and discharge variability) and the properties of the fluvial network (e.g. channel width and steepness). They found that across a wide range of conditions, it is the dynamic narrowing of alluvial channels due to landslide input that plays a key role in prompting post-earthquake river transport capacity and setting the landslide evacuation time to be around <10s-100 years. Some other studies, even without considering the dynamic evolution of channel morphology (e.g. Yanites et al., 2010), also suggest an evacuation time of 100-1000 years, i.e., shorter or comparable to the recurrence time for large earthquakes. The assumption that landslide debris is efficiently evacuated is supported by field observations that mountainous valleys accumulate little clastic sediment (Parker et al., 2011; Marc et al., 2016a). However, we recognize that in some settings, such as the central Nepal Himalaya, the relatively short recurrence time for large earthquakes (Bollinger et al., 2014) may lead to persistence of landslide debris within the landscape, violating this assumption. Nonetheless, we approximate seismically induced erosional unloading using the magnitude and pattern of earthquake-triggered landslides. For computational simplicity, we also do not account for the effect of the sedimentation of landslide materials in frontal basins, assuming all landslide sediment are exported and deposited in further downstream areas with minimal influence on fault zone deformation. In general, sedimentation in footwall basins would reduce both local subsidence due to sediment infilling and adjacent hanging wall uplift due to flexural isostatic response to sediment loading (e.g. King et al., 1988; Densmore et al., 2012). However, explicit modeling the effect of local sedimentation requires constraints on the distribution of sediment in subsidence areas, which could be explored in future studies but is beyond the scope of this study.

These approximations allow us to adopt a set of analytical solutions, making it possible to explore relevant parameter space and in the process gain insight into what controls the volume balance of earthquakes. However, unlike fully resolved numerical models of landscape evolution, we do not attempt to simulate the full suite of factors responsible for time-dependent topographic development. In the following sections, we describe in more detail how we model different processes and related deformation over earthquake cycles.

3. Model setup and parameterization

3.1. Tectonic uplift driven by co-seismic, post-seismic and aseismic deformation

Seismic deformation is expressed as the vertical surface displacement caused by co-seismic deformation and post-seismic adjustment (King et al., 1988). We model the co-seismic displacement field using an analytical solution to a 2-D dip-slip dislocation model (Cohen, 1996). Fault displacement and length are calculated using the empirical scaling relations between earthquake magnitude and average displacement (D) and surface rupture length (L_{sf}) for dip-slip fault earthquakes, respectively (Table 6 in Leonard, 2010). To simulate post-seismic relaxation integrated over timescales of >100s-1000s years, comparable to the timescales of multiple earthquake cycles, we adopt a computationally convenient, analytical solution of Savage and Gu (1985), who use a plate flexure approach to approximate the complete time-dependent relaxed-asthenosphere solution of Thatcher and Rundle (1984). This post-seismic deformation solution represents a viscoelastic gravitational solution (Equations 4, 5 and 14 in Savage and Gu, 1985) that accounts for the effect of gravity and the corresponding isostatic adjustment to co-seismic deformation (Thatcher and Rundle, 1984; Savage and Gu, 1985). The net seismically induced rock uplift volume ($V_{up}^{seismic}$) is determined as the sum of local subsidence and uplift, and varies as a function of θ, T_e and M_w (Savage and Gu, 1985).

To account for the uplift volume caused by aseismic processes ($V_{up}^{aseismic}$) and link this quantity to the seismically uplifted volume, we introduce a partitioning coefficient f:

$$f = V_{up}^{seismic}/(V_{up}^{aseismic} + V_{up}^{seismic}) \quad \text{(Eq. 2)}$$

where f is the proportion of seismically induced uplift relative to the total uplift caused by seismic and aseismic deformations over one seismic cycle. By definition, f is close to 1 in regions with high inter-seismic coupling (locked faults as in the Himalayas and illustrated in Figure 2b; Stevens and Avouac, 2015), and is much smaller in regions with low coupling (Figure 2c). We later use f to evaluate how aseismic slip contributes to the volume budget and balance over earthquake cycles (Section 7). We consider a scenario where tectonic loading is applied from far field at regional scales and is expected to have negligible influence on near-fault surface deformation during the inter-seismic period (Simpson, 2015). Thus, as noted above (Section 2), in regions where inter-seismic loading is significant (e.g., Taiwan and the frontal Himalayas), our model can only resolve the co-seismic and post-seismic components of deformation, and must incorporate the inter-seismic component to describe a complete seismic cycle.

3.2. Seismic landslide erosion

3.2.1. Landslide volume

To describe the total volume of landslides associated with an earthquake event, Marc et al. (2016b) adopt an empirical linear relation between landslide volume and ground motion at local scales, simulate seismic ground motion using the empirical relations reported by Boore and Atkinson (2008), and integrate across landscapes to obtain total landslide volume. This modeling framework has also been used to define the boundaries of landslide occurrence., i.e. the spatial extent of landsliding (Marc et al., 2017).

We predict the volume of earthquake-triggered landslides (V_{ls}) using the model of Marc et al. (2016b), accounting for seismotectonic and topographic conditions, and further consider the effect of different seismological landslide-triggering factors. Specifically, the landslide volume is calculated as:

$$V_{ls} = \pi\delta_V a_c R_0^2 A_{topo}\left(\frac{R_{ref} b\bar{S}}{R_0 a_c} - 1\right)^2 \left(\frac{L}{I_c}\right) \exp\left(\frac{S_{\mathrm{mod}}}{T_{SV}}\right), \quad (R_{ref} b\bar{S} > a_c R_0) \qquad \text{(Eq. 3)}$$

where V_{ls} is the volume of earthquake-triggered landslides, δ_V is the hillslope material sensitivity to landsliding under a given shaking, a_c is the landslide-triggering threshold acceleration (0.15 g), R_0 is the mean depth of rupture area as an approximation of the mean depth of seismic energy sources, A_{topo} is the proportion of landscape area with sufficient steepness to trigger landsliding, b is the averaged acceleration at a reference difference R_{ref} (taken as 1 km) away from the seismic energy source, $\bar{S}$ is a coefficient representing the landscape-averaged site effects on amplification (dimensionless), L is the rupture length of the seismogenic fault as determined from M_w-based scaling relations for dip-slip faults (Leonard, 2010), I_c is a constant representing the characteristic length of seismic energy source, S_{mod} is the modal slope angle for the studied landscape, and T_{sv} is the global-averaged steepness normalization constant (11.6±0.6°).

A complete derivation of Equation 3 is detailed in Marc et al. (2016b). Here we summarize their approach, emphasizing how they derive local seismic ground motion, a central parameter in the model. Marc et al. 2016b assume that at local scales, landslide volume per unit area (i.e., "landslide volume density") scales with an exceedance acceleration, the difference between local ground motion a and the landslide-triggering threshold acceleration a_c, following empirical observations (e.g., Meunier et al., 2007). They calculate the patterns of ground motion and landslides caused by one seismic energy point source (conceptualized as a spot with a characteristic length of I_c) at depth R_0 across the whole landscape, integrate over the total number of seismic energy point sources (L/I_c) and the range of the emission angles and radii of seismic waves, correct for the steepness of landscpaes (A_{topo} and

S_{mod}), and obtain a landslide volume function with scaling parameters T_{sv} and δ_V. They then estimate the scaling parameters (T_{sv} and δ_V) by calibrating the model to a global database of the volumes of co-seismic landslides. Estimating local ground motion is a key part of their analysis. They obtain local seismic peak ground acceleration a at one landscape cell caused by a seismic energy point source, assuming attenuation is mainly caused by geometric spreading of seismic waves and neglecting any non-linear attenuation, as:

$$a = b(\overline{S} + dS)R_{ref} / d \qquad \text{(Eq. 4)}$$

Where b is the source acceleration at a reference distance R_{ref} (taken as 1km here), $\overline{S}$ is the average site response over the whole landscape that accounts for how surface topography modulates seismic acceleration, dS is the deviation of local site response from the landscape-averaged $\overline{S}$, and d is the distance of the landscape cell to the seismic energy source. Equation 4 thus represents a simplified form of ground motion prediction equations (GMPE), accounting for scaling with earthquake magnitude, site effects, and distance from the source (e.g. Boore and Atkins, 2008).

Equation 4 is difficult to solve directly because b, $\overline{S}$, and dS are not well constrained at regional scales. Empirical observations and modeling studies show that the local site response of source acceleration depends strongly on hillslope morphology and that ($\overline{S}$ +dS) can vary significantly, for example by a factor of 2-10 (e.g. Meunier et al., 2008; Maufroy et al., 2014). Marc et al. (2016b) propose that when integrating over the whole landscape, the total effect of dS should be negligible (i.e. treating dS as random noise), considering that landslides occur across multiple locations characterized by randomly varying dS. After eliminating the dS term, $b\overline{S}$ is then considered as a combined term. The term b is calculated using a group of M_w-dependent ground motion prediction equations developed by Boore and Atkinson (2008):

$$b\overline{S} = b_{sat}\overline{S}\exp[e_5(M_w - M_h) + e_6(M_w - M_h)^2], \quad (M_w \le M_h) \qquad \text{(Eq. 5)}$$

$$b\overline{S} = b_{sat}\overline{S}\exp[e_7(M_w - M_h)], \quad (M_w > M_h) \qquad \text{(Eq. 6)}$$

where M_h is a “hinge” magnitude beyond which ground motion saturates at b_{sat}, and e_5, e_6 and e_7 are empirical parameters. These parameters are constants for the 5%-damped pseudo-acceleration (PSA) for seismic waves with specified periods or for other ground motion indexes like peak ground accelerations (PGA) and peak ground velocities (PGV), and are empirically determined from 58 worldwide earthquakes (Boore and Atkinson, 2008).

Although b_{sat} and $\bar{S}$ are difficutl to determine independently, Marc et al. 2016b use empirical observations to constrain the combined term $b_{sat}\bar{S}$. Neglecting dS, $b_{sat}\bar{S}R_{ref}/d$ should predict the saturated surface ground motion at distance d. Following this relation, Marc et al. (2016b) suggest that a representative value of $b_{sat}\bar{S}$ is $4g$, because this value means surface peak ground accelerations (PGA) around 0.4-0.8 g for large earthquakes with a source depth of 5-10 km, consistent with field observations from the 1999 Chi-Chi and 2008 Wenchuan earthquakes (Lee et al., 2001; Li et al., 2008). We retain this value suggested by Marc et al. (2016b).

In our model, we introduce two modifications of the landslide model by Marc et al. (2016b), to allow examination of landslide-triggering mechanisms and to reduce free parameters. First, we consider a range of seismological factors that can potentially trigger landslides. Marc et al. (2016a, 2016b) assume earthquake triggering of landslides is most directly related to 1 Hz (period = 1s) seismic S waves. However, the property of seismic energy release that causes landslides and thus optimally describes the total volume is not well known. In addition to 1 Hz waves, seismic waves of other frequencies, PGA, and peak ground velocities (PGV) have all been proposed as best explaining landsliding associated with earthquakes (Jibson and Keefer, 1993; Harp and Jibson, 1996; Dreyfus et al., 2013; Athanasopoulos-Zekkos et al., 2016; Tanyas et al., 2017). Given this uncertainty, we use the framework of Marc et al. (2016b) to model the volumes of earthquake-triggered landslides assuming different seismic factors that control landsliding triggering. We calculate the ground motion associated with each factor referring to the empirical relations and parameters reported by Boore and Atkinson (2008). For S waves, we focus on the oscillator period range of 0.1-10 s, or frequency bands of 0.1-10 Hz, as >10 Hz waves have high quality decay and <0.1 Hz waves likely have too long wavelength to cause damage at hillslope scales (Marc et al., 2016b). In each case, V_{ls} is calculated as a function of δ_{sn}, S_{mod}, R_0, and the seismological landslide-triggering factor that directly determined M_h, e_5, e_6 and e_7.

Secondly, we combine δ_V and A_{topo} as δ_{sn}, the normalized landscape failure susceptibility, to reflect the overall characteristics of a landscape:

$$\delta_{sn} = \frac{\delta_V A_{topo}}{\bar{\delta}_V} \quad \text{(Eq. 7)}$$

where $\bar{\delta}_V$ is the global average hillslope material sensitivity (4174 m^3 km^{-2}, empirically determined from a global landslide inventory; Marc et al., 2016b). δ_{sn} thus integrates the effects of the properties of hillslope material and the overall steepness of the studied landscape, normalized by a global average condition.

3.2.2. Landslide spatial pattern

For the landslide spatial distribution pattern, we adopt an empirical relation (Meunier et al., 2007; Marc et al., 2017) and assume a linear seismic energy source:

$$P_{Vls} = P_0 \frac{R_0}{d} \exp(-\frac{d-R_0}{R_0\beta}) \quad \text{(Eq. 8)}$$

where P_{Vls} is the landslide volumetric density (volume of landslides in unit area, m^3 km^{-2}), d is the distance to the energy source, and P_0 and β are scaling factors. β is defined here as the spatial decay factor, with higher values meaning more widely spread landsliding. Note that Equation 7 is analogous to the law of seismic wave attenuation accounting for both geometric spreading and quality decay, and has successfully reproduced the patterns of landslides caused by the Chi-Chi, Northridge, Finisterre, and Wenchuan earthquakes (Meunier et al., 2007; Li et al., 2018a). Based on current studies, $1/\beta$ ranges from around 0 (Chi-Chi) to 5 (Northridge). We assume landslide erosion results in complete removal of material within an earthquake cycle (Parker et al., 2011) and for simplicity do not consider the effects of sedimentation in adjacent basins, which will influence spatial patterns and could be added in future work.

3.3. Isostatic uplift

Using a flexural-isostasy model, we model the isostatic responses as the flexure due to erosional unloading (King et al., 1988; Watts, 2001). Landslide-induced erosion is converted to erosion depth across a 2-D cross section and approximated as a series of linear unloads, and the flexure caused by each segment of unloading is calculated numerically, after King et al. (1988). The rationale of using this 2-D approach is discussed in Section 2.1.

At local scales, the volume of erosion-induced isostatic uplift ($V_{up}^{isostasy}$) varies as a function of landslide volume, T_e, and the landslide spatial decay factor, β. We note that, in this context, $V_{up}^{isostasy}$ only refers to the isostatic response to erosion, following the convention of King et al. (1988). There is also isostatic response to seismic deformation over full earthquake cycles, but this component is considered in the calculation of post-seismic deformation, thus in the term $V_{up}^{seismic}$ (Section 3.1; Savage and Gu, 1985 and references therein).

As noted above, fluvial evacuation of landslide debris out of mountains (erosional unloading) and the isostatic response do not occur instantaneously, but operate over inter-seismic periods (Hovius et al., 2011; Wang et al., 2015). Thus $V_{up}^{isostasy}$ is calculated at the end of multiple seismic cycles when landslide evacuation and isostatic adjustment are complete, the same stage when post-seismic deformation is (almost) complete and accounted for in our calculation (Sections 2.2 and 3.1).

3.4. Selection of spatial window

Previous studies show that seismically induced deformations and erosion vary spatially (King et al., 1988; Keefer, 1994; Hovius et al., 2011; Parker et al., 2011; Li et al., 2014; Marc et al., 2016b); thus, the total balance between uplifted and eroded volume depends on the spatial window over which the volumes are budgeted. To account for this effect, we explore a wide range of values for the width of this window, and focus on two representative cases in our discussion: (1) a "near field window" on the hanging wall where most co-seismic uplift and earthquake-triggered landslide erosion occur, with the width of this window (W_n) determined by the distance beyond which ground motion is not strong enough to trigger landslides in the model, with reference to seismic energy source depth R_0 = 0 and assuming 1 s period (1 Hz) seismic waves as the main landslide-triggering factor (W_n increases with M_w, varying from ~5-50 km for M_w 5-9; Marc et al., 2017); and (2) a "far field window" centered at the fault rupture with a width (W_f) of four times of W_n, i.e., ~20-200 km across M_w 5-9, which covers near field deformations (both foot wall subsidence and hanging wall uplift) and a major part of far field deformation. For reference, the widths of modern-day tectonically active mountain belts (e.g., Taiwan) are generally around 50-200 km (Hovius, 1996; Watts, 2001).

3.5. Topographic volume balance over earthquake cycles

We first consider the seismic volume budget and balance without accounting for the aseismic component. We then introduce aseismic deformation and evaluate how this term affects the seismic volume balance. For seismic volume balance, within a specified spatial window, the erosion term is defined as the volume of earthquake-triggered landslides (V_{ls}), whereas the uplift term (V_{up}) is determined as the sum of seismic uplift volume ($V_{up}^{seismic}$, resulting from co-seismic deformation and post-seismic relaxation) and erosion-induced isostatic uplift volume ($V_{up}^{isostasyy}$):

$$V_{up} = V_{up}^{seismic} + V_{up}^{isostasy} \qquad \text{(Eq. 9)}$$

The seismic volume balance is expressed as the ratio (Ω) between the volume of landslides (V_{ls}) versus the uplifted volume (V_{up}):

$$\Omega = V_{ls}/(V_{up}^{seismic} + V_{up}^{isostasy}) \qquad \text{(Eq. 10)}$$

V_{ls} and $V_{up}^{isostasy}$ are calculated following the approaches in sections 3.2 and 3.3, and we define their ratio as $\lambda=V_{up}^{isostasy}/V_{ls}$. At regional scales, this ratio is determined by the relative magnitude of the density of the underlying lithosphere versus the asthenosphere (Molnar, 2012). At local scales with given density of the lithosphere and the asthenosphere, this ratio is a function of those parameters determining the extent to which isostasy compensates landslide erosional unloading, specifically lithospheric T_e and landslide spatial pattern factor β. As noted above, interpretation of our model results using λ is valid only in the context of our modeling framework considering the net effect of multiple earthquake cycles and where 2-D models are suitable (Section 2.1); explicit 3-D models would be required to simulate single earthquake events whose rupture length are shorter or of similar length scale as T_e. With λ, we rewrite the seismic volume balance ratio (Eq. 10) as:

$$\Omega = V_{ls}/(V_{up}^{seismic} + \lambda V_{ls}) \qquad \text{(Eq. 11)}$$

We next add the aseismic uplift volume ($V_{up}^{aseismic}$) to the uplift term in Equation 8 and define the volume balance over one full earthquake cycle as:

$$\Omega^* = V_{ls}/(V_{up}^{seismic} + V_{up}^{aseismic} + \lambda V_{ls}) \qquad \text{(Eq. 12)}$$

Combining Equations 2, 11, and 12, we have:

$$\frac{\Omega^*}{\Omega} = \frac{f}{1+(f-1)\lambda\Omega} \qquad \text{(Eq. 13)}$$

Ω^*/Ω provides a metric of how the volume balance ratio accounting for aseismic uplift differs from the seismic volume balance ratio. Based on Equation 13, we later explore how Ω^*/Ω varies across f, λ and Ω.

3.6. Sensitivity test

To evaluate the relative importance of different model parameters in determining the seismic volume budget, we perform a sensitivity test considering how changes in free parameters affect Ω, landslide volume V_{ls}, seismically uplifted volume $V_{up}^{seismic}$, and the ratio between the volumes of isostatic uplift versus landslides ($\lambda = V_{up}^{isostasy}/V_{ls}$). The input parameters are T_e, fault dip θ, normalized landslide failure susceptibility δ_{sn}, mean rupture depth R_0, landscape gradient, and landslide spatial decay factor β. We choose the ranges of the input parameters as observed in real geological settings (R_0: 2-40 km, T_e: 2-40 km, $\mathrm{Log}_{10}\delta_{sn}$: -1~1, θ: 10-70°, S_{mod}:20-40°, $1/\beta$: 0-5; Watts, 2001; Meunier et al., 2007; Marc et al., 2016b; Li et al., 2017). For a series of earthquake magnitudes from $M_w = 6$ to $M_w = 9$ and different seismological landslide-triggering factors that give different groups of M_h, e_5, e_6, and e_7, we fix all parameters at their medians, vary one parameter by 10% of the full sampling range at a time, and calculate the corresponding percentage deviation of V_{ls}, $V_{up}^{seismic}$, Ω, and $V_{up}^{isostasy}/V_{ls}$. The sensitivity tests are run for both the near field and the far field scenarios.

To visualize the model results in the multi-dimensional parameter space, we also present 2-D contour plots calculated using the same range for input parameters as the sensitivity analysis. We first fix all input parameters at their medians and then vary two parameters over the full range, calculating the difference between the resulting Ω and the average of all Ω values ($\overline{\Omega}$) as we focus on the relative difference rather than absolute values in this context, and report Ω-$\overline{\Omega}$ in 2-D contour plots. To test the sensitivity of V_{ls} and Ω to earthquake depth, we assume $V_{up}^{seismic}$ is constant over varying depth. This assumption may introduce a minor uncertainty (5-10%) to

$V_{up}^{seismic}$; Marc et al. (2016a) show that co-seismic uplift varies by 5-10% at different R_0 and King et al. (1988) suggest that T_e exerts the major control on post-seismic deformation (i.e, R_0 plays a minor role). Note that only in this analysis focusing on the relative changes do we make this assumption and vary earthquake depth to calculate $V_{up}^{seismic}$, whereas in other analysis concerning $V_{up}^{seismic}$, we always refer to Section 2.1.1 to use fault width and dip angle to estimate depth.

3.7. Wenchuan earthquake volume balance considering post-seismic effects

In addition to the general consideration of volume budgets for different earthquakes, we apply our approach specifically to the Wenchuan earthquake, where we can combine the model results with empirical observations. The comprehensive studies of earthquake-triggered landslides (e.g., Li et al., 2014; Xu et al., 2014) and seismically induced deformations (e.g., de Michele et al., 2010; Fielding et al., 2013; Huang et al., 2014) following the Wenchuan earthquake make this event an ideal case to study earthquake volume balance. Prior studies (Parker et al., 2011; Li et al., 2014) only considered the volume balance between co-seismic uplift and landslide erosion, not taking into account the effects of post-seismic relaxation and isostatic responses to erosion. Limited studies (e.g., Huang et al., 2014) have characterized post-Wenchuan deformation using <2 years of geodetic measurements but cannot constrain post-seismic deformation over the full earthquake cycle. Note that the seismogenic fault was thought to be fully locked before the Wenchuan earthquake (e.g. Wang et al., 2009); thus we neglect aseismic slip in this case.

We calculate the volume balance for the Wenchuan event over a full earthquake cycle, combining empirical data on the co-seismic uplift and landslide volumes with modeling of the post-seismic relaxation and isostatic response. We adopt the landslide map from Li et al. (2014) where landslide volumes were determined using an empirical area-volume scaling relation and co-seismic displacement data determined from SAR measurements by Fielding et al. (2013). We also model the co-seismic deformation field and earthquake-triggered landslides using the Wenchuan parameters, and validate our model results by comparing to field observations. With the co-seismic uplift data, we then model the completely relaxed deformation using the approach in Section 2.2. We model the flexural-isostatic response to landslide erosional unloading using the approach in Section 3.4, assuming complete removal of landslide debris between earthquake cycles. For the effective elastic thickness T_e, we consider values of 10, 20, 30 and 40 km, recognizing that estimates of T_e in the Wenchuan region vary broadly from ~7 to 40 km (Densmore et al., 2012 and references therein).

To better understand how earthquakes drive topographic development of the eastern Tibetan mountains where the Wenchuan earthquake occurred, we then consider the volume balance over multiple earthquake cycles for the Wenchuan region. We calculate the volume balance ratio for each earthquake magnitude using the parameters constrained from the Wenchuan data and estimate the probability distribution of Ω over multiple earthquake cycles to evaluate the net topographic effect of seismicity in this region.

4. Results

4.1. Patterns of seismically induced deformations

Over one full earthquake cycle, different processes contribute to producing distinct topographic structures. Co-seismic deformation creates focused uplift in a narrow zone above the fault plane, with far field subsidence on the hanging wall, and a combination of near field subsidence and far field bulging on the footwall (Figure 4a). Post-seismic relaxation distributes the localized, co-seismic deformation to far field areas, reducing the near field uplift and enhancing the hanging wall's far field uplift and the footwall's subsidence (Figure 4a, b and c). These deformation patterns depend in part on dip angle of the seismogenic fault (Figure 4a, b and c). Notably, the modeled seismic deformation produces similar topographic features as simple back-slip models (e.g., Savage et al., 1983), a propagator matrix-based analytical model (Thatcher and Rundle, 1984; King et al., 1988) and a viscoelastic finite element model (Simpson, 2015). Earthquake-triggered landslide erosion mainly focuses in a narrow zone and rapidly decays in the far field (Figure 4d). Flexural-isostatic compensation to erosional unloading is more widely distributed as compared to landsliding, featuring a bulge in the near field and depressions in the far field (Figure 4d, e).

4.2. Variations of the seismically induced volumes over input parameters

As shown in Equation 10, the earthquake volume balance ratio Ω is determined by the landslide volume V_{ls}, the seismic uplift volume $V_{up}^{seismic}$ as induced by co-seismic and post-seismic deformation, and λ, the ratio between the isostatically uplifted volume $V_{up}^{isostasy}$ and V_{ls}. Here we explore the variations of V_{ls}, $V_{up}^{seismic}$ and λ across the studied ranges of the input parameters as reported in Section 3.6, with earthquake magnitude varying from $M_w = 6$ to $M_w = 9$.

$V_{up}^{seisimc}$ varies as a function of earthquake magnitude M_w, lithospheric T_e and fault dip θ. Across the range of these parameters, $V_{up}^{seismic}$ has the most significant variation over M_w (~1000 times with M_w~6-9), relatively moderate variation over T_e (~10 times for T_e from 2-40 km), and limited change over θ (~1-3 times for θ from 30-60°), as illustrated by the color contours in Figure 5a and 5b. The effects of T_e and M_w are similar for near field and far field scenarios (Figure 5a, b). However, $V_{up}^{seismic}$ shows opposite trends over θ in the far field scenario (Figure 5b), which is caused by the fact that the far field window includes both local uplift and subsidence which increase together as θ grows, but the subsidence term increases faster, offsetting the uplift term and leading to a smaller $V_{up}^{seismic}$.

V_{ls} is similar in the near field window and the far field window (Section 3.5), so we just consider the total volume of V_{ls}. Mean rupture depth R_0 is a major control on V_{ls}, causing changes in V_{ls} (up to 10,000 times across the selected range of R_0) comparable or even exceeding changes over M_w (Figure 5c). The V_{ls}-M_w relations differ depending on the assumed landslide-triggering factor, with the maximum V_{ls} corresponding to 4 s period (0.25 Hz) S waves (Figure 5e). Notably, for a given earthquake magnitude, the variation of V_{ls} calculated assuming different landslide-triggering factors is comparable to the entire range of V_{ls} across the studied earthquake magnitudes, emphasizing the importance of landslide-triggering mechanisms in V_{ls} and the earthquake volume balance (Figure 5e). V_{ls} has a moderate dependence on landscape failure susceptibility and steepness, showing ~100 times and ~10 times variations across their studied ranges, respectively (Figure 5d, f).

For isostatic response, in the far field scenario, λ is a constant determined by the ratio of the density of lithosphere versus that of the asthenosphere (Molnar and England, 1990; Molnar, 2012). In the near field scenario where the spatial window is independent of T_e and the wavelength of erosion-induced isostacy, λ is in theory controlled by the lithospheric rigidity and the spatial pattern of landslides (Densmore et al., 2012). The near field λ has a strong dependence on T_e and a relatively weak dependence on the spatial pattern factor of landslides, β, and is insensitive to changes in M_w (Figure 5g, h). The decreasing trend of near field λ with T_e is expected because higher T_e means higher lithospheric rigidity and causes more distributed isostatic uplift over broader areas.

The sensitivity analysis complements the above calculations and allows us to evaluate the relative importance of different parameters in the earthquake volume balance (Figure 6). The signs of the calculated sensitivities also indicate whether increasing a parameter would increase (positive) or decrease (negative) the uplift and landslide volumes and the related volumetric ratios. We have considered a series of earthquake magnitudes, different landslide-triggering factors that are representative of the observed Ω-M_w patterns (discussed later in Section 5.1 and in Figure 9), and the effect of spatial windows. In the near field scenario, the volume balance ratio (Ω) is highly sensitive to the landslide volume-related parameters including R_0, δ_{sn}, S_{mod}, moderately sensitive to T_e and θ, and almost insensitive to landslide spatial pattern factor β (Figure 6). In most cases, Ω is most sensitive to mean rupture depth R_0. Exceptional cases appear where landslides are triggered by waves of 4s period (0.25 Hz frequency) and $M_w \geq 8$, where Ω and V_{ls} is most sensitive to failure susceptibility and less sensitive to R_0. $V_{up}^{seismic}$ shows low sensitivity to θ and T_e. The near field isostasy ratio λ responds weakly to changes in T_e, with no obvious responses to changes in other parameters. Considering the meaning of the signs, the sensitivity analysis predicts erosive earthquakes should occur in cases with shallower R_0, thinner T_e, higher failure susceptibility, lower dip, and steeper S_{mod}, and would not be influenced much by the spatial pattern of landslides. In far field scenarios, most findings are consistent with the near field cases, except that the isostasy ratio has almost no sensitivity to T_e and other parameters, as in this case λ is determined by the density difference between the lithosphere and asthenosphere. Also, in the far field case, higher fault dip would lead to lower $V_{up}^{seismic}$ and consequently higher Ω, opposite to the near field, as also shown in Figure 5b.

The contour plots also help to illustrate how Ω varies in the multi-dimensional parameter space, complementing the above sensitivity analysis (Figures 7 and A1-A4). In these plots, we report Ω-$\bar{\Omega}$, the changes of Ω relative to the average value of Ω in the sampling parameter space (see Section 3.6), and we show results for the far field scenario. The contour plots show that, in general, the earthquake volume balance ratio is sensitive to R_0, S_{mod} and δ_{sn} and relatively insensitive to θ and β. Sensitivity to T_e decreases as the absolute value of T_e increases. Similar to the sensitivity analysis, we also note that the 4s period represents an extremely erosive scenario (e.g., for $M_w \geq 7$, Ω~1 and $V_{ls}/V_{up}^{seismic}$ ~ 5, Figures 7, A2, A3 and A4) where earthquakes at deeper depth (>20 km) can still trigger landslides (e.g. Figure A4g) and Ω becomes insensitive to increases in V_{ls} (e.g. Figure A4h) because the uplift term is dominated by landslide erosion-induced isostacy such that Ω is close to the ratio of $V_{ls} : V_{up}^{isostacy}$, which is relatively stable in far field scenarios. However, Ω is still sensitive to changes in T_e, θ, and thus $V_{up}^{seismic}$, when V_{ls}-controlling parameters are fixed (e.g. Figure A4i). The near field scenario shows similar trends as the far field results, except for θ which has opposite effect (Figure 5b).

Overall, the above analysis demonstrates that in most cases, earthquake magnitude is the dominant control on the volume of both the uplifted topography and landslides, consistent with attention on this parameter in prior studies (Li et al., 2014; Marc et al., 2016a). For a given earthquake magnitude, seismological landslide-triggering factors, mean rupture depth and lithospheric effective elastic thickness can modulate the earthquake volume budget.

5. What is the role of earthquake magnitude?

5.1. Volume balance across earthquake magnitudes

In this section, we revisit the problem of earthquake volume balance over varying earthquake magnitudes, previously considered by Li et al. (2014) and Marc et al. (2016a). Here we consider how post-seismic processes influence this analysis, and how conclusions are sensitive to assumptions about the seismic properties responsible for triggering of landslides. As fault size and the generated earthquake magnitudes vary both spatially and temporally, the Ω-M_w pattern provides key information about the spatiotemporal variability in the erosivity of earthquakes.

Across the selected ranges of T_e and θ, $\mathrm{Log}_{10}(V_{up}^{seismic})$ scales mostly linearly with M_w (Figure 8a, b); the gentle curvature is an artifact caused by integrating volumes within defined spatial windows. The modeled V_{ls}-M_w relations feature a kink corresponding to the seismic hinge magnitude beyond which ground motion saturates (Figure 8c, d, e and f). Assumptions about landslide-triggering factors play a first-order role in determining the V_{ls}-M_w relations, determining not only where the "kink" (hinge magnitude) is, but also the curvature in the relationships and the absolute values of V_{ls}

(Figure 8c). For a given landslide-triggering factor, mean rupture R_0 does not influence the location of the kink and the V_{ls}-M_w curvature beyond the hinge magnitude, but impacts the absolute values of V_{ls} and the curvature when M_w is smaller than the hinge magnitude (Figure 8d). In contrast, landscape failure susceptibility and steepness only affect the absolute values of V_{ls} but not the patterns of the V_{ls}-M_w curves (Figure 8e and f). These differences ultimately control the balance between uplift and landslide erosion for a single event (Figure 8a-d).

Since the seismic triggering factor exerts a first order control on the V_{ls}-M_w relationship, we calculate volume balance (Ω, the ratio of V_{ls} to $V_{up}^{seismic}$) across earthquake magnitudes considering different assumed landslide-triggering factors (Figure 9a for near field and Figure 9b for far field scenarios). We report the results for fixed values of other input parameters (θ = 45°, T_e = 20 km, R_0 =10 km, S_{mod} = 30°, $1/\beta$ = 1, and δ_{sn} = 1) and note that changing these parameter values will change the absolute values of volume balance ratio, as detailed in the sensitivity analysis in Section 4.2 and Figure 6, but the overall trends in the Ω-M_w relationships should remain similar. In general, we find four types of Ω-M_w relationships: (1) "hump" curves featured by peak Ω around M_w5-6 (category A in Figure 9c and d, for waves with periods of 0.1-0.2 s and PGA), (2) hump curves with peak Ω around M_w6.7 (category B in Figure 9c and d, for waves with periods of 0.2-2 s), (3) hump curves with peak Ω around M_w8-9 (category D in Figure 9c and d, for S waves with periods of 5-10 s and PGV), and (4) curves which increase monotonically with M_w featured by kinks at M_w6.7 (category C in Figure 9c and d, for S waves with periods of 3-4 s). The Ω-M_w pattern of type (2) is similar to that reported in Marc et al. (2016a) where 1 Hz S waves are the major trigger of landslides, such that intermediate-magnitude earthquakes are most erosive and earthquakes of smaller or greater magnitudes are more constructive. The Ω-M_w pattern of type (4) is similar to that reported in Li et al. (2014), in which earthquakes of higher magnitudes tend to be more erosive. As noted above, changes of other parameters or the spatial window will change the absolute values of Ω but will not change the general patterns of the Ω-M_w relationships. We also note that seismological landslide-triggering factors have a major control of the patterns of Ω-M_w relationships, but have much less influence on the previous sensitivity analysis and contour-based illustration of Ω across the multiple-dimensional parameter space (e.g. Figures 6 and 7). Post-seismic processes, while important in determining the magnitude and spatial distribution of deformation, do little to affect the shape of the relationship between the volume balance and earthquake magnitude. Our results thus highlight the role of the seismological landslide-triggering factors in setting the relative erosivity of earthquakes as fault systems develop (e.g., Wesnousky et al., 1988; Wesnousky, 1994; Hillers et al., 2007; Ben-Zion, 2008; Milliner et al., 2016). Since much remains unknown about which seismic factors are most important in landslide triggering and how this sensitivity varies, we suggest that better defining the seismic factors responsible for triggering landslides is needed in future studies.

5.2. Efficiency of eroding and uplifting topography depends on earthquake magnitude

Earthquakes make use of seismic energy release to uplift topography, thus increasing gravitational potential. Earthquakes also use seismic energy to overcome cohesion and friction resistance, triggering landslides. In these respects, the processes by which earthquakes build and erode topography can be conceptualized as energy-conversion, and we can think of earthquakes as using seismic energy to drive landscape change (Wolman and Miller, 1960; Muenchow et al., 2012). For different earthquake magnitudes, the ratio between seismically eroded or uplifted volume versus seismic moment release (i.e., the amount of landscape change induced per unit energy) represents the efficiency of earthquakes in driving topographic change. With this concept in mind, we calculate the seismic moment M_o (N·m) from M_w using Equation 14 (Hanks and Kanamori, 1979):

$$\mathrm{Log}_{10} M_o = 1.5 M_w + 9.05 \quad \text{(Eq.14)}$$

and we consider $V_{up}^{seismic}$ and V_{ls} as a function of M_o, respectively (Figure 10).

Considering landslide erosion, the M_o-V_{ls} relations tend to have shallower slopes at higher M_o (Figure 10a). The M_o-normalized landslide volume shows rapid increases at lower magnitude, peaks near the corresponding hinge magnitude, and gradually decays towards higher magnitude (Figure 10b). This pattern is independent of the assumed landslide-triggering factor, and the decaying trends towards higher magnitudes are consistent with the saturation effect on ground motion (Boore and Atkins, 2008). The modeled V_{ls}/M_o-M_w relations suggest that for the same seismological and topographic conditions and within the range of earthquake magnitudes that trigger landslides (M_w>5 in this context), smaller-size events are more efficient in generating landsliding and eroding topography as compared to larger-size events. Notably, this finding updates the understanding of Keefer (1994) which showed that V_{ls} scales linearly with M_o, suggesting a uniform efficiency in eroding topography across earthquake magnitudes, with a more comprehensive consideration of the seismological factors triggering landslides.

For the uplifted volume, $V_{up}^{isostasy}$ scales linearly with V_{ls} under given T_e, and thus is expected to display the same behavior as V_{ls} (Figure 10a,b). Similar to V_{ls}, the $V_{up}^{seismic}$-M_o relations also have shallower slopes at higher M_o (Figure 10d), and the M_o-normalized seismically uplifted volume decreases towards higher magnitude (Figure 10e), suggesting lower efficiency of high magnitude events. This finding is actually expected when considering the scaling relations between fault dimensions, earthquake magnitude, and seismic moment. By definition, seismic moment is the product of shear modulus μ, fault displacement D, and fault rupture area A:

$$M_o = \mu \times A \times D \quad \text{(Eq. 15)}$$

and fault rupture area A is the product of fault rupture length L and fault with W assuming a rectangular rupture surface:

$$A = W \times L \tag{Eq.16}$$

Fault rupture length L, fault width W, and fault displacement D all scale with M_o (Leonard, 2011). As derived in Li et al. (2014), the co-seismically uplifted volume is proportional to product $A \times D$ or $W \times L \times D$, and thus scales linearly with seismic moment M_o, indicating a power-law exponent of one and uniform efficiency across earthquake magnitudes. Whereas fault width W dictates the horizontal wavelength of the co-seismically uplifted topography (Li et al., 2014), the effect of post-seismic relaxation depends heavily on T_e that is independent of M_o. Thus, over a full earthquake cycle, the dependence of $V_{up}^{seismic}$ on W and M_o is reduced, leading to a power law exponent smaller than one, i.e., a decreasing trend in the $V_{up}^{seismic}/M_o$-M_o relation. Due to the limitations of our 2-D calculation, we cannot directly evaluate the dependence on fault length, which likely has more profound influence for single earthquakes with shorter rupture length and requires further examination in 3-D models.

Thus, when considering how seismic energy release drives topographic change, larger earthquakes are less efficient both in terms of landslide erosion and uplift, compared to their smaller relatives. This suggests that as fault systems mature and are capable to accommodate higher M_w events, it is possible that the efficiency of both inducing landslide erosion and producing topography may decrease. At the same time, growing fault zones can promote structure complexities and local deformation features that could limit high magnitude events (e.g., Wesnousky, 1994), potentially complicating how they release seismic energy and cause topographic change.

Normalizing volumes by seismic moment helps in evaluating the efficiency of earthquakes of different magnitudes, both in terms of landslide erosion and seismically induced uplift. However, over multiple earthquake cycles, earthquake recurrence time depends on earthquake magnitude. We take into account the M_w-earthquake recurrence time relation, in order to evaluate how earthquakes of different magnitudes contribute to the cumulative topographic changes over longer time scales of multiple earthquakes, accounting for the M_w-earthquake recurrence time relation. Taking the same approach as in Section 2.1, we model earthquake sequences over multiple seismic cycles using a Gutenberg-Richter M_w-frequency distribution. We consider a common fault setting where θ= 45°, T_e= 20 km, S_{mod}= 30°,δ_{sn}= 1, and $1/\beta$ = 1, and allow earthquake depth and magnitude to vary. We then calculate the total seismically eroded landslide volume within each earthquake magnitude bin (ΔM_w = 0.1), as the product of the recurrence time of the earthquakes in the magnitude bin and the corresponding V_{ls}, respectively. We perform this calculation for a broad range of R_0 (1-40 km) and integrate V_{ls} over R_0 for each earthquake magnitude bin. We then quantify the contribution from each earthquake magnitude bin to the total volume budget over multiple earthquake cycles. Similarly, we calculate the contribution to the total seismic uplift from earthquakes of varying magnitudes, but we set earthquake depth equivalent to the product of fault width and sin(θ), although we expect varying depth would cause limited influence to $V_{up}^{seismic}$ (e.g. Marc et al., 2016a; Section 3.6).

As shown in Figure 10c, medium-to-high magnitude earthquakes are the most significant contributors to landslide erosion, and the magnitudes of maxima volumetric contribution correspond to the hinge magnitude beyond which ground motion saturates (Figure 9). This finding further emphasizes the importance of landslide-triggering mechanisms in understanding the volume budget caused by earthquakes. As shown in Figure 10f, high magnitude earthquakes, though occurring less frequently, contribute most to the total uplifted volume than the more frequently occurred, small-medium magnitude earthquakes.

6. Post-seismic processes and wavelengths of deformations

6.1. Effect of post-seismic processes in seismic mountain building

Post-seismic processes represent the rheological response of the lithosphere-asthenosphere system to surface changes induced co-seismically and over the earthquake cycle, but the effect of post-seismic processes has not been considered in previous models of earthquake volume balance (Li et al., 2014; Marc et al., 2016a). For a given landslide volume model and landslide-triggering factor, post-seismic processes do not fundamentally change the relative volume balance across M_w, i.e., the pattern in Figures 6 and 7, as compared to prior co-seismic studies (Li et al., 2014; Marc et al., 2016a). However, post-seismic processes could cause large variations in the absolute values of uplift volumes, and thus affect whether earthquakes are net constructive or erosive. Specifically, post-seismic relaxation enhances hanging wall uplift and footwall subsidence, and isostasy causes distributed uplift (Figure 4). The net topographic effects of these processes and their volume budget vary in different seismotectonic and landscape settings, as evidenced by changes of $V_{up}^{seismic}$ and λ versus the studied seismotectonic and landscape parameters (Figure 5). Isostasy offsets a major part of landsliding (Molnar, 2012) but does not entirely compensate for the erosional losses, such that some earthquakes that trigger landslides of large enough volumes (e.g., 10 times of $V_{up}^{seismic}$) can still be net erosive over the timescale of earthquake cycles, although such highly erosive events have been rarely observed (e.g., considering landslide volume compilation in Marc et al., 2016b).

Notably, across the assumed landslide-triggering mechanisms and the selected range of the model parameters, far field Ω is systematically higher than near field Ω (Figure 9). Since V_{ls} remains similar in both near field and far field cases, this difference is caused by the fact that far field V_{up} is smaller than near field V_{up} with the studied range of the parameters. The difference in V_{up} for near versus far field emerges because V_{up} is composed of the seismically uplifted volume $V_{up}^{seismic}$ and the isostatically uplifted volume $V_{up}^{isostasy}$, and $V_{up}^{seismic}$ is the sum of local uplift and subsidence. When expanding the spatial window, there is a trade-off between isostatic uplift versus seismically induced subsidence. In the near field scenario, for given T_e and landslide pattern, $V_{up}^{isostasy}$ is minimal because the majority of the isostatic uplift is distributed in the far field, but $V_{up}^{seismic}$ is maximal as most subsidence lies outside this window. Vice versa, in the far field window, $V_{up}^{isostasy}$ and seismically induced subsidence both increase, but seismic subsidence outpaces isostatic uplift, leading to the reduction of the total V_{up}, and consequently a higher value of Ω, as shown in Figure 6. Such effects are mainly observed in cases where V_{ls} is smaller or comparable to $V_{up}^{seismic}$. In extremely erosive events where earthquakes trigger large enough volumes of landslides (e.g, 10-100 times of $V_{up}^{seismic}$), it is possible that $V_{up}^{isostasy}$ outweighs seismically induced subsidence, leading to a higher V_{up} in the far field window. However, we expect that such events rarely if ever occur in nature, such that the importance of isostasy is secondary to the counteraction of uplift by subsidence (e.g., Barlow et al., 2015).

Overall, we conclude that post-seismic effects exert a secondary influence on the relative patterns of M_w-earthquake volume balance relation, but can meaningfully affect the spatial patterns.

6.2. Wavelength of seismically produced topography and tectonic implications

The spatial patterns of seismic and post-seismic deformations may contribute some insight into the construction of the tectonic features observed today. Earthquake-triggered landslides are concentrated in the near field but the corresponding isostatic responses broaden the region of deformation relative to co-seismic effects alone (Figure 4). Post-seismic relaxation also distributes co-seismic uplift and subsidence to the far field. Thus, we expect erosion to be focused near range-bounding faults (Li et al., 2017), while uplift and subsidence extend over wide areas. This pattern of concentrated erosion and distributed uplift and subsidence is consistent with the structure of a range-basin system where erosion is focused along mountain fronts and uplift and subsidence are distributed broadly, demonstrating that earthquakes can produce such tectonic features (e.g., King et al., 1988). Another interesting observation is that the wavelength of seismically created topography scales with M_w and T_e (Figure 11). This finding suggests that in landscapes controlled by seismogenic fault systems encompassing faults and earthquakes of varying sizes, the fault-produced topography should be composed of a series of topographic features with varying wavelength that is linked to fault characteristics. Aging, mature faults that are capable of generating fewer, higher magnitude, and deeper earthquakes are expected to produce longer wavelength, smoothed topography, whereas younger, less mature faults (e.g., Wesnousky, 1994; Ben-Zion, 2008) are likely to produce shorter wavelength, higher-relief, steeper topography at a faster pace.

7. Aseismic processes and the influence on the volume balance over earthquake cycles

Equation 13 and the deformation partitioning coefficient f help us to evaluate the role of aseismic uplift in the volume balance over earthquake cycles. Based on Equation 13, we calculate Ω^*/Ω as a function of f for varying isostatic compensation (λ) and seismic volume balance ratio (Ω). As shown in Figure 12, Ω^*/Ω (volume balance ratio accounting for both seismic and aseismic uplift : seismic volume balance ratio) generally increases as f increases. As f approaches 1, Ω^*/Ω becomes less sensitive to change in f. For a given f, Ω^*/Ω gets further away from 1 both as λ and Ω decreases (Figure 12a and b), suggesting that aseismic slip can affect the overall volume balance significantly in cases when isostatic compensation is weak (low λ) and/or landslide erosion counteracts little uplift (low Ω). Alternatively, for a given long-term tectonic uplift rate over earthquake cycles, higher f indicates more contribution to topography from seismic processes that trigger landslides, thus meaning relatively more landslide erosion as compared to low f scenarios.

Although there is no direct measurement of f in real geological settings, we use seismic coupling coefficient, χ, defined as the ratio of seismic slip versus long-term slip, as a first-order approximation of f. Previous studies have compiled seismic coupling coefficients in typical tectonic settings and in major convergent plate boundary systems (e.g., Bird and Kagan, 2004; Wang et al., 2009; Theunissen et al., 2010; Ader et al., 2012; Scholz and Campos, 2012; Stirling et al., 2012; Stevens and Avouac, 2015; Li et al., 2018b), and we report those values in Figure 12c and 12d. In regions of high inter-seismic coupling (e.g., the Himalayas and the eastern Tibetan mountains), i.e., where we assert that f is close to 1, the corresponding Ω^*/Ω is predicted to be close to 1 as well (Figure 12a and b), meaning limited influence from aseismic slip on the total volume balance over earthquake cycles. If inter-seismic coupling is low and aseismic uplift is significant, the seismic volume balance ratio Ω can be corrected to Ω^* using Equation 13 with the related parameters constrained. We also note that in typical continental convergent boundaries where mountainous topography is pronounced (e.g., the Himalayas), χ and f are in general higher and closer to 1 than in other settings (Figure 12c and 12d), pointing to a major role of earthquakes in building topography in these environments. Yet we also recognize, as noted above, that many of these settings may be characterized by inter-seismic deformation associated with tectonic loading, which our model does not consider. Overall, although our analysis focuses on the volume budget and balance caused by seismic processes, f and χ allow us to also account for aseismic uplift and thus provide a more comprehensive picture of deformation across earthquake cycles in diverse settings.

8. Topographic effects of earthquake cycles at the eastern margin of the Tibetan Plateau

We apply our model to the central Longmen Shan mountains where the 2008 M_w7.9 Wenchuan earthquake occurred, to evaluate how earthquakes drive topographic evolution at the eastern margin of the Tibetan Plateau. We neglect aseismic processes in this analysis, because the seismogenic fault is thought to have been fully locked before the Wenchuan earthquake (Wang et al., 2009), and we consider this to be a region where the assumption of minimal effects from inter-seismic tectonic loading may be justified (see above). We first delineate the deformation field associated with the Wenchuan event, combining observational data of co-seismic deformation and landslide erosion, along with modeling of inter-seismic deformation. For seismic deformation, we focus on the vertical displacement caused by the thrust component and neglect the strike-slip component which causes little vertical changes, although the Wenchuan earthquake contains both components (Liu-Zeng et al., 2009; Xu et al., 2009).

The observations from the Wenchuan earthquake illustrate well the distinct spatial patterns of seismically induced deformations (Figure 13), as predicted by our model: landslide erosion and co-seismic deformation (both from empirical observations for this event) focus in a narrow corridor (<50 km) above the fault plane and decay quickly away from the fault trace. Specifically comparing the empirical and model results, the magnitude and pattern of earthquake-triggered landslides match well with the results predicted from our model (Figure 13b). For co-seismic deformation, our model reproduces the structure on the hanging wall, but lacks accuracy on the footwall (Figure 13b). Whereas geodetic observations show limited subsidence in this case (de Michele et al., 2010; Fielding et al., 2013), our adopted co-seismic deformation model (Cohen, 1996) and other similar models based on uniform viscoelastic half space (Thatcher and Rundle, 1984; King et al., 1988; Okada, 1992; Marc et al., 2016a) predict major subsidence in the near field of the footwall. Such discrepancy is likely caused by the fact that in the case of the Wenchuan earthquake there is a strong contrast in lithospheric rheology between the hanging wall block (the Tibetan Plateau) and the footwall block (the Sichuan Basin, an ancient, intact carton whose viscosity is over two orders of magnitudes higher than the adjacent Tibetan block; Huang et al., 2014 and references therein), which contradicts the assumption of homogeneous visco-elastic half space of the model. Moreover, numerical studies suggest that simple flexural-based models are not sufficient to explain footwall foreland basin subsidence, since more complex fault slip-basin margin interaction processes play an important role (e.g., Simpson, 2014). Such effects are also not considered in our model. However, as our model reproduces well the features on the hanging wall, we propose that our model is effective for the hanging wall side where landslide erosion and topographic uplift are mainly located, and we focus on the hanging wall results in the following discussion.

We lack empirical data to compare to the modeled post-seismic deformation and isostastic response, but the calculated values suggest that these distribute over much broader areas with much slower spatial decaying trends than the coseismic uplift or landslide erosion (Figure 13c).

To illustrate how the resulting Wenchuan earthquake volume balance varies spatially, we plot the volume balance ratio as a function of area in which the budget is calculated, which we define based on the distance to the fault trace and consider only the hanging wall results as discussed above (Figure 13d). Notably, the modeled co-seismic volume ratio curve shows a similar trend as that derived from empirical observations, with around 10% difference in magnitude (Figure 13d). The co-seismic volume ratio curve quick saturates within a narrow zone near fault (<30 km) and changes little beyond this zone, as suggested by Marc et al. (2016a). The post-seismic curves decay continuously, extending to far field (Figure 13d). Overall, the significant variation of the earthquake volume balance ratio over different integration boundaries (Figure 13d) demonstrates the importance of considering both far field and near field windows when interpreting the model results over earthquake cycles, whereas a near field window is likely sufficient for capturing co-seismic deformation. The Wenchuan example shows that considering post-seismic in addition to co-seismic processes can considerably change the inferred volume balance, with a greater difference in the far field and relatively smaller difference in the near field – emphasizing the role of post-seismic processes in affecting the spatial distribution of deformation.

We next consider the topographic effects of multiple earthquake cycles in the eastern Tibetan mountains. Whereas the field observations from the Wenchuan event help determine the parameters describing landscape susceptibility to landsliding and fault geometry (Liu-Zeng et al., 2009; Xu et al., 2009; Marc et al., 2016b; Li et al., 2017; Li et al., 2018a), major uncertainties exist in the effective elastic thickness (T_e ~7-40 km; Jordon and Watts, 2005; Densmore et al., 2012; Fielding and McKenzie, 2012; Huang et al., 2014) and earthquake depth (R_0, typically within 20 km depth in this region; Xu et al., 2009). To account for these uncertainties, in our modeling, we conduct Monte Carlo random sampling of T_e and R_0 for each earthquake magnitude bin (M_w~5-8 and $\Delta M_w = 0.1$) and report the medians and the 16th and 84th percentiles of Ω over earthquake magnitude for 1000 simulations (Figure 14a). Here we only consider the near field scenario to account for the mountainous region on the hanging wall. To integrate the effects over multiple earthquake cycles, we generate earthquake sequences using the earthquake frequency-magnitude relation established from the regional seismic catalog and paleoseismic studies (Li et al., 2017 and references therein). Note that the earthquake frequency-magnitude relation varies as a function of the different estimates of the recurrence time (T) of Wenchuan-like events. We then calculate an average near-field volume balance ratio Ω for all earthquake events of varying magnitudes, weighted by the total seismic uplift volume of each magnitude bin, i.e. the product of earthquake occurrence time and the corresponding seismic uplift volume for a single event of the specified M_w.

As shown in Figure 14b, the uplift volume-weighed distribution of Ω varies slightly across different estimated recurrence interval of the Wenchuan-like events (T). Across the range of reported T values (500-4000 years), we find that the net topographic effect of earthquake cycles tends to be constructive, with >95% probability for $\Omega<1$ and <5% probability for $\Omega>1$. Using a similar approach, we also calculated the volume balance for co-seismic scenarios (Figure 14c and d, $\Omega_{\text{co-seismic}} = V_{ls}/V_{up}^{co\text{-}seismic}$).

Compared to the volume balance over full earthquake cycles, we find that in co-seismic scenarios, earthquakes tend to be more erosive (with 10-30% probability, Figure 14d), and this difference clearly demonstrates the buffering role of inter-seismic processes in regulating seismically produced topography. Overall, at the eastern margin of the Tibetan Plateau, our analysis suggests that earthquakes work mainly as topographic constructors over multiple seismic cycles, even though the Wenchuan earthquake stimulated interest in this problem due to its highly erosive characteristics (Figure 14b).

9. Conclusions, limitations and implications

Taking a modeling approach, we have evaluated the volume balance between tectonic uplift and landslide erosion over earthquake cycles, considering varying magnitudes and different seismotectonic and topographic conditions and extensively exploring the relevant parameter space. Several findings contribute to better understanding of the seismic role in mountain building:

(1) The extent to which earthquakes build or destroy mountains depends on earthquake magnitudes, topographic and seismotectonic conditions, and assumptions about the seismological triggering of landslides. At the eastern margin of the Tibetan Plateau where the 2008 Wenchuan earthquake occurred, across the currently known ranges of the related parameters and the possible mechanisms triggering landslides, we conclude that the long-term effect of earthquakes tend to be topographic constructive, and that destructive events are rare (e.g., Figure 14b). Nonetheless, though most are likely not to be net destructive, the erosive power of earthquakes may play a significant role in topographic evolution, particularly by affecting the location and spatial distribution of deformation.

(2) Different processes operating over one full earthquake cycle produce topographic forms of distinct spatial patterns. Landslide erosion and co-seismic deformation are focused on a narrow window near the fault trace, but post-seismic relaxation and erosion-induced isostatic uplift distribute deformation over broader areas. Thus understanding of the earthquake volume balance depends on defining a specified spatial window, and one-dimensional calculations may overlook the fact that spatially non-uniform deformation can shape the resulting topographic features. Aseismic slip can also contribute to long-term uplift, and can be accounted for in the overall volume balance using a deformation partitioning coefficient, though the influence of aseismic deformation is expected to be limited in regions with high inter-seismic coupling, such as the Himalayas and the eastern margin of the Tibetan Plateau.

(3) We confirm previous findings (Li et al., 2014; Marc et al., 2016a) that earthquake magnitude exerts a primary control on the volume of earthquake-triggered landslides and seismically uplifted topography, and thus on the related volume balance ratio. Seismotectonic and topographic conditions modulate volumes of seismically induced deformations but have a secondary influence on the overall budget, except in cases

where landscapes have very limited susceptibility of landsliding (e.g., low steepness). Larger landslide volumes and more erosive earthquake events tend to occur in seismic zones featured by shallower rupture depths and thinner effective elastic thickness, and in steeper and more landslide-prone landscapes.

(4) Assumptions about the seismological factor that is most relevant to landslide triggering lead to large uncertainties in modeled landslide volume and volume ratio, highlighting the importance of better understanding of landsliding-triggering mechanisms. The assumed landsliding-triggering factor also dictates the patterns of V_{ls}-M_w and Ω-M_w relations. As M_w increases, Ω either peaks around the hinge magnitude beyond which ground motion saturates or increases monotonically with M_w, depending on the assumed landslide-triggering factor.

(5) Seismically uplifted or eroded topography represents the geomorphic work done by earthquakes using the released seismic moment. At higher earthquake magnitudes, earthquakes gradually erode and uplift less volume per unit seismic moment, meaning they are less efficient in driving topographic change. This relationship is caused by the saturation of ground motion approaching higher magnitude and the lower dependence on fault width that determines the horizontal wavelength of the seismically uplifted topography. However, when considering the relative contributions to the total volume budget, we find that higher magnitude earthquakes contribute more to total seismic uplift, whereas medium-to-high magnitude earthquakes contribute most to landslide erosion.

(6) Over full earthquake cycles, the wavelength of seismically created topography to first-order scales with T_e, earthquake magnitude, and fault dimensions. These findings provide a mechanistic link between fault characteristics, seismicity and topography. We hypothesize that aging, mature fault systems that can generate higher magnitude earthquakes are capable to produce longer wavelength, smoothed topography, whereas less mature faults tend to create shorter wavelength, higher-relief, steeper topography.

Despite these new understanding gained from our modeling effort, several limitations exist in this work, and these limitations point to key directions of further research.

(1) As we neglect inter-seismic loading, our model does not fully represent the processes active in regions where inter-seismic processes contribute significantly to surface deformation (e.g. the Himalayas and Taiwan), although our model does capture the co-seismic and post-seismic components and is expected to work well in settings where inter-seismic loading is applied at regional scales (e.g. eastern Tibet). As we focus on seismic processes, we simplify aseismic processes using a deformation partitioning coefficient. However, aseismic processes can also play an important role in long-term uplift in some settings (Simpson, 2015; Marc et al., 2016a). More detailed modeling of aseismic processes considering different modes of

creeping and loading (e.g. regional vs. localized, Johnson et al., 2005; Simpson, 2015) could add further insight, as could modeling of tectonic leading coupled to episodic seismically-triggered erosion.

(2) With the shortcomings of our 2-D approach, our model captures single seismic cycles only for high magnitude earthquakes with long rupture length ($L/T_e > \sim 10$) and long recurrence time (e.g. >10 times of Maxwell relaxation time τ), or multiple earthquake cycles when the tectonic setting satisfies the above rules. Applying the model to single smaller magnitude events with lower fault length-to-T_e ratios could be problematic. The 2-D approach also limits our understanding of the 3-D structures of seismically induced deformation and how along-strike variations influence on the seismic volume budget. 3-D models are needed in future studies to address these issues (e.g., Sun et al., 2014; Ren et al., 2018).

(3) As our model is based on homogeneous viscoelastic half space, our model will not accurately represent regions with heterogeneous rheology such as the eastern Tibetan margin, where our results perform poorly in replicating the observed footwall deformation associated with the Wenchuan earthquake. Moreover, we have not considered the role of sedimentation and fault slip in range-bounding basins (e.g. King et al., 1988; Densmore et al., 2012; Simpson, 2014), which emerges in our Wenchuan modeling and should have major influence in other range-basin settings as well. In the context of our modeling framework, adding a sedimentation component in the footwall basins would both reduce footwall subsidence (because of sediment infill) and the adjacent hanging wall uplift due to flexural isostatic response to loading, but the net effect remains unconstrained. To better constrain the role of basin sedimentation in earthquake volume balance, future studies are needed to better describe how sediments are distributed in range-front basins, which likely vary as functions of fluvial sediment transport and the properties (e.g. geometry, structure, and rheology) of the range-frontal basins (Huang et al., 2014; references). Recent studies also highlight the importance of the kinematics of basin margins related to fault slip and lithospheric deformation in basin subsidence (Simpson, 2014), which should be considered as well. However, we do not expect including the sedimentation component would affect our major interpretations that earthquake sequences tend to be topographically constructive in settings like the eastern Tibetan mountains, and that landslide erosion can affect topographic wavelength.

(4) We do not consider the evolution of relief with time, as in a landscape evolution model, or the effect of geomorphic transport processes driven by climatic variations (Whipple, 2009; Perron, 2017). Neither do we account for the transient changes of landslide propensity in response to climatic triggers during post-earthquake time periods (e.g. Marc et al., 2015; Parker et al., 2015), which are also important mechanisms of how earthquakes work to influence landscape erosion. Thus we cannot simulate how fault systems, earthquake cycles, and mountainous landscapes co-evolve over time.

Overall, although our model has these many shortcomings and simplifications, our results have meaningful implications. One the one hand, we find that, especially when considering the modulating effect of post-seismic processes, the vast majority of large earthquakes in a setting such as the eastern margin of the Tibetan Plateau are likely constructive – dispelling any apparent paradox in which large earthquake might be thought of as “net erosive”. At the same time, our results suggest that the erosive component of earthquakes can be important in shaping first-order features of large-scale topography, especially considering the evolving characteristics of fault systems and how these characteristics may affect patterns of erosion versus uplift. Thus episodic, seismically-induced landslides erosion should be considered in more complete models of landscape evolution and crustal deformation over earthquake cycles, particularly considering the cumulative effect of multiple faults of varying maturity.

Symbol Notations

A	Fault rupture area, km^2
a	Local peak ground seismic acceleration, gravitational acceleration g
a_c	Threshold acceleration to landsliding, gravitational acceleration g
A_{topo}	Fraction of topography available for landsliding , dimensionless
b	Inferred acceleration at 1 km from seismic energy source for a given landslide-triggering mechanism, gravitational acceleration g
b_{sat}	Saturated acceleration of b, gravitational acceleration g
d	Distance to seismic energy source, km
D	Fault displacement, km
E	Young's modulus , Pa
f	Partitioning coefficient of deformation over earthquake cycles, dimensionless
e_5, e_6, e_7	Empirical scaling parameters for ground motion, dimensionless
I_{asp}	Seismic energy spot length scale, km
L	Fault rupture length, km
L_{sf}	Fault surface rupture length, km
M_o	Seismic moment, N·m
M_w	Moment magnitude, dimensionless
P_0	Scaling parameter for predicting landslide pattern, m^3 km^{-2}
P_{Vls}	Landslide volumetric density, m^3 km^{-2}
R_0	Mean asperity depth, km
R_{ref}	Reference distance, km
S	Site effect on amplification of ground motion, dimensionless
$\bar{S}$	Average site effect on amplification of ground motion, dimensionless
S_{mod}	Landscape modal slope, °
τ	Maxwell relaxation time, yr
T	Recurrence time of Wenchuan-like events, yr

T_e	Lithospheric effective elastic thickness, km
T_{sv}	Empirical steepness normalization constant, °
V_{ls}	Landslide volume, km^3
V_{up}	Total uplift volume, km^3
$V_{up}^{aseismic}$	Aseismically uplifted volume, km^3
$V_{up}^{isostasy}$	Isostatically uplifted volume induced by landslide erosion, km^3
$V_{up}^{seismic}$	Seismically uplifted volume, km^3
W	Fault width, km
W_f	Width of far field window , km
W_n	Width of near field window, km
β	Landslide spatial pattern factor, dimensionless
δ_{sn}	Normalized landscape failure susceptibility, dimensionless
δ_V	Landscape failure susceptibility, m^3 km^{-2}
$\bar{\delta}_V$	Global-averaged landscape failure susceptibility, m^3 km^{-2}
θ	Fault dip, °
λ	Ratio between $V_{up}^{isostasy}$ and V_{ls}, dimensionless
μ	Shear modulus, Pa
v	Poisson ratio, dimensionless
ρ_A	Density of asthenosphere, kg m^{-3}
ρ_L	Density of lithosphere, kg m^{-3}
Ω	Seismic volume balance ratio, dimensionless
Ω^*	Volume balance ratio over full earthquake cycles accounting for uplift driven by both seismic and aseismic processes, dimensionless
$\Omega_{\text{co-seismic}}$	Co-seismic volume balance ratio (landslide erosion : co-seismic uplift), dimensionless
$\bar{\Omega}$	Average volume balance ratio over the sampling parameter space

Acknowledgement

This work is funded by the U.S. National Science Foundation (NSF-EAR/GLD grants 1053504 and 1640894 to A.J.W.). G. L. was supported by a USC Dornsife college graduate merit fellowship. We thank Jean-Philippe Avouac, Sylvain Barbot, Alexander Densmore, Josh Roering, Niels Hovius, Odin Marc, Patrick Meunier, Yehuda Ben-Zion, James Dolan, Luca Dal Zilio, Lei Qin, Haoran Meng, Chris Milliner, Zhigang Peng, Mong-Han Huang and Joel Scheingross for helpful discussions. G. L. thanks Wanbin Chen for discussions about several mathematical problems involved in this work. We thank three reviewers and the Editor for their insightful and constructive comments that helped to improve an earlier version of the manuscript, and we appreciate the editorial handling. This paper is mainly built on the results from a numerical model, and the adopted Wenchuan seismic deformation and landslide data are contained in multiple published sources cited in references.

References

1. Athanasopoulos-Zekkos, A., H. Pence, and A. Lobbestael (2016), Ground Motion Selection for Seismic Slope Displacement Evaluation Analysis of Earthen Levees, *Earthquake Spectra*, *32*(1), 217-237.
2. Avouac, J. P. (2007), 6.09 - Dynamic Processes in Extensional and Compressional Settings – Mountain Building: From Earthquakes to Geological Deformation, in *Treatise on Geophysics*, edited by S. Editor-in-Chief: Gerald, pp. 377-439, Elsevier, Amsterdam.
3. Barlow, J., I. Barisin, N. Rosser, D. Petley, A. Densmore, and T. Wright (2015), Seismically-induced mass movements and volumetric fluxes resulting from the 2010 Mw7.2 earthquake in the Sierra Cucapah, Mexico, *Geomorphology*, *230*(0), 138-145.
4. Ben-Zion, Y. (2008), Collective behavior of earthquakes and faults: Continuum-discrete transitions, progressive evolutionary changes, and different dynamic regimes, *Reviews of Geophysics*, *46*(4).
5. Bird, P., and Y. Y. Kagan (2004), Plate-Tectonic Analysis of Shallow Seismicity: Apparent Boundary Width, Beta, Corner Magnitude, Coupled Lithosphere Thickness, and Coupling in Seven Tectonic Settings, *Bulletin of the Seismological Society of America*, *94*(6), 2380-2399.
6. Bollinger, L., S. N. Sapkota, P. Tapponnier, Y. Klinger, M. Rizza, J. Van der Woerd, D. R. Tiwari, R. Pandey, A. Bitri, and S. Bes de Berc (2014), Estimating the return times of great Himalayan earthquakes in eastern Nepal: Evidence from the Patu and Bardibas strands of the Main Frontal Thrust, *Journal of Geophysical Research: Solid Earth*, *119*(9), 7123-7163.
7. Boore, D. M., and G. M. Atkinson (2008), Ground-Motion Prediction Equations for the Average Horizontal Component of PGA, PGV, and 5%-Damped PSA at Spectral Periods between 0.01 s and 10.0 s, *Earthquake Spectra*, *24*(1), 99-138.
8. Boos, W. R., and Z. Kuang (2010), Dominant control of the South Asian monsoon by orographic insulation versus plateau heating, *Nature*, *463*(7278), 218-222.
9. Brenguier, F., M. Campillo, C. Hadziioannou, N. M. Shapiro, R. M. Nadeau, and E. Larose (2008), Postseismic Relaxation Along the San Andreas Fault at Parkfield from Continuous Seismological Observations, *Science*, *321*(5895), 1478-1481.
10. Burchfiel, B. C., L. H. R., R.D. van der Hilst, B.H. Hager, Z. Chen, R.W. King, C. Li, J. Lü, H. Yao, and E. Kirby (2008), A geological and geophysical context for the Wenchuan earthquake of 12 May 2008, Sichuan, People's Republic of China, *GSA Today*, 18(7), 5.
11. Cattin, R., and J. P. Avouac (2000), Modeling mountain building and the seismic cycle in the Himalaya of Nepal, *Journal of Geophysical Research-Solid Earth*, *105*(B6), 13389-13407.
12. Clark, M. K., and L. H. Royden (2000), Topographic ooze: Building the eastern margin of Tibet by lower crustal flow, *Geology*, *28*(8), 703-706.
13. Cohen, S. C. (1996), Convenient formulas for determining dip-slip fault parameters from geophysical observables, *Bulletin of the Seismological Society of America*, *86*(5), 1642-1644.
14. Croissant, T., D. Lague, P. Steer, and P. Davy (2017), Rapid post-seismic landslide evacuation boosted by dynamic river width, *Nat Geosci*, *10*, 680.
15. de Michele, M., D. Raucoules, J. de Sigoyer, M. Pubellier, and N. Chamot-Rooke (2010), Three-dimensional surface displacement of the 2008 May 12 Sichuan earthquake (China) derived from Synthetic Aperture Radar: evidence for rupture on a blind thrust, *Geophys J Int*, *183*(3), 1097-1103.

16. Dal Zilio, L., Y. van Dinther, T. Gerya, and J.-P. Avouac (2019), Bimodal seismicity in the Himalaya controlled by fault friction and geometry, *Nature Communications*, *10*(1), 48.
17. Densmore, A. L., R. N. Parker, N. J. Rosser, M. de Michele, Y. Li, R. Q. Huang, S. Whadcoat, and D. N. Petley (2012), Isostasy can't be ignored reply, *Nat Geosci*, *5*(2), 83-84.
18. Dreyfus, D., E. M. Rathje, and R. W. Jibson (2013), The influence of different simplified sliding-block models and input parameters on regional predictions of seismic landslides triggered by the Northridge earthquake, *Engineering Geology*, *163*, 41-54.
19. Elliott, J. R., R. Jolivet, P. J. González, J. P. Avouac, J. Hollingsworth, M. P. Searle, and V. L. Stevens (2016), Himalayan megathrust geometry and relation to topography revealed by the Gorkha earthquake, *Nat Geosci*, *9*, 174.
20. Fan, X., G. Domènech, G. Scaringi, R. Huang, Q. Xu, T. C. Hales, L. Dai, Q. Yang, and O. Francis (2018), Spatio-temporal evolution of mass wasting after the 2008 Mw 7.9 Wenchuan earthquake revealed by a detailed multi-temporal inventory, *Landslides*, *15*(12), 2325-2341.
21. Fielding, E. J., and D. McKenzie (2012), Lithospheric flexure in the Sichuan Basin and Longmen Shan at the eastern edge of Tibet, *Geophysical Research Letters*, *39*(9).
22. Fielding, E. J., A. Sladen, Z. H. Li, J. P. Avouac, R. Burgmann, and I. Ryder (2013), Kinematic fault slip evolution source models of the 2008 M7.9 Wenchuan earthquake in China from SAR interferometry, GPS and teleseismic analysis and implications for Longmen Shan tectonics, *Geophys J Int*, *194*(2), 1138-1166.
23. Galy, V., C. France-Lanord, O. Beyssac, P. Faure, H. Kudrass, and F. Palhol (2007), Efficient organic carbon burial in the Bengal fan sustained by the Himalayan erosional system, *Nature*, *450*(7168), 407-U406.
24. Gassenmeier, M., C. Sens-Schönfelder, T. Eulenfeld, M. Bartsch, P. Victor, F. Tilmann, and M. Korn (2016), Field observations of seismic velocity changes caused by shaking-induced damage and healing due to mesoscopic nonlinearity, *Geophys J Int*, *204*(3), 1490-1502.
25. Godard, V., R. Cattin, and J. Lave (2004), Numerical modeling of mountain building: Interplay between erosion law and crustal rheology, *Geophysical Research Letters*, *31*(23).
26. Godard, V., R. Cattin, and J. Lavé (2009), Erosional control on the dynamics of low-convergence rate continental plateau margins, *Geophys J Int*, *179*(2), 763-777.
27. Hanks, T. C., and H. Kanamori (1979), A moment magnitude scale, *Journal of Geophysical Research: Solid Earth*, *84*(B5), 2348-2350.
28. Harp, E. L., and R. W. Jibson (1996), Landslides triggered by the 1994 Northridge, California, earthquake, *Bulletin of the Seismological Society of America*, *86*(1B), S319-S332.
29. Hillers, G., P. M. Mai, Y. Ben-Zion, and J. P. Ampuero (2007), Statistical properties of seismicity of fault zones at different evolutionary stages, *Geophys J Int*, *169*(2), 515-533.
30. Hovius, N. (1996), Regular spacing of drainage outlets from linear mountain belts, *Basin Research*, *8*(1), 29-44.
31. Hovius, N., C. P. Stark, and P. A. Allen (1997), Sediment flux from a mountain belt derived by landslide mapping, *Geology*, *25*(3), 231-234.
32. Hovius, N., P. Meunier, L. Ching-Weei, C. Hongey, C. Yue-Gau, S. Dadson, H. Ming-Jame, and M. Lines (2011), Prolonged seismically induced erosion and the mass balance of a large earthquake, *Earth and Planetary Science Letters*, *304*(3-4), 347-355.
33. Huang, M.-H., R. Bürgmann, and A. M. Freed (2014), Probing the lithospheric rheology across the eastern margin of the Tibetan Plateau, *Earth and Planetary Science Letters*, *396*, 88-96.

34. Hubbard, J., and J. H. Shaw (2009), Uplift of the Longmen Shan and Tibetan plateau, and the 2008 Wenchuan (M=7.9) earthquake, *Nature, 458*(7235), 194-197.

35. Jibson, R. W., and D. K. Keefer (1993), Analysis of the seismic origin of landslides: Examples from the New Madrid seismic zone, *Geol Soc Am Bull*, *105*(4), 521-536.

36. Johnson, K. M., P. Segall, and S. B. Yu (2005), A viscoelastic earthquake cycle model for Taiwan, *Journal of Geophysical Research: Solid Earth*, *110*(B10).

37. Jordan, T. A., and A. B. Watts (2005), Gravity anomalies, flexure and the elastic thickness structure of the India–Eurasia collisional system, *Earth and Planetary Science Letters*, *236*(3), 732-750.

38. Keefer, D. K. (1994), The importance of earthquake-induced landslides to long-term slope erosion and slope-failure hazards in seismically active regions, *Geomorphology, 10*(1), 265-284.

39. Kelsey, H. M. (1990), Late Quaternary deformation of marine terraces on the Cascadia Subduction Zone near Cape Blanco, Oregon, Tectonics, 9(5), 983-1014.

40. King, G. C. P., R. S. Stein, and J. B. Rundle (1988), The Growth of Geological Structures by Repeated Earthquakes 1. Conceptual Framework, *Journal of Geophysical Research: Solid Earth*, *93*(B11), 13307-13318.

41. Lee, W. H. K., T. C. Shin, K. W. Kuo, K. C. Chen, and C. F. Wu (2001), CWB free-field strong-motion data from the 21 September Chi-Chi, Taiwan, earthquake, *Bull. Seismol. Soc. Am.*, 91(5), 1370–1376.

42. Leonard, M. (2010), Earthquake fault scaling: Self-consistent relating of rupture length, width, average displacement, and moment release, *Bulletin of the Seismological Society of America*, *100*(5A), 1971-1988.

43. Li, G., A. J. West, A. L. Densmore, Z. Jin, R. N. Parker, and R. G. Hilton (2014), Seismic mountain building: Landslides associated with the 2008 Wenchuan earthquake in the context of a generalized model for earthquake volume balance, *Geochemistry, Geophysics, Geosystems*, *15*(4), 833-844.

44. Li, G., A. J. West, A. L. Densmore, D. E. Hammond, Z. Jin, F. Zhang, J. Wang, and R. G. Hilton (2016), Connectivity of earthquake-triggered landslides with the fluvial network: Implications for landslide sediment transport after the 2008 Wenchuan earthquake, *Journal of Geophysical Research: Earth Surface*, *121*(4), 703-724.

45. Li, G., A. J. West, A. L. Densmore, Z. Jin, F. Zhang, J. Wang, M. Clark, and R. G. Hilton (2017), Earthquakes drive focused denudation along a tectonically active mountain front, *Earth and Planetary Science Letters*, *472*, 253-265.

46. Li, G., A. J. West, A. L. Densmore, Z. Jin, F. Zhang, J. Wang, and R. G. Hilton (2018), Distribution of earthquake-triggered landslides across landscapes: Towards understanding erosional agency and cascading hazards, in Y.-G. Li (Ed.), *Fault-Zone Guided Wave, Ground Motion, Landslide and 5180 Earthquake Forecast*, 160-190. Berlin, Boston: De Gruyter.

47. Li, X., Z. Zhou, H. Yu, R. Wen, D. Lu, M. Huang, Y. Zhou, and J. Cu (2008), Strong motion observations and recordings from the great Wenchuan earthquake, *Earthquake Eng. Eng. Vibr.*, 7(3), 235–246.

48. Jiang, J., and N. Lapusta (2016), Deeper penetration of large earthquakes on seismically quiescent faults, *Science*, *352*(6291), 1293-1297.

49. Li, Y., G. Zhang, X. Shan, Y. Liu, Y. Wu, H. Liang, C. Qu, and X. Song (2018), GPS-Derived Fault Coupling of the Longmenshan Fault Associated with the 2008 Mw Wenchuan 7.9

Earthquake and Its Tectonic Implications, *Remote Sensing*, *10*(5), 753.

50. Liu-Zeng, J., et al. (2009), Co-seismic ruptures of the 12 May 2008, Ms 8.0 Wenchuan earthquake, Sichuan: East-west crustal shortening on oblique, parallel thrusts along the eastern edge of Tibet, *Earth and Planetary Science Letters*, 286(3-4), 355-370.
51. Maggi, A., J. A. Jackson, D. McKenzie, and K. Priestley (2000), Earthquake focal depths, effective elastic thickness, and the strength of the continental lithosphere, *Geology*, *28*(6), 495-498.
52. Malamud, B. D., D. L. Turcotte, F. Guzzetti, and P. Reichenbach (2004), Landslides, earthquakes, and erosion, *Earth and Planetary Science Letters*, *229*(1–2), 45-59.
53. Marc, O., N. Hovius, P. Meunier, T. Uchida, and S. Hayashi (2015), Transient changes of landslide rates after earthquakes, *Geology*, *43*(10), 883-886.
54. Marc, O., N. Hovius, and P. Meunier (2016a), The mass balance of earthquakes and earthquake sequences, *Geophysical Research Letters*, *43*(8), 3708-3716.
55. Marc, O., N. Hovius, P. Meunier, T. Gorum, and T. Uchida (2016b), A seismologically consistent expression for the total area and volume of earthquake-triggered landsliding, *Journal of Geophysical Research: Earth Surface*, *121*(4), 2015JF003732.
56. Marc, O., P. Meunier, and N. Hovius (2017), Prediction of the area affected by earthquake-induced landsliding based on seismological parameters, *Nat. Hazards Earth Syst. Sci.*, *17*(7), 1159-1175.
57. Marc, O., R. Behling, C. Andermann, J. M. Turowski, L. Illien, S. Roessner, and N. Hovius (2019), Long-term erosion of the Nepal Himalayas by bedrock landsliding: the role of monsoons, earthquakes and giant landslides, *Earth Surf. Dynam.*, *7*(1), 107-128.
58. Maufroy, E., F. Cotton, V. M. Cruz−Atienza, and S. Gaffet (2014), Frequency-scaled curvature as a proxy for topographic site effect: amplification and groun motion variability, *Bulletin of the Seismological Society of America*, *105*(1), 354-367.
59. Meunier, P., N. Hovius, and J. A. Haines (2008), Topographic site effects and the location of earthquake induced landslides, *Earth and Planetary Science Letters, 275*(3-4), 221-232.
60. Meade, B. J. (2010), The signature of an unbalanced earthquake cycle in Himalayan topography?, *Geology*, *38*(11), 987-990.
61. Meunier, P., N. Hovius, and A. J. Haines (2007), Regional patterns of earthquake-triggered landslides and their relation to ground motion, *Geophysical Research Letters*, *34*(20).
62. Milliner, C. W. D., C. Sammis, A. A. Allam, J. F. Dolan, J. Hollingsworth, S. Leprince, and F. Ayoub (2016), Resolving Fine-Scale Heterogeneity of Co-seismic Slip and the Relation to Fault Structure, *Scientific reports*, *6*, 27201.
63. Molnar, P. (2012), Isostasy can't be ignored, *Nat Geosci*, *5*(2), 83-83.
64. Molnar, P., and P. England (1990), Late Cenozoic uplift of mountain ranges and global climate change: chicken or egg?, *Nature*, *346*(6279), 29-34.
65. Muenchow, J., A. Brenning, and M. Richter (2012), Geomorphic process rates of landslides along a humidity gradient in the tropical Andes, *Geomorphology*, *139-140*, 271-284.
66. Okada, Y. (1992), Internal Deformation Due to Shear and Tensile Faults in a Half-Space, *Bulletin of the Seismological Society of America*, *82*(2), 1018-1040.
67. Parker, R. N., A. L. Densmore, N. J. Rosser, M. de Michele, Y. Li, R. Q. Huang, S. Whadcoat, and D. N. Petley (2011), Mass wasting triggered by the 2008 Wenchuan earthquake is greater than orogenic growth, *Nat Geosci*, *4*(7), 449-452.

68. Parker, R. N., G. T. Hancox, D. N. Petley, C. I. Massey, A. L. Densmore, and N. J. Rosser (2015), Spatial distributions of earthquake-induced landslides and hillslope preconditioning in the northwest South Island, New Zealand, *Earth Surf. Dynam.*, *3*(4), 501-525.

69. Perron, J. T. (2017), Climate and the Pace of Erosional Landscape Evolution, *Annual Review of Earth and Planetary Sciences*, *45*(1), 561-591.

70. Raymo, M. E., W. F. Ruddiman, and P. N. Froelich (1988), Influence of late Cenozoic mountain building on ocean geochemical cycles, *Geology*, *16*(7), 649-653.

71. Ren, Z., Z. Zhang, H. Zhang, W. Zheng, and P. Zhang (2018), The Role of the 2008 Mw 7.9 Wenchuan Earthquake in Topographic Evolution: Seismically Induced Landslides and the Associated Isostatic Response, *Tectonics*, 37(9), 2748-2757.

72. Savage, J. C. (1983), A dislocation model of strain accumulation and release at a subduction zone, *Journal of Geophysical Research: Solid Earth*, *88*(B6), 4984-4996.

73. Savage, J. C., and G. Gu (1985), A plate flexure approximation to postseismic and interseismic deformation, *Journal of Geophysical Research: Solid Earth*, *90*(B10), 8570-8580.

74. Scheingross, J. S., B. M. Minchew, B. H. Mackey, M. Simons, M. P. Lamb, and S. Hensley (2013), Fault-zone controls on the spatial distribution of slow-moving landslides, *GSA Bulletin*, *125*(3-4), 473-489.

75. Scholz, C. H. (2002), The Mechanics of Earthquakes and Faulting, 2nd ed., 471 pp., Cambridge Univ. Press, Cambridge, U. K.

76. Scholz, C. H., and J. Campos (2012), The seismic coupling of subduction zones revisited, *Journal of Geophysical Research: Solid Earth*, *117*(B5).

77. Simpson, G. (2014), Decoupling of foreland basin subsidence from topography linked to faulting and erosion, *Geology*, *42*(9), 775-778.

78. Simpson, G. (2015), Accumulation of permanent deformation during earthquake cycles on reverse faults, *Journal of Geophysical Research: Solid Earth*, *120*(3), 1958-1974.

79. Stevens, V. L., and J. P. Avouac (2015), Interseismic coupling on the main Himalayan thrust, Geophysical Research Letters, 42(14), 5828-5837.

80. Stirling, M., et al. (2012), National Seismic Hazard Model for New Zealand: 2010 UpdateNational Seismic Hazard Model for New Zealand: 2010 Update, *Bulletin of the Seismological Society of America*, *102*(4), 1514-1542.

81. Sun, T., et al. (2014), Prevalence of viscoelastic relaxation after the 2011 Tohoku-oki earthquake, *Nature*, *514*, 84.

82. Tanyaş, H., et al. (2017), Presentation and Analysis of a Worldwide Database of Earthquake-Induced Landslide Inventories, *Journal of Geophysical Research: Earth Surface*, *122*(10), 1991-2015.

83. Tapponnier, P., X. Zhiqin, F. Roger, B. Meyer, N. Arnaud, G. Wittlinger, and Y. Jingsui (2001), Oblique Stepwise Rise and Growth of the Tibet Plateau, *Science*, *294*(5547), 1671-1677.

84. Thatcher, W., and J. B. Rundle (1984), A viscoelastic coupling model for the cyclic deformation due to periodically repeated Earthquakes at subduction zones, *Journal of Geophysical Research: Solid Earth*, *89*(B9), 7631-7640.

85. Torres, M. A., A. J. West, and G. Li (2014), Sulphide oxidation and carbonate dissolution as a source of CO2 over geological timescales, *Nature*, *507*(7492), 346-349.

86. Theunissen, T., Y. Font, S. Lallemand, and W.-T. Liang (2010), The largest instrumentally recorded earthquake in Taiwan: revised location and magnitude, and tectonic significance of the

1920 event, *Geophys J Int*, *183*(3), 1119-1133.

87. Vanmaercke, M., F. Ardizzone, M. Rossi, and F. Guzzetti (2017), Exploring the effects of seismicity on landslides and catchment sediment yield: An Italian case study, *Geomorphology*, 278, 171-183.
88. Vergne, J., R. Cattin, and J. P. Avouac (2001), On the use of dislocations to model interseismic strain and stress build-up at intracontinental thrust faults, *Geophys J Int*, *147*(1), 155-162.
89. Vita-Finzi, C. (2000), Deformation and seismicity of Taiwan, *Proceedings of the National Academy of Sciences*, *97*(21), 11176-11180.
90. Wang, J., Z. Jin, R. G. Hilton, F. Zhang, A. L. Densmore, G. Li, and A. J. West (2015), Controls on fluvial evacuation of sediment from earthquake-triggered landslides, *Geology*, 43 (2): 115-118.
91. Wang, H., M. Liu, X. Shen, and J. Liu (2010), Balance of seismic moment in the Songpan-Ganze region, eastern Tibet: Implications for the 2008 Great Wenchuan earthquake, *Tectonophysics*, *491*(1), 154-164.
92. Watts, A. B. (2001), *Isostacy and flexure of the lithosphere*, Cambridge University Press, Cambridge.
93. Wells, D. L., and K. J. Coppersmith (1994), New Empirical Relationships among Magnitude, Rupture Length, Rupture Width, Rupture Area, and Surface Displacement, *Bulletin of the Seismological Society of America*, *84*(4), 974-1002.
94. Wesnousky, S. G. (1988), Seismological and structural evolution of strike-slip faults, *Nature*, *335*, 340.
95. Whipple, K. X., M. Shirzaei, K. V. Hodges, and J. Ramon Arrowsmith (2016), Active shortening within the Himalayan orogenic wedge implied by the 2015 Gorkha earthquake, *Nature Geoscience*, *9*, 711.
96. Wolman, M. G., and J. P. Miller (1960), Magnitude and Frequency of Forces in Geomorphic Processes, *The Journal of geology*, *68*(1), 54-74.
97. Xu, C., X. Xu, X. Yao, and F. Dai (2014), Three (nearly) complete inventories of landslides triggered by the May 12, 2008 Wenchuan Mw 7.9 earthquake of China and their spatial distribution statistical analysis, *Landslides*, *11*(3), 441-461.
98. Yanites, B. J., G. E. Tucker, K. J. Mueller, and Y. G. Chen (2010), How rivers react to large earthquakes: Evidence from central Taiwan, *Geology*, *38*(7), 639-642.
99. Zhang, P.-Z., et al. (2004), Continuous deformation of the Tibetan Plateau from global positioning system data, *Geology*, *32*(9), 809-812.
100. Zhang, S., L. M. Zhang, and T. Glade (2014), Characteristics of earthquake- and rain-induced landslides near the epicenter of Wenchuan earthquake, *Engineering Geology*, 175, 58-73.

Figures (14 figures in the main text + 3 figures in the appendix)

Figure 1.

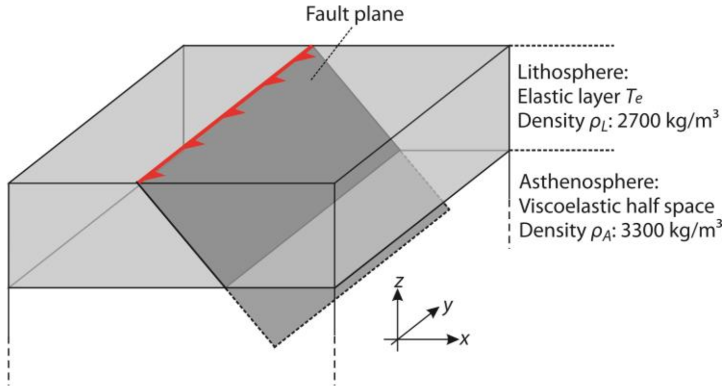

Figure 1. Illustrated diagram of the fault setting modeled in this study, composed of elastic lithosphere with thickness T_e and density ρ_L, viscoelastic asthenosphere with density ρ_A, and a thrust fault plane with dip θ. The fault plane is assumed to be large enough to accommodate all earthquake magnitudes of interest (up to M_w8-9 in this context), and the rupture dimensions are determined from M_w-based scaling relations for dip-slip fault earthquakes (cf. Table 6, Leonard, 2010).

Figure 2.

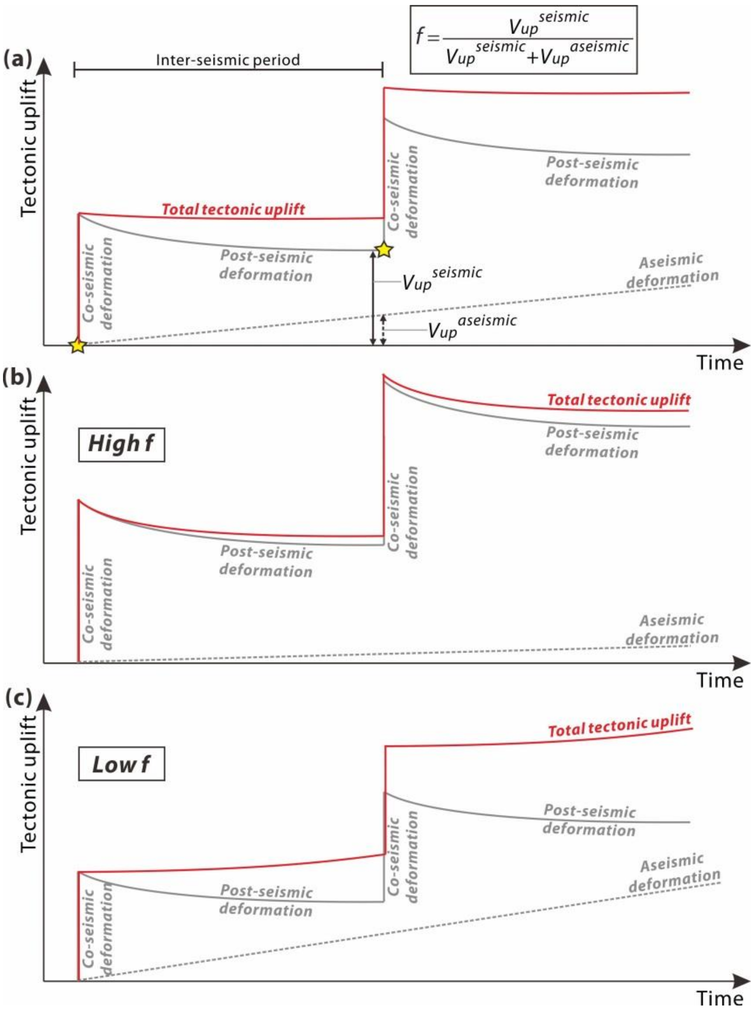

Figure 2. Schematic diagrams of seismic and aseismic deformation of the fault zone over earthquake cycles, the meaning of factor *f*, and two cases of high and low *f*. (a) Tectonic uplift versus time in the context of earthquake cycles: total tectonic uplift (red solid curve) is composed of co-seismic (gray solid line, occurring during earthquakes represented by the yellow stars), post-seismic (gray solid curve) and aseismic (gray dashed curve) deformations. (b) Tectonic uplift versus time in a high *f* case where seismic deformation contributes most to total uplift, i.e., high inter-seismic coupling as observed in the Himalayas (Stevens and Avouac, 2015). (c) Tectonic uplift versus time in a low *f* case where aseismic uplift is significant. Note that these schematic diagrams are for regional loading scenarios where inter-seismic deformation at the fault zone is neglected, whereas in localized loading scenarios deformation may show different trends over time (e.g. Cattin and Avouac, 2000; Simpson, 2015).

Figure 3.

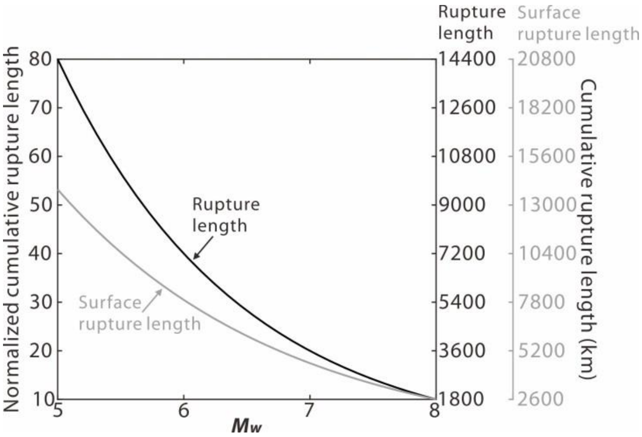

Figure 3. Cumulative rupture length as a function of earthquake magnitude over 10 M_w8 earthquake cycles concerning rupture length (subsurface) and surface rupture length. The normalized cumulative rupture length is normalized by the rupture length of one single maximum magnitude (M_w = 8 in this case) event, which is assumed to be equivalent to the full fault length. Smaller magnitude earthquakes rupture different segments of the fault. Rupture length is calculated using the M_w-based empirical scaling relationships for dip-slip fault earthquakes reported in Leonard (2010).

Figure 4.

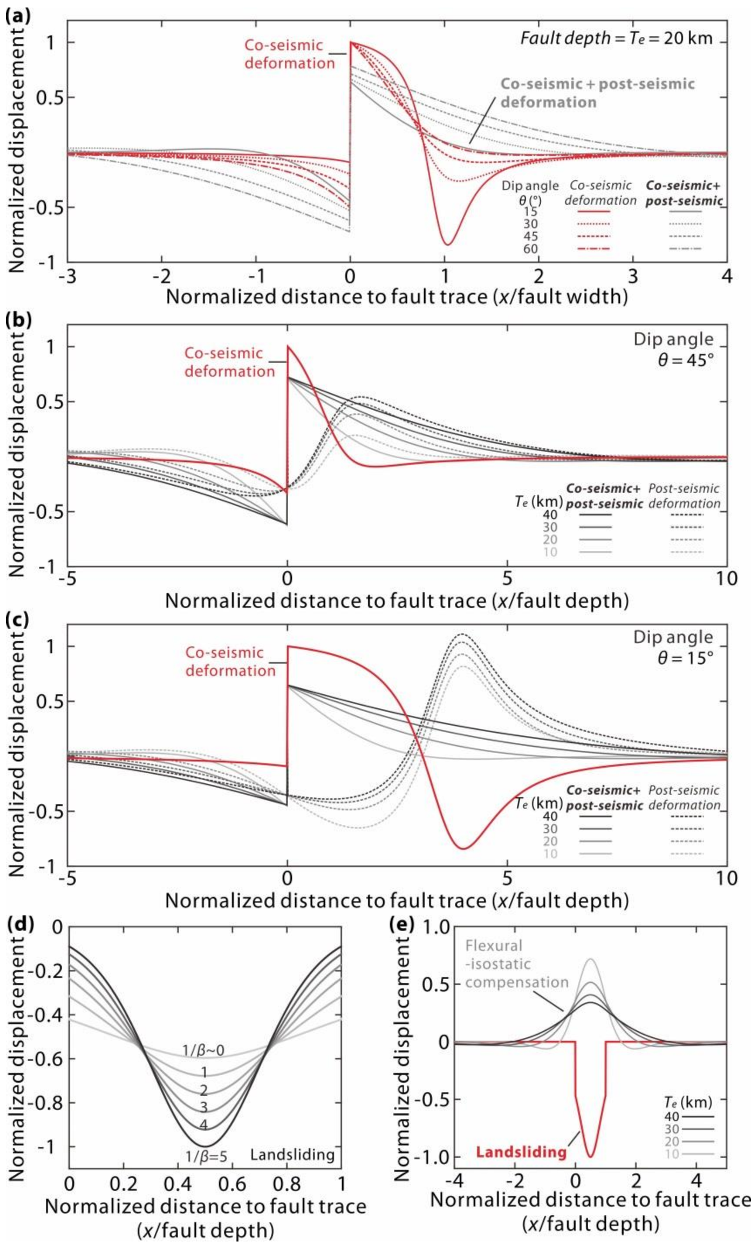

Figure 4. Spatial patterns of seismically induced deformations over full earthquake cycles and variations over controlling parameters. (a) Normalized vertical displacements of co-seismic deformation (red lines) and the combined co-seismic and post-seismic deformation (gray curves) with varying fault dip and T_e values versus distance to fault trace normalized by fault width. (b) Normalized vertical displacements caused by co-seismic deformation (red lines), post-seismic deformation (dashed gray curves) and the combined co-seismic and post-seismic deformation (solid gray curves) with a fault dip θ of 45° and varying T_e values versus distance to fault trace normalized by fault depth, and the same type of results for a fault dip θ of 15° is plotted in (c). (d) Normalized vertical displacement of landslide erosion as a

function of landslide spatial pattern factor β. (e) Normalized vertical displacement of flexural-isostatic compensation to landslide erosion ($\beta = 1$) over changing T_e. In (d) and (e), the modeled landslides are set to occur only on the hanging wall (x/fault depth > 0). Note the different horizontal scales in the x-axes, and the x-axis in (a) is normalized to fault width whereas for other panels the x-axis is normalized to fault depth (fault depth = fault width × sinθ). Here we consider earthquake rupture depth is equal to fault depth and T_e.

Figure 5.

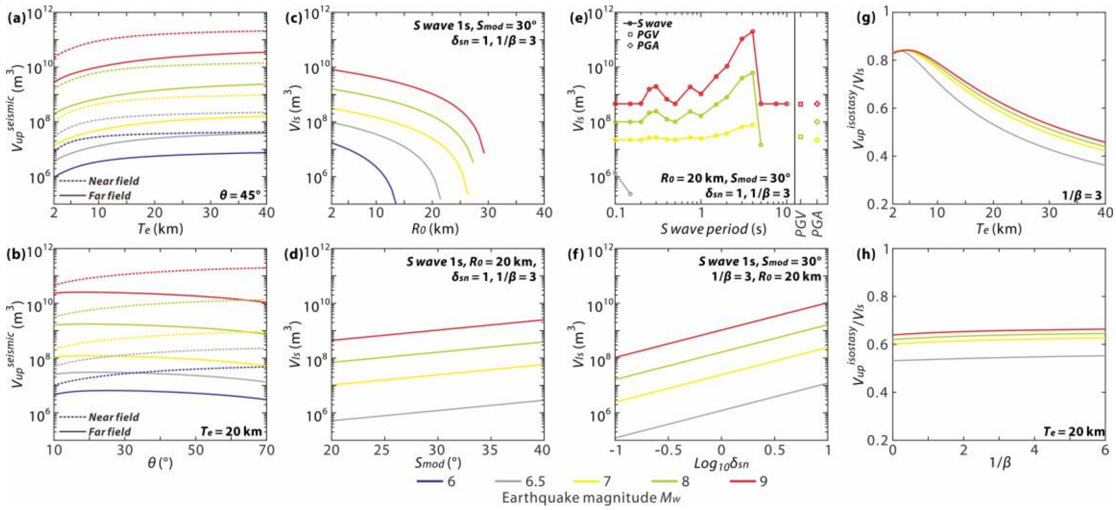

Figure 5. Seismically induced volumes and the isostatic ratio over input parameters and assumptions about landslide-triggering factors, including $V_{up}^{seismic}$ versus (a) T_e and (b) θ; V_{ls} versus (c) R_0, (d) S_{mod}, (e) assumed landslide-triggering factor including seismic waves of different frequencies, PGV, and PGA; near field isostasy ratio versus (g) T_e, (f) δ_{sn}, and (h) $1/\beta$. $V_{up}^{seismic}$ considers both far field and near field scenarios, i.e., the solid and dashed lines in (a) and (b), respectively. Adopted values of relevant model parameters are reported in each panel.

Figure 6.

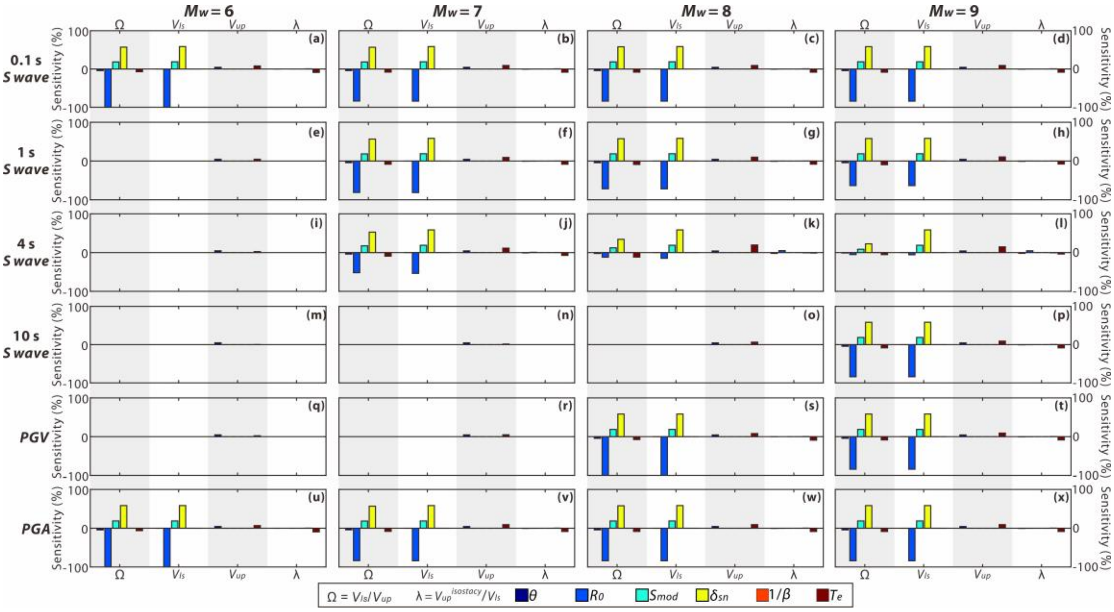

Figure 6. Sensitivity analysis of earthquake volume balance ratio Ω, V_{ls}, V_{up} and λ to changes in the studied parameters over different earthquake magnitudes and seismological factors responsible for triggering landslides (e.g. S waves of different periods, *PGV* and *PGA*) for near field scenario. Panels showing blank results (e.g. panels e, i, m and q) mean no landslides are triggered with the given conditions. The signs indicate the changes of the ratios and uplift volumes when increasing a parameter: positive means increase and negative means decrease.

Figure 7.

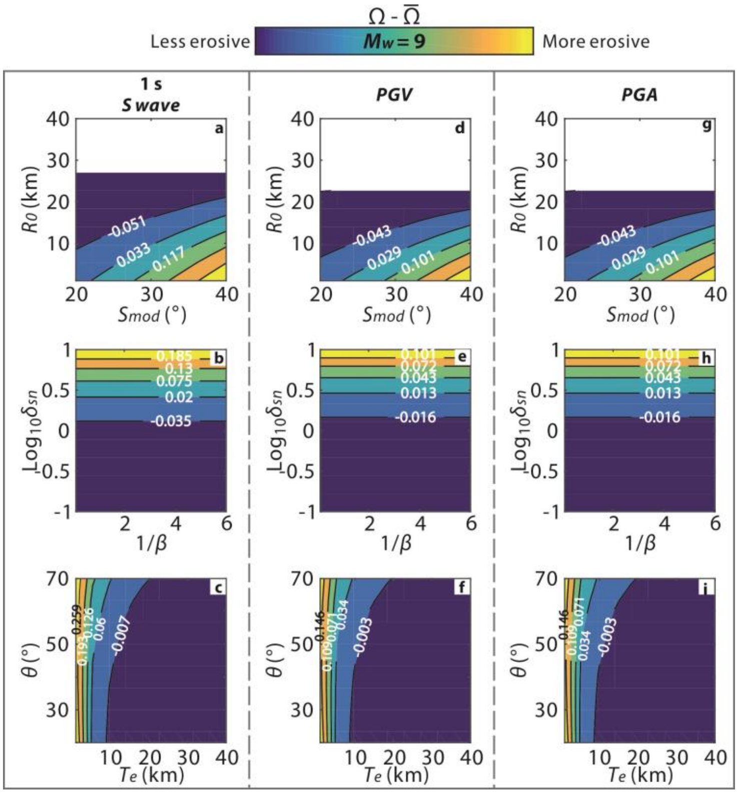

Figure 7. Contour plots of the relative earthquake volume balance ratio, defined as the difference between the earthquake volume balance ratio Ω and the average volume balance ratio $\overline{\Omega}$ over the sampling space. We consider M_w=9 here and a range of representative seismological factors (S wave of 1 s period, *PGV* and *PGA*) responsible for triggering landslides in a far field scenario. Blank areas (on panels a, d, and g) represent no landslides being triggered for the given conditions. The values of the input parameters and sampling ranges are detailed in Section 3.6. Please see more contour plots for various earthquake magnitudes and a more complete set of landslide-triggering factors in the Appendix.

Figure 8.

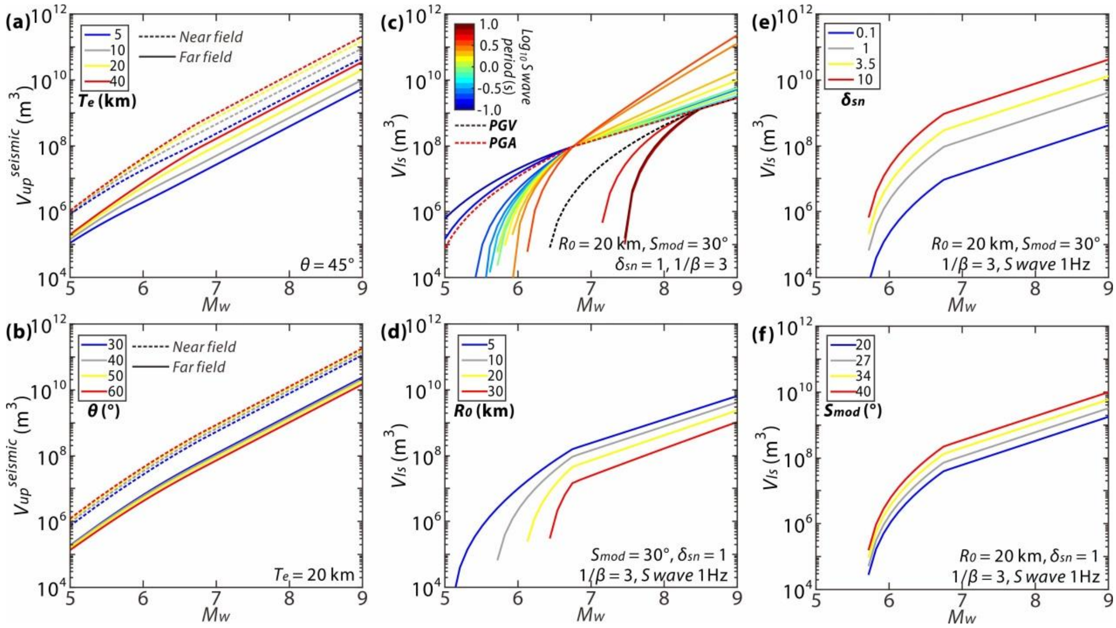

Figure 8. Variations of seismically induced uplift and landslide volumes across earthquake magnitudes over different parameters and possible seismological landslide-triggering factors. (a) $V_{up}^{seismic}$ versus M_w under changing T_e (colored) in near field (dashed lines) and far field (solid lines) scenarios. (b) $V_{up}^{seismic}$ versus M_w under changing θ (colored) in near field (dashed lines) and far field (solid lines) scenarios. (c) V_{ls} versus M_w under changing seismological factors responsible for triggering landslides. (d) V_{ls} versus M_w under changing seismological factors responsible for triggering landslides. (e) V_{ls} versus M_w under changing landscape failure susceptibility. (f) V_{ls} versus M_w under changing landscape steepness. Adopted values of relevant model parameters are reported in each panel.

Figure 9.

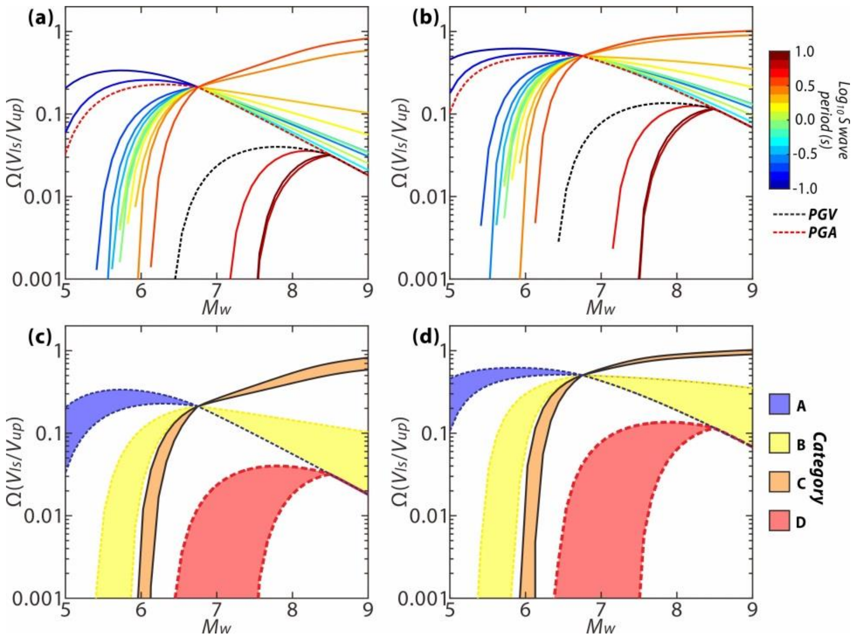

Figure 9. Earthquake volume balance ratio across earthquake magnitudes over possible seismological factors responsible for triggering landslides, accounting for (a) near field and (b) far field scenarios. (c) and (d) illustrate the representative patterns (color-labeled as category A, B, C and D) as plotted in (a) and (b), respectively. The related parameters are set at their medians of the ranges reported in Section 2.7. The input parameters are: θ = 45°, T_e = 20 km, R_0 =10 km, S_{mod} = 30°, $1/\beta$ = 1, and δ_{sn} = 1.

Figure 10.

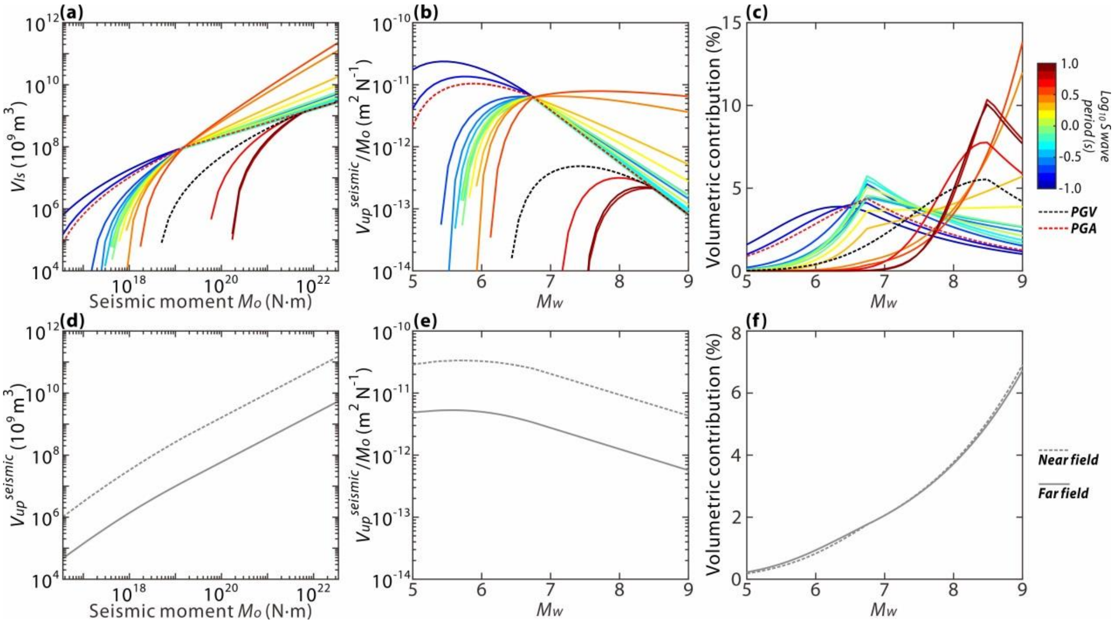

Figure 10. Seismically induced uplift and landslide volumes versus seismic moment release and earthquake magnitude. (a) V_{ls} versus M_o under changing seismological factors responsible for triggering landslides. (b) V_{ls}/M_o versus M_w under changing seismological factors responsible for triggering landslides. (c) Contribution to the total landslide volume over multiple earthquake cycles versus M_w, considering changing seismological factors responsible for triggering landslides. For V_{ls} calculations, the input parameters are: R_0 =1-40 km, S_{mod} = 30°, δ_{sn} = 1, and $1/\beta$ = 1. (d) $V_{up}^{seismic}$ versus M_o for near field (dashed curve) and far field (solid curve) scenarios. (e) $V_{up}^{seismic}/M_o$ versus M_w for near field (dashed curve) and far field (solid curve) scenarios. (f) Contribution to the total seismic uplift volume over multiple earthquake cycles versus M_w, considering near field (dashed curve) and far field (solid curve) cases. For $V_{up}^{seismic}$ calculations, we choose θ = 45°, T_e = 20 km, and determine rupture dimensions using M_w-based scaling relations and earthquake depth combining fault width and dip angle.

Figure 11.

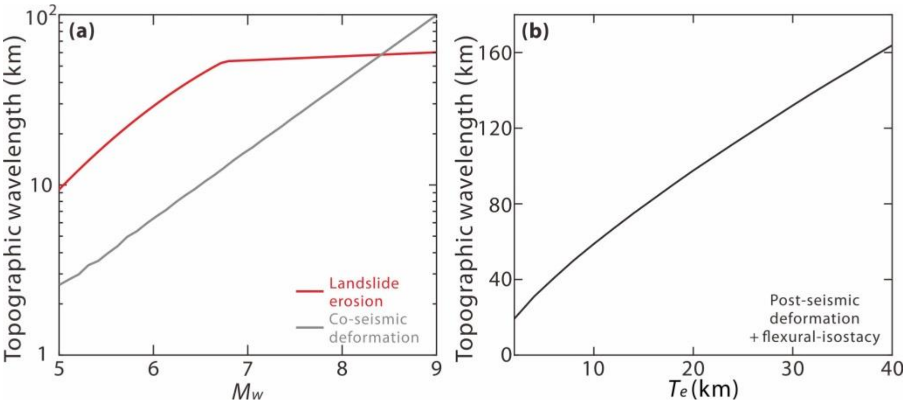

Figure 11. Wavelength of seismically produced topography versus (a) M_w and (b) T_e, considering topographic wavelength caused by (a) co-seismic deformation (gray curve, wavelength defined as the horizontal range within 20% of maximum deformation), landslide erosion (red curve, wavelength defined as the horizontal width of the full landslide erosion zone, using the relation from Marc et al., 2017) as a function of earthquake magnitude, and (b) post-seismic processes (the sum of inter-seismic relaxation and flexural-isostatic compensation). For (a), we set $\theta = 45°$, $1/\beta = 1$, $S_{mod} = 30°$, $\delta_{sn} = 1$, and assume landslides are mainly triggered by 1 Hz (period = 1 s) seismic waves. R_0 is assumed to be equivalent to the fault depth (fault width × sinθ) for simplicity (Marc et al., 2016b). Fault width is calculated using the scaling relations in Leonard (2010). For (b), we test earthquake magnitudes from 5 to 9 and the trends maintain similar, with varying T_e and other parameters same as in (a).

Figure 12.

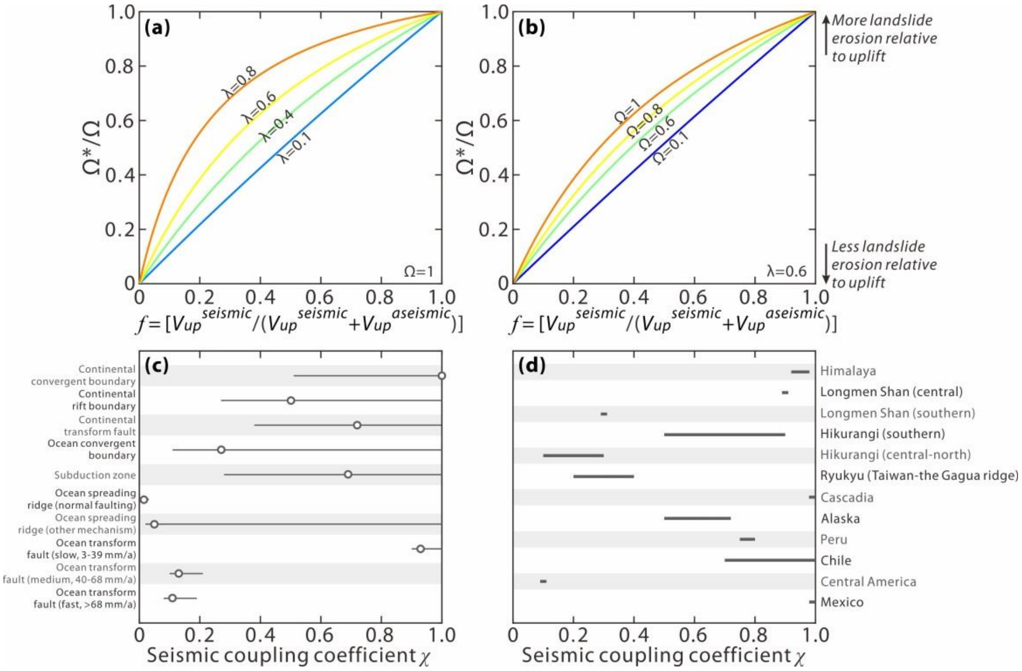

Figure 12. Ω^*/Ω (volume balance ratio accounting for both seismic and aseismic uplift : seismic volume balance ratio) as a function of *f*, the proportion of seismically induced uplift relative to the total uplift caused by seismic and aseismic deformations over one seismic cycle, under changing (a) isostatic response coefficient λ and (b) seismic volume balance ratio Ω. Although there are no direct measurement of *f*, we use the seismic coupling coefficient χ, the proportion of seismic slip over long-term slip, as a first-order approximation of *f*. (c) χ values in typical tectonic settings as compiled by Bird and Kagan (2004), with error bars indicating 95% confidence intervals. (d) χ values in major tectonically compressional regions and convergent plate boundary systems with error bars indicating uncertainties from spatial variations and/or calculation method: the Himalayas (Ader et al., 2012), the Longmen Shan mountain range at the eastern margin of the Tibetan Plateau (Li et al., 2018b), the Hikurangi subduction system (Stirling et al., 2012), the Ryukyu subduction system (Taiwan-Gagua ridge, Theunissen et al., 2010), Cascadia, Alaska, Chile, and Mexico (Scholz and Campos, 2012), and the central America as an example of low χ-region (Scholz and Campos, 2012).

Figure 13.

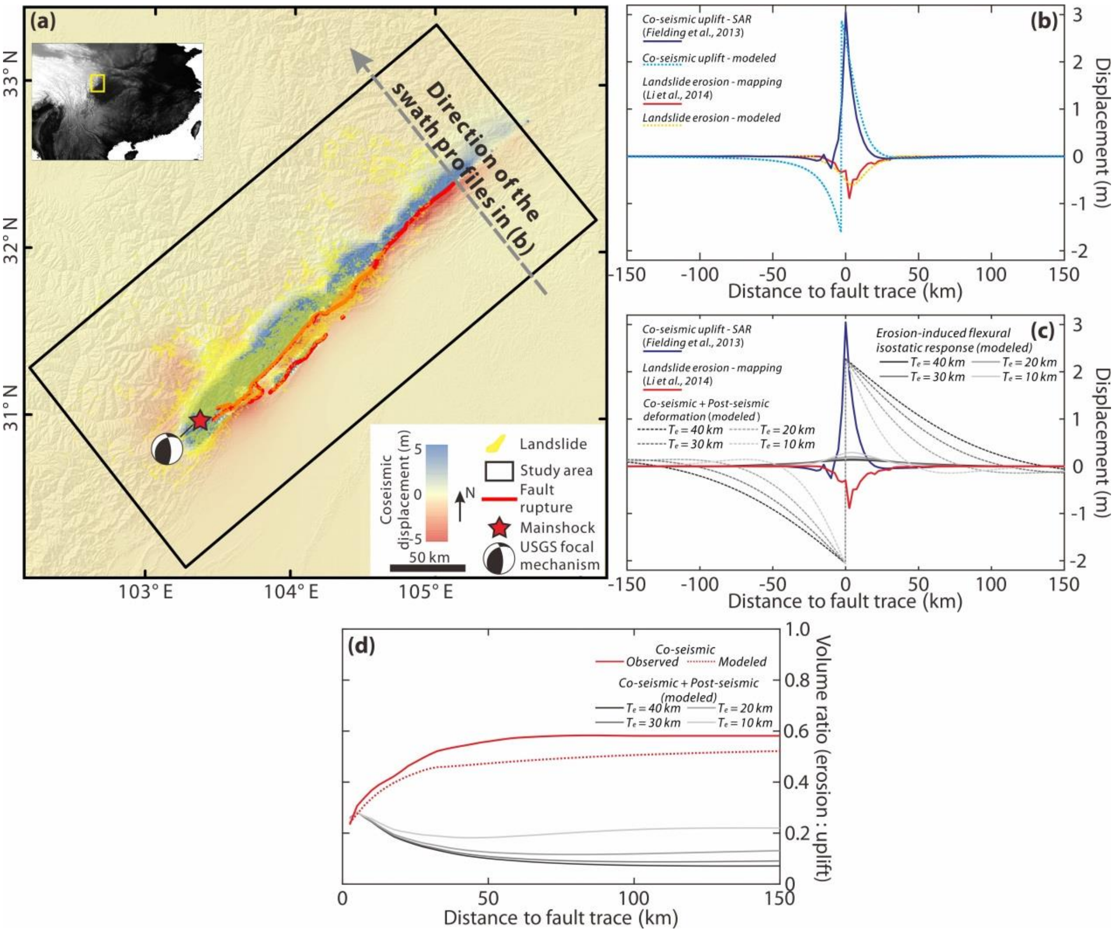

Figure 13. Spatial variations of seismically induced deformations for the 2008 M_w7.9 Wenchuan case. (a) Mapview of the epicentral region of the Wenchuan earthquake, with co-seismic displacement and distribution of earthquake-triggered landslides. (b) Vertical displacement caused by co-seismic deformation and landslide erosion derived from observations and modeling. Model parameters are determined from the Wenchuan field data, with $\theta = 65°$, $1/\beta = 0.68$, $S_{mod} = 31°$, $\delta_{sn} = 5$, $R_0 = 9.5$ km, assuming 1 Hz seismic waves are the main seismological factor responsible for triggering landsliding (Liu-Zeng et al., 2009; Xu et al., 2009; Marc et al., 2016b; Li et al., 2017; Li et al., 2018). (c) Displacement of seismically induced deformations (co-seismic deformation, landslide erosion, combined co-seismic and post-seismic deformation, flexural isostatic response to landslide erosion) projected along the direction perpendicular to the fault trace, i.e. the grey arrow in (a). (d) Volume ratio between landslide erosion and seismically induced uplift on the hanging wall for the observed and modeled co-seismic case (solid and dashed red curves, respectively) and over the full earthquake cycle (gray curves) versus the distance to fault trace, with T_e of 10, 20, 30 and 40 km.

Figure 14.

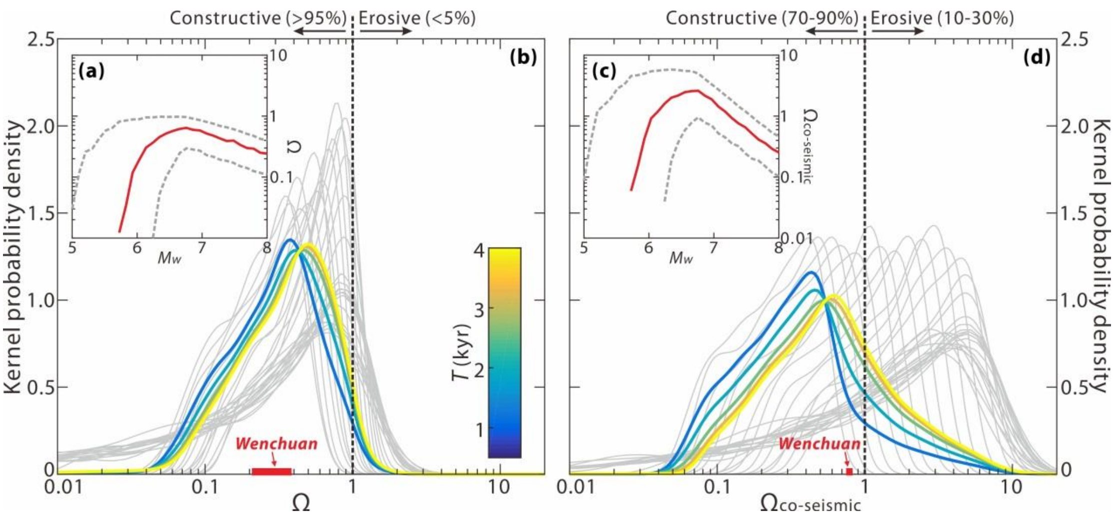

Figure 14. Volume balance and the overall topographic effects of earthquake cycles at the eastern margin of the Tibetan Plateau modeled via Monte Carlo random sampling of T_e (7-40 km) and R_0 (1-20 km) for earthquake events with M_w ~5-8. Other model parameters are determined from the Wenchuan field data, considering hanging wall, near field scenarios. (a) Seismic volume balance ratio (Ω, landslide erosion : uplift) versus M_w: 1000 times' Monte Carlo simulations are run for each earthquake magnitude bin ($\Delta M_w = 0.1$) to account for variations of T_e and R_0; the results are reported as the medians (red solid curve) and an envelope bounded by the 16th-84th percentiles (gray dashed curves) of the modeled Ω population. (b) Kernel probability density of Ω for each earthquake magnitude bin (gray curves, with each curve representing the probability density for the 1000 Ω values from the Monte Carlo simulations for a specified M_w bin) and for the average of Ω weighted by seismic uplift and occurrence frequency of each M_w bin (colored curves) considering different estimates of the recurrence time of Wenchuan-like events, T, as indicated by the colored curves and the color bar. Our results suggest the overall topographic effect of earthquake cycles tends to be constructive (with >90% probability for $\Omega < 1$) rather than erosive (with <10% probability for $\Omega > 1$). The red bar indicates the Wenchuan event. (c) and (d) are for co-seismic scenarios ($\Omega_{\text{co-seismic}} = V_{ls}/V_{up}^{co\text{-}seismic}$), with the red square on (d) representing the Wenchuan case.

Appendix

Figure A1.

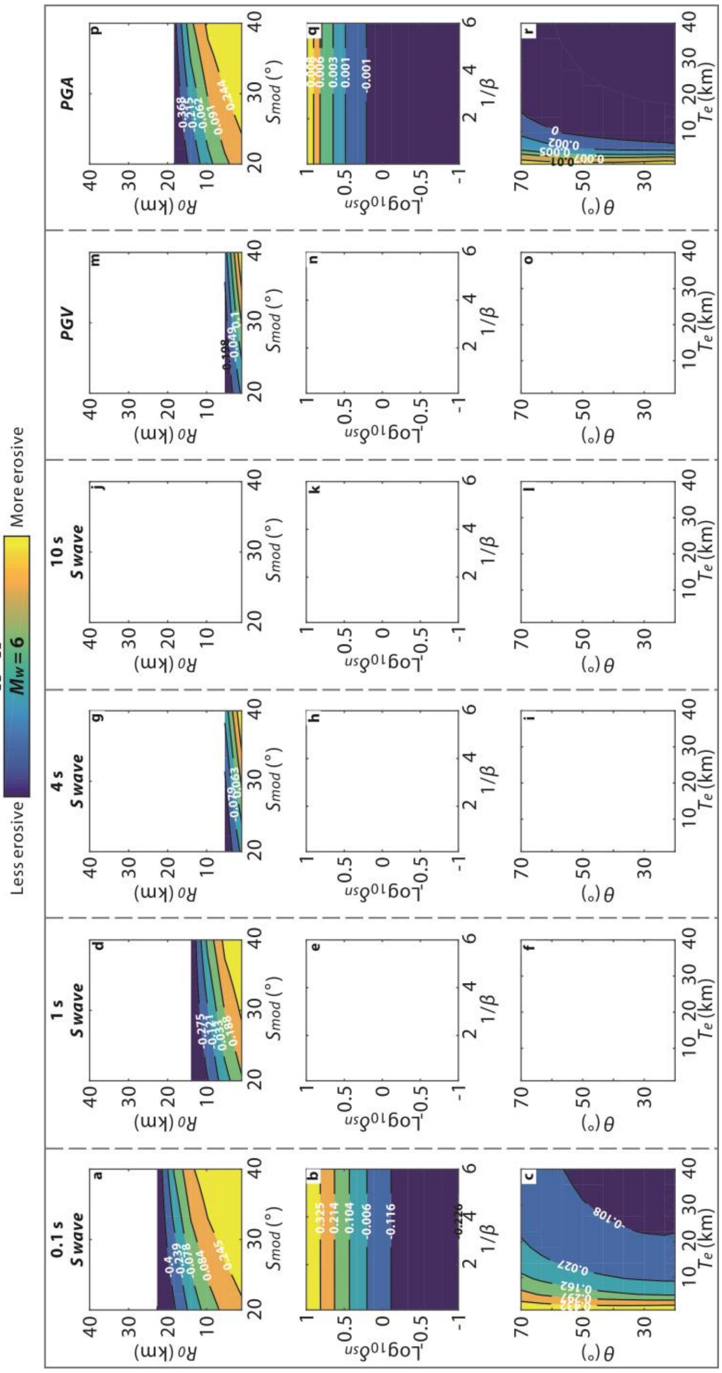

Figure A1. Contour plots of the relative earthquake volume balance ratio, defined as the difference between the earthquake volume balance ratio Ω and the average volume balance ratio $\overline{\Omega}$ over the sampling space. We consider M_w=6 here and a range of seismological factors (S waves of different periods, *PGV* and *PGA*) responsible for triggering landslides in a far field scenario. Blank areas represent no landslides being triggered for the given conditions.

Figure A2.

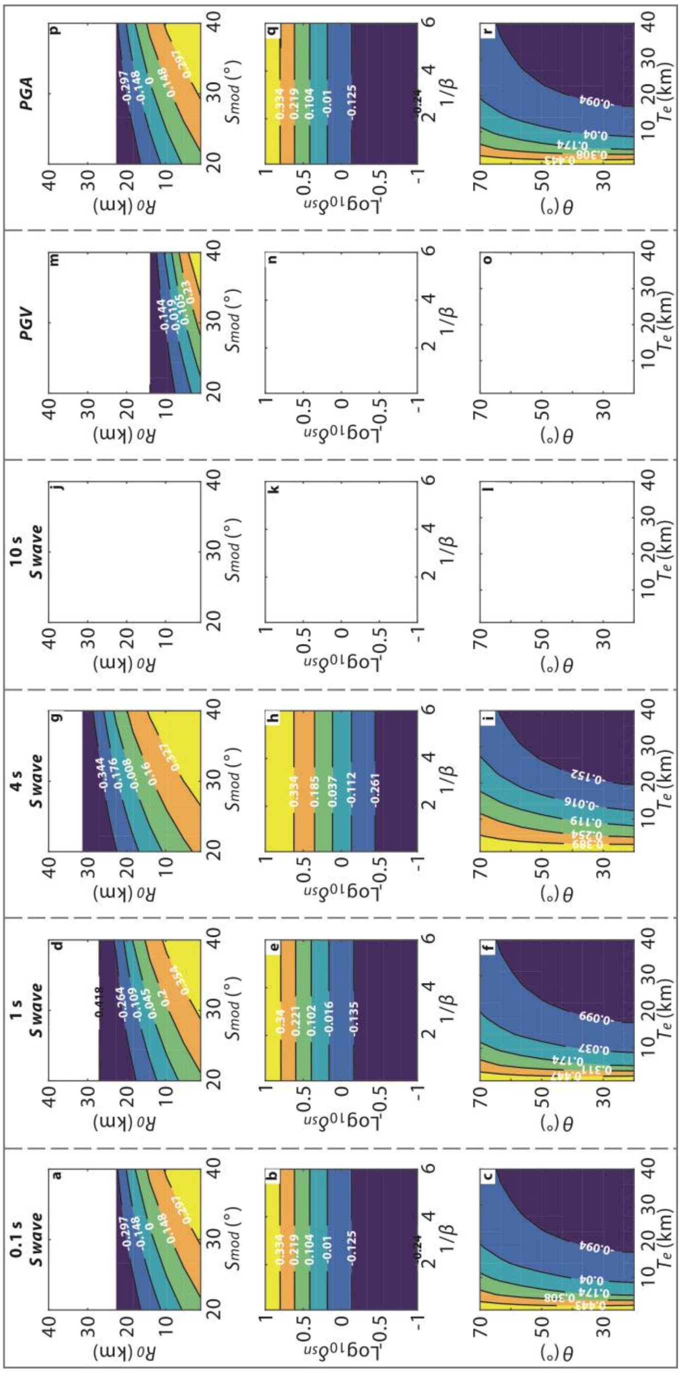

Figure A2. Contour plots of the relative earthquake volume balance ratio, defined as the difference between the earthquake volume balance ratio Ω and the average volume balance ratio $\overline{\Omega}$ over the sampling space. We consider M_w= 7 here and a range of seismological factors (S waves of different periods, *PGV* and *PGA*) responsible for triggering landslides in a far field scenario. Blank areas represent no landslides being triggered for the given conditions.

Figure A3.

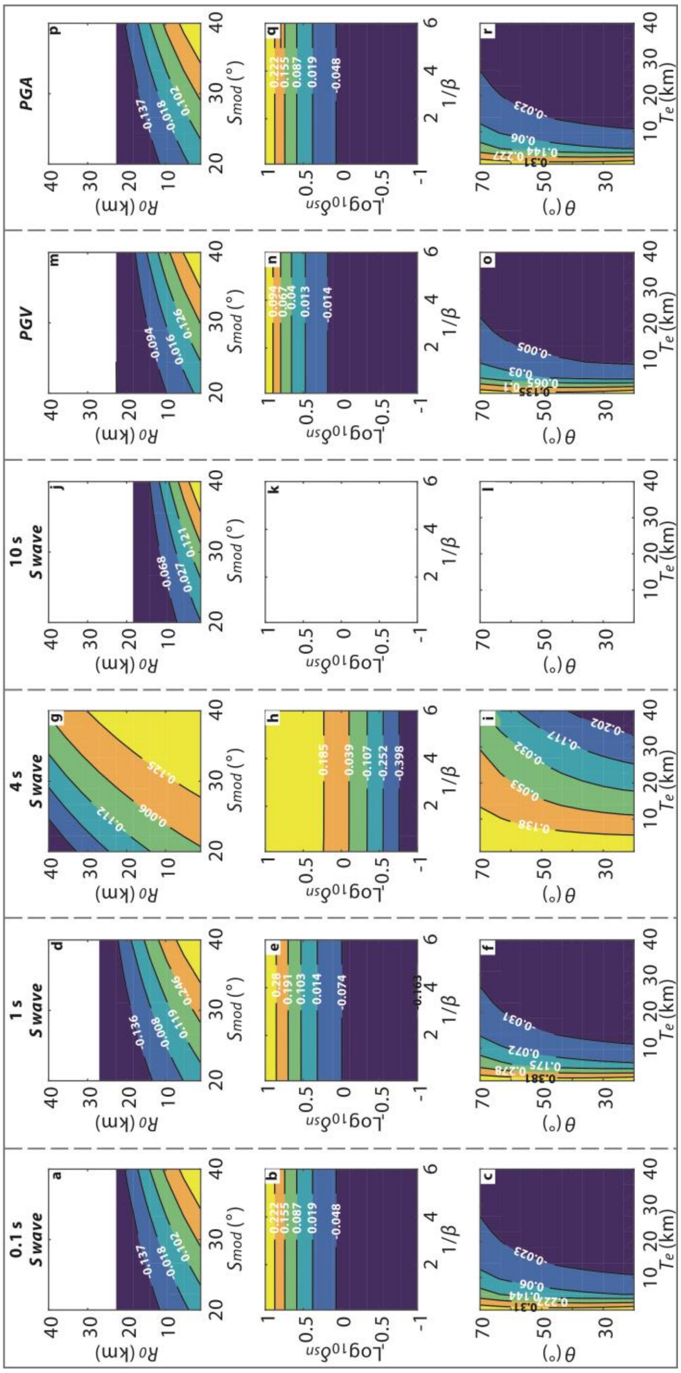

Figure A3. Contour plots of the relative earthquake volume balance ratio, defined as the difference between the earthquake volume balance ratio Ω and the average volume balance ratio $\overline{\Omega}$ over the sampling space. We consider M_w= 8 here and a range of seismological factors (S waves of different periods, *PGV* and *PGA*) responsible for triggering landslides in a far field scenario. Blank areas represent no landslides being triggered for the given conditions.

Figure A4.

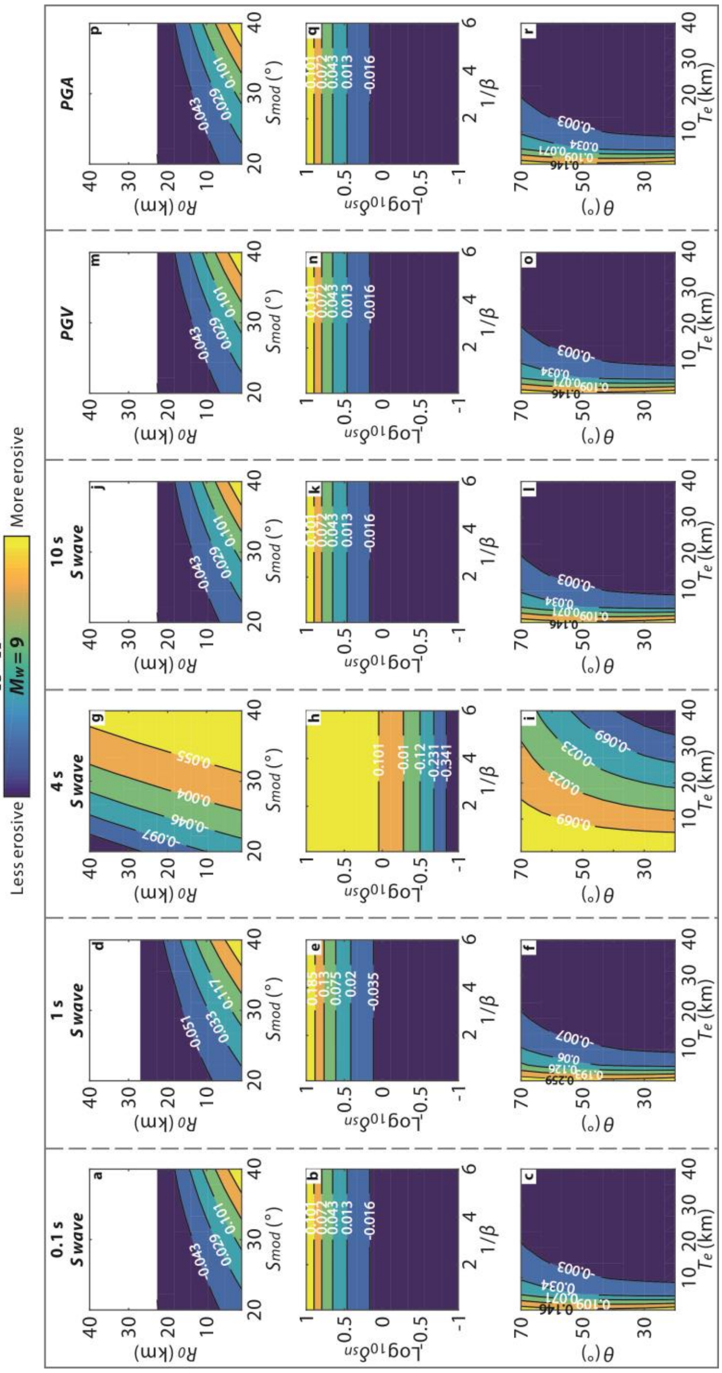

Figure A4. Contour plots of the relative earthquake volume balance ratio, defined as the difference between the earthquake volume balance ratio Ω and the average volume balance ratio $\overline{\Omega}$ over the sampling space. We consider M_w= 9 here and a range of seismological factors (S waves of different periods, *PGV* and *PGA*) responsible for triggering landslides in a far field scenario. Blank areas represent no landslides being triggered for the given conditions.

Figure01.

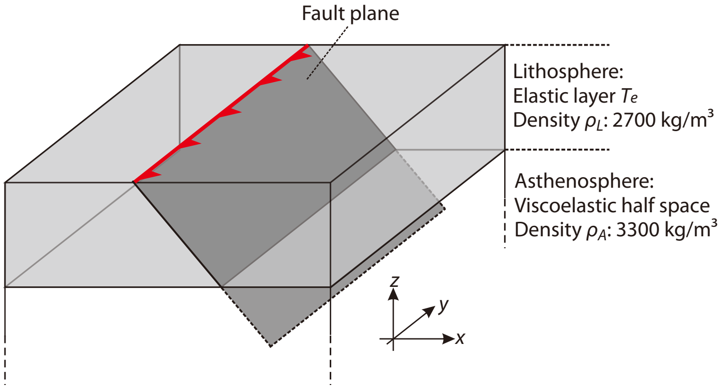

Fault plane
Lithosphere:
Elastic layer T_e
Density ρ_L: 2700 kg/m^3
Asthenosphere:
Viscoelastic half space
Density ρ_A: 3300 kg/m^3
z
y
x

Figure02.

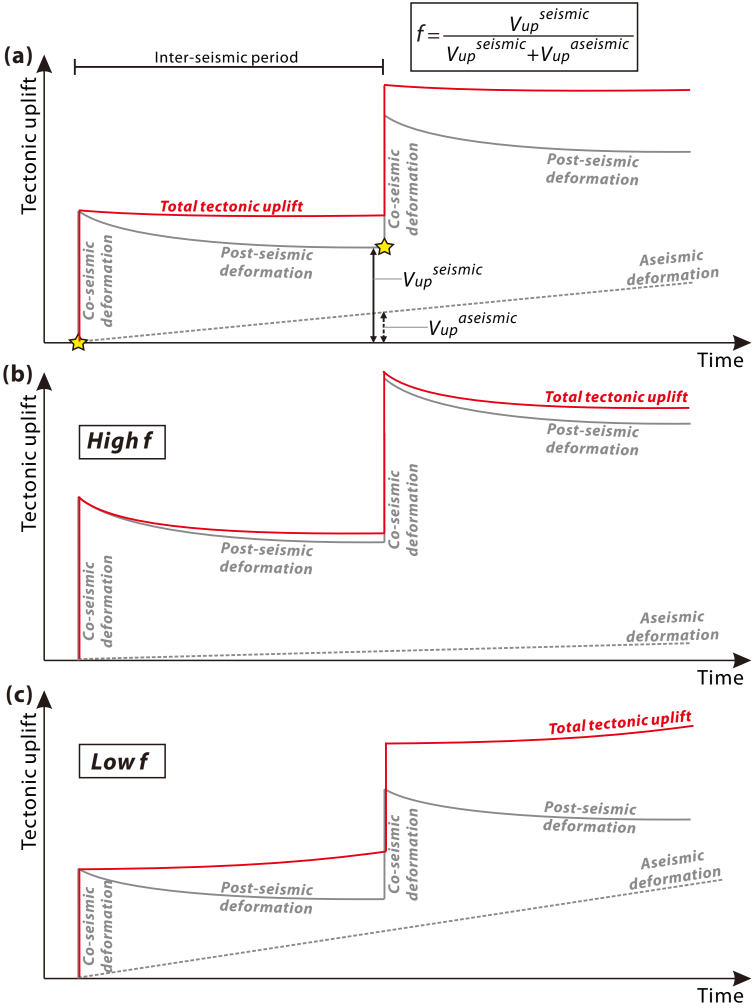

(a)
Inter-seismic period
$f = \frac{V_{up}^{seismic}}{V_{up}^{seismic} + V_{up}^{aseismic}}$
Tectonic uplift
Total tectonic uplift
Co-seismic deformation
Post-seismic deformation
Co-seismic deformation
Post-seismic deformation
$V_{up}^{seismic}$
Aseismic deformation
$V_{up}^{aseismic}$
Time
(b)
Tectonic uplift
High f
Total tectonic uplift
Post-seismic deformation
Co-seismic deformation
Post-seismic deformation
Co-seismic deformation
Aseismic deformation
Time
(c)
Tectonic uplift
Low f
Total tectonic uplift
Post-seismic deformation
Co-seismic deformation
Post-seismic deformation
Co-seismic deformation
Aseismic deformation
Time

Figure03.

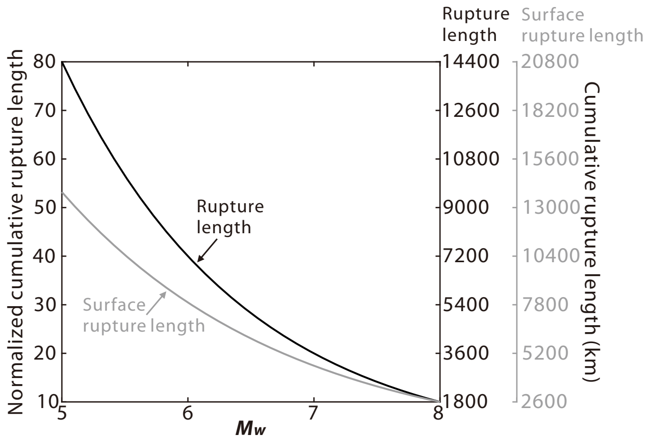
Rupture length
Surface rupture length
Normalized cumulative rupture length
Cumulative rupture length (km)
80
70
60
50
40
30
20
10
14400
12600
10800
9000
7200
5400
3600
1800
20800
18200
15600
13000
10400
7800
5200
2600
5
6
7
8
Mw
Rupture length
Surface rupture length

Figure04.

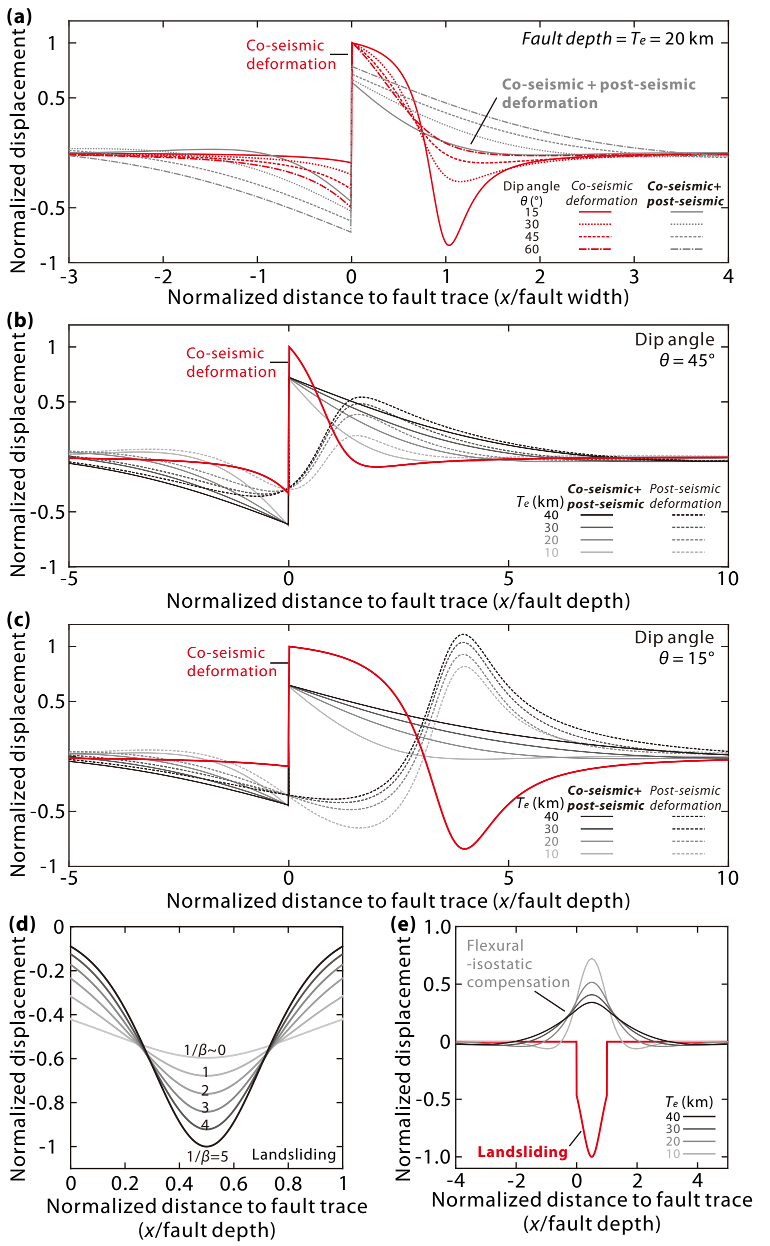

(a)
Fault depth = T_e = 20 km
Co-seismic deformation
Co-seismic + post-seismic deformation
Dip angle θ (°)
Co-seismic deformation
Co-seismic+ post-seismic
15
30
45
60
Normalized displacement
Normalized distance to fault trace (x/fault width)
(b)
Dip angle θ = 45°
Co-seismic deformation
T_e (km)
Co-seismic+ post-seismic
Post-seismic deformation
40
30
20
10
Normalized displacement
Normalized distance to fault trace (x/fault depth)
(c)
Dip angle θ = 15°
Co-seismic deformation
T_e (km)
Co-seismic+ post-seismic
Post-seismic deformation
40
30
20
10
Normalized displacement
Normalized distance to fault trace (x/fault depth)
(d)
1/β~0
1
2
3
4
1/β=5
Landsliding
Normalized displacement
Normalized distance to fault trace (x/fault depth)
(e)
Flexural -isostatic compensation
Landsliding
T_e (km)
40
30
20
10
Normalized displacement
Normalized distance to fault trace (x/fault depth)

Figure05.

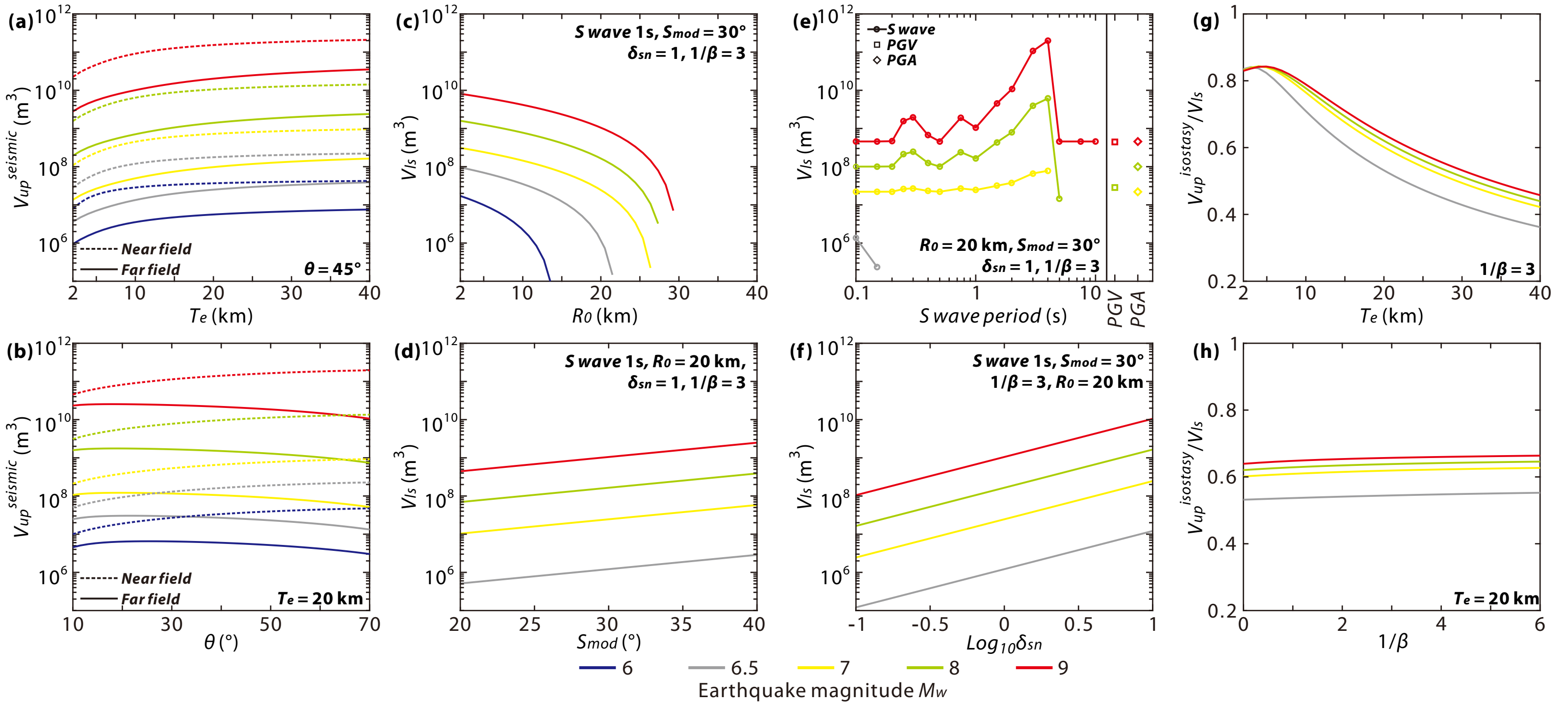
(a)
(b)
(c)
(d)
(e)
(f)
(g)
(h)
Near field
Far field
θ = 45°
Te = 20 km
Te (km)
θ (°)
Vup seismic (m3)
S wave 1s, Smod = 30°
δsn = 1, 1/β = 3
S wave 1s, R0 = 20 km,
Ro (km)
Smod (°)
Vls (m3)
S wave
PGV
PGA
R0 = 20 km, Smod = 30°
S wave period (s)
1/β = 3, R0 = 20 km
Log10δsn
Vup isostasy/Vls
1/β = 3
1/β
6
6.5
7
8
9
Earthquake magnitude Mw

Figure06.

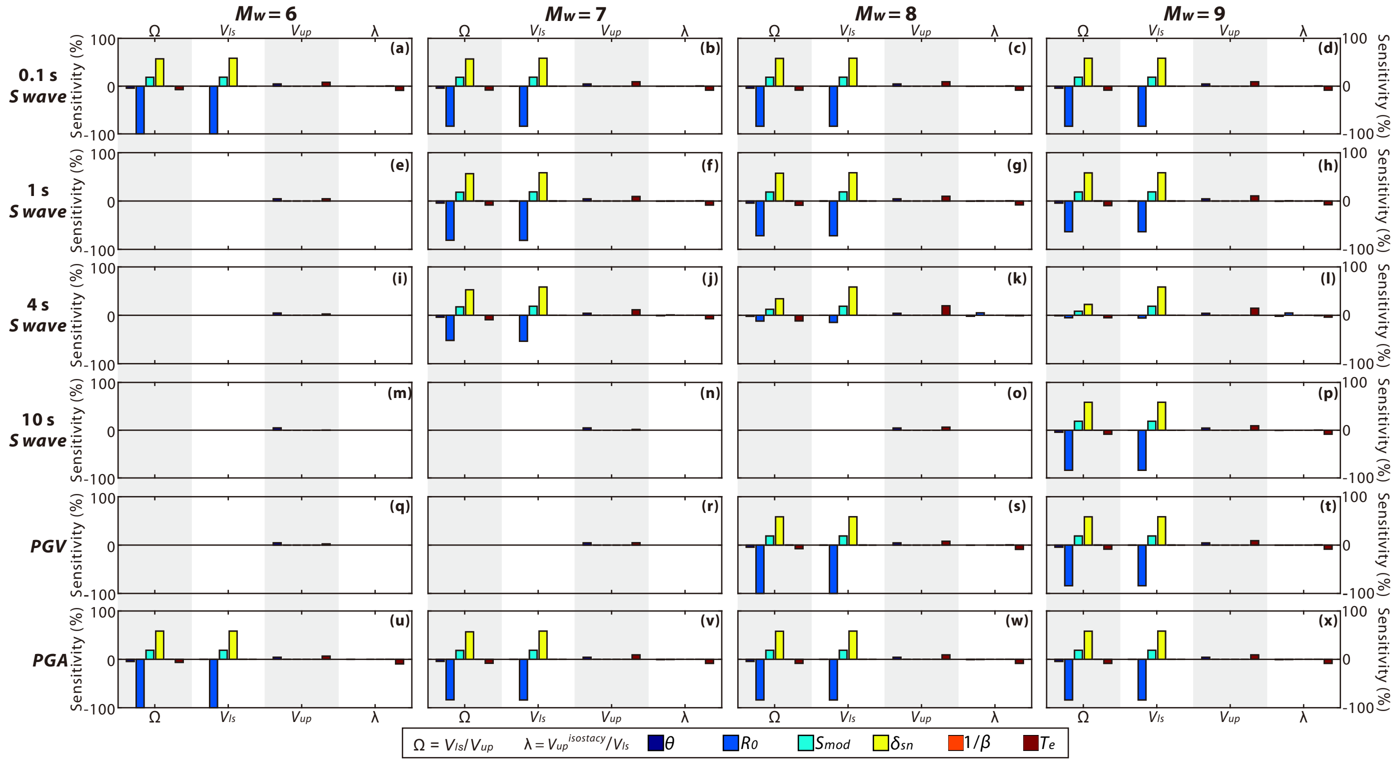

Mw = 6
Mw = 7
Mw = 8
Mw = 9
0.1 s S wave
1 s S wave
4 s S wave
10 s S wave
PGV
PGA
Sensitivity (%)
Ω
Vls
Vup
λ
Ω = Vls/Vup
λ = Vup^isostacy/Vls
θ
R0
Smod
δsn
1/β
Te

Figure07.

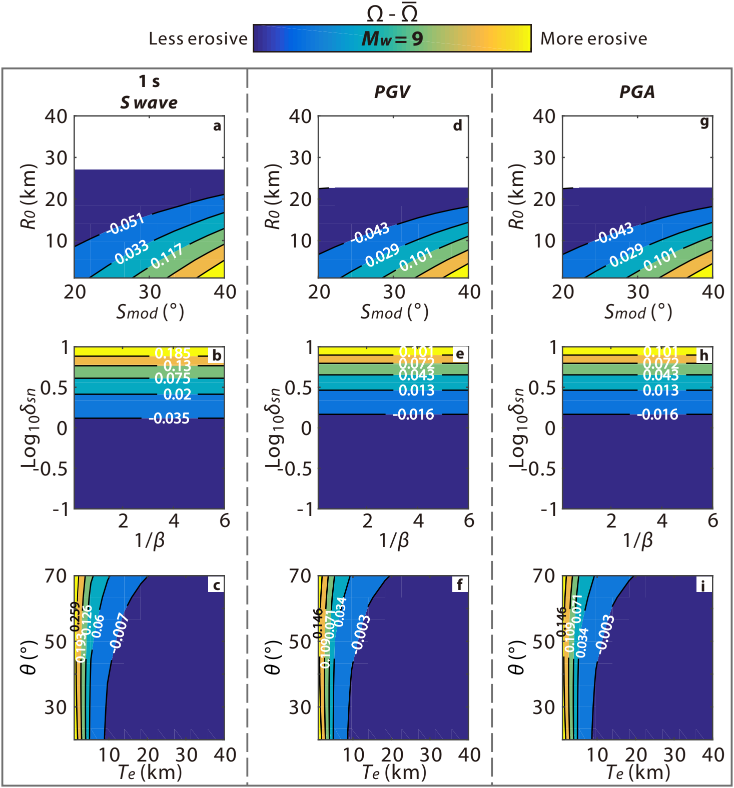

Ω - Ω̄
Less erosive
Mw = 9
More erosive
1 s
S wave
PGV
PGA
R0 (km)
Smod (°)
Log10δsn
1/β
θ (°)
Te (km)
a
b
c
d
e
f
g
h
i
-0.051
0.033
0.117
-0.043
0.029
0.101
0.185
0.13
0.075
0.02
-0.035
0.101
0.072
0.043
0.013
-0.016
0.259
0.193
0.126
0.06
-0.007
0.146
0.109
0.071
0.034
-0.003

Figure08.

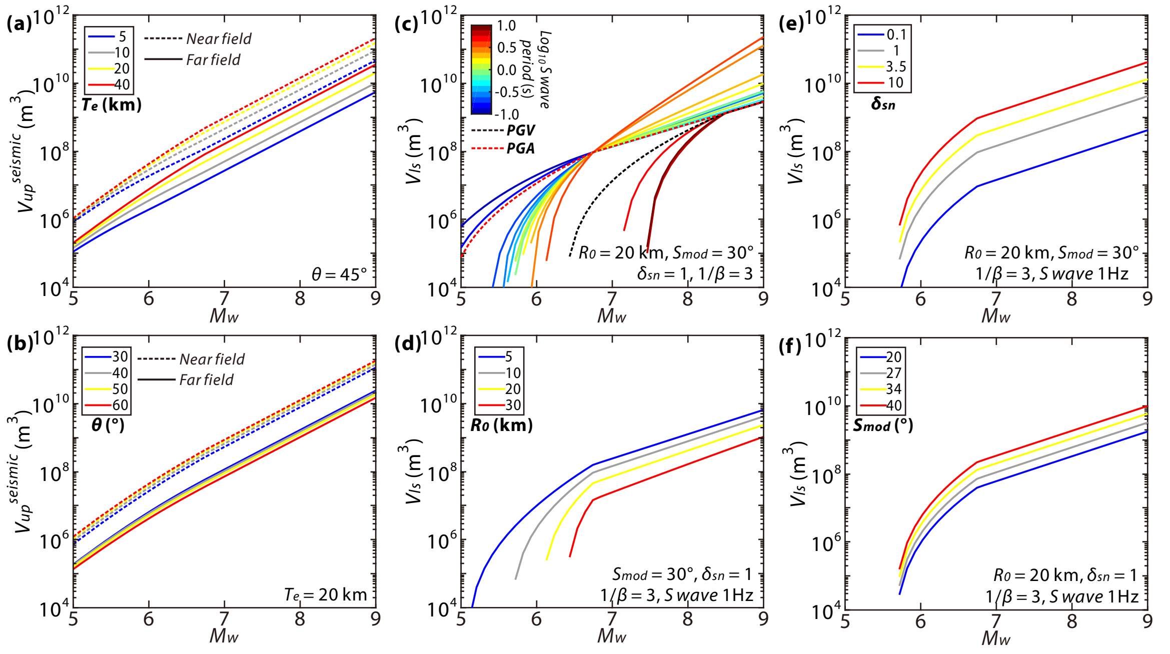

(a)
(b)
(c)
(d)
(e)
(f)
Near field
Far field
T_e (km)
5
10
20
40
$\theta = 45°$
θ (°)
30
40
50
60
$T_e = 20$ km
$V_{up}^{seismic}$ (m^3)
V_{ls} (m^3)
M_w
Log$_{10}$ S wave period (s)
1.0
0.5
0.0
-0.5
-1.0
PGV
PGA
$R_0 = 20$ km, $S_{mod} = 30°$
$\delta_{sn} = 1$, $1/\beta = 3$
R_0 (km)
5
10
20
30
$S_{mod} = 30°$, $\delta_{sn} = 1$
$1/\beta = 3$, S wave 1Hz
δ_{sn}
0.1
1
3.5
10
$R_0 = 20$ km, $S_{mod} = 30°$
$1/\beta = 3$, S wave 1Hz
S_{mod} (°)
20
27
34
40
$R_0 = 20$ km, $\delta_{sn} = 1$
$1/\beta = 3$, S wave 1Hz

Figure09.

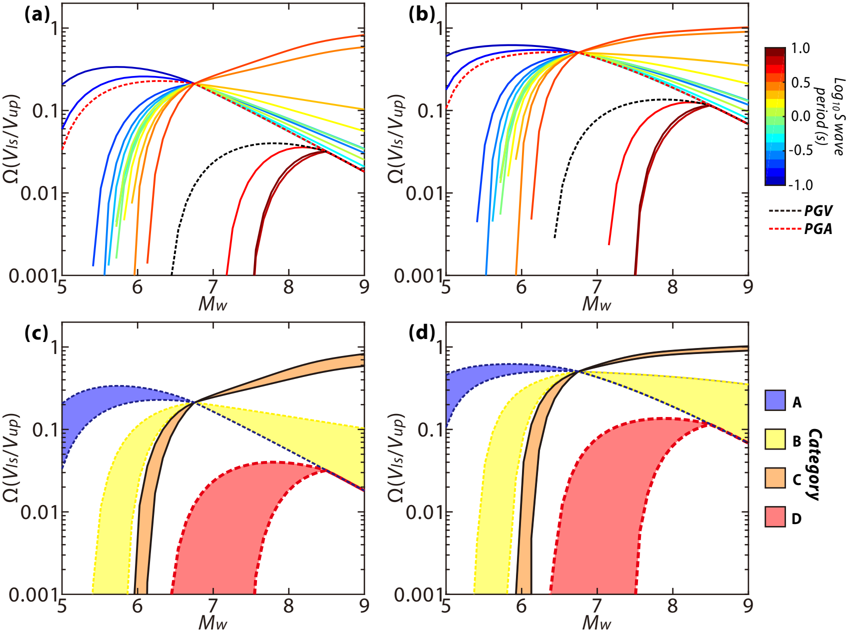
(a)
(b)
(c)
(d)
$\Omega(V_{ls}/V_{up})$
M_w
1
0.1
0.01
0.001
5
6
7
8
9
1.0
0.5
0.0
-0.5
-1.0
Log_{10} S wave period (s)
PGV
PGA
A
B
C
D
Category

Figure10.

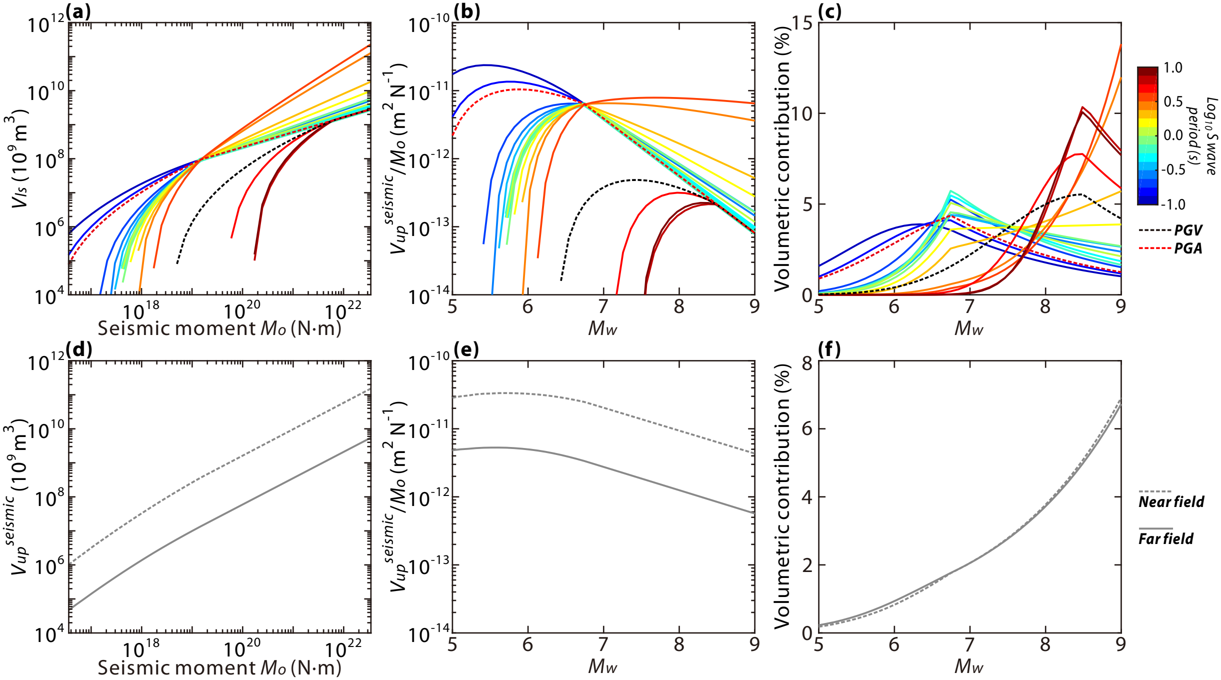

(a)
(b)
(c)
(d)
(e)
(f)
V_{ls} (10^9 m^3)
Seismic moment Mo (N·m)
$V_{up}^{seismic}/Mo$ (m^2 N^{-1})
Mw
Volumetric contribution (%)
Log_{10} S wave period (s)
PGV
PGA
$V_{up}^{seismic}$ (10^9 m^3)
Near field
Far field

Figure11.

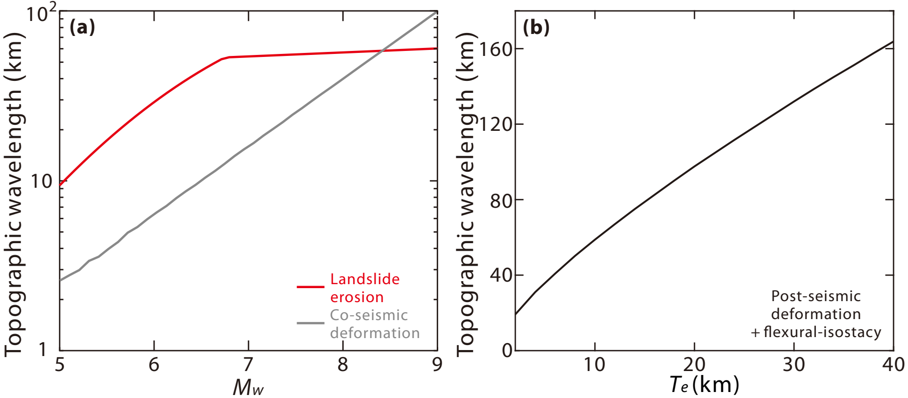

(a)
Topographic wavelength (km)
10^2
10
1
5
6
7
8
9
M_w
Landslide erosion
Co-seismic deformation
(b)
Topographic wavelength (km)
160
120
80
40
0
10
20
30
40
T_e (km)
Post-seismic deformation + flexural-isostacy

Figure12.

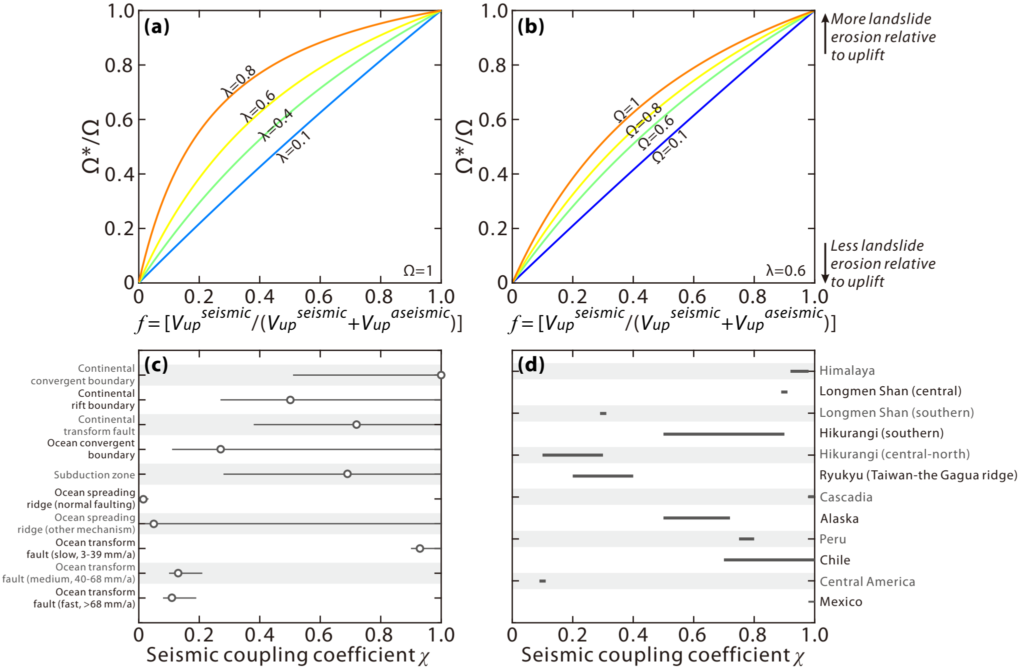

(a)
λ=0.8
λ=0.6
λ=0.4
λ=0.1
Ω=1
Ω*/Ω
f = [Vup^seismic/(Vup^seismic + Vup^aseismic)]
(b)
Ω=1
Ω=0.8
Ω=0.6
Ω=0.1
λ=0.6
More landslide erosion relative to uplift
Less landslide erosion relative to uplift
(c)
Continental convergent boundary
Continental rift boundary
Continental transform fault
Ocean convergent boundary
Subduction zone
Ocean spreading ridge (normal faulting)
Ocean spreading ridge (other mechanism)
Ocean transform fault (slow, 3-39 mm/a)
Ocean transform fault (medium, 40-68 mm/a)
Ocean transform fault (fast, >68 mm/a)
Seismic coupling coefficient χ
(d)
Himalaya
Longmen Shan (central)
Longmen Shan (southern)
Hikurangi (southern)
Hikurangi (central-north)
Ryukyu (Taiwan-the Gagua ridge)
Cascadia
Alaska
Peru
Chile
Central America
Mexico
Seismic coupling coefficient χ

Figure13.

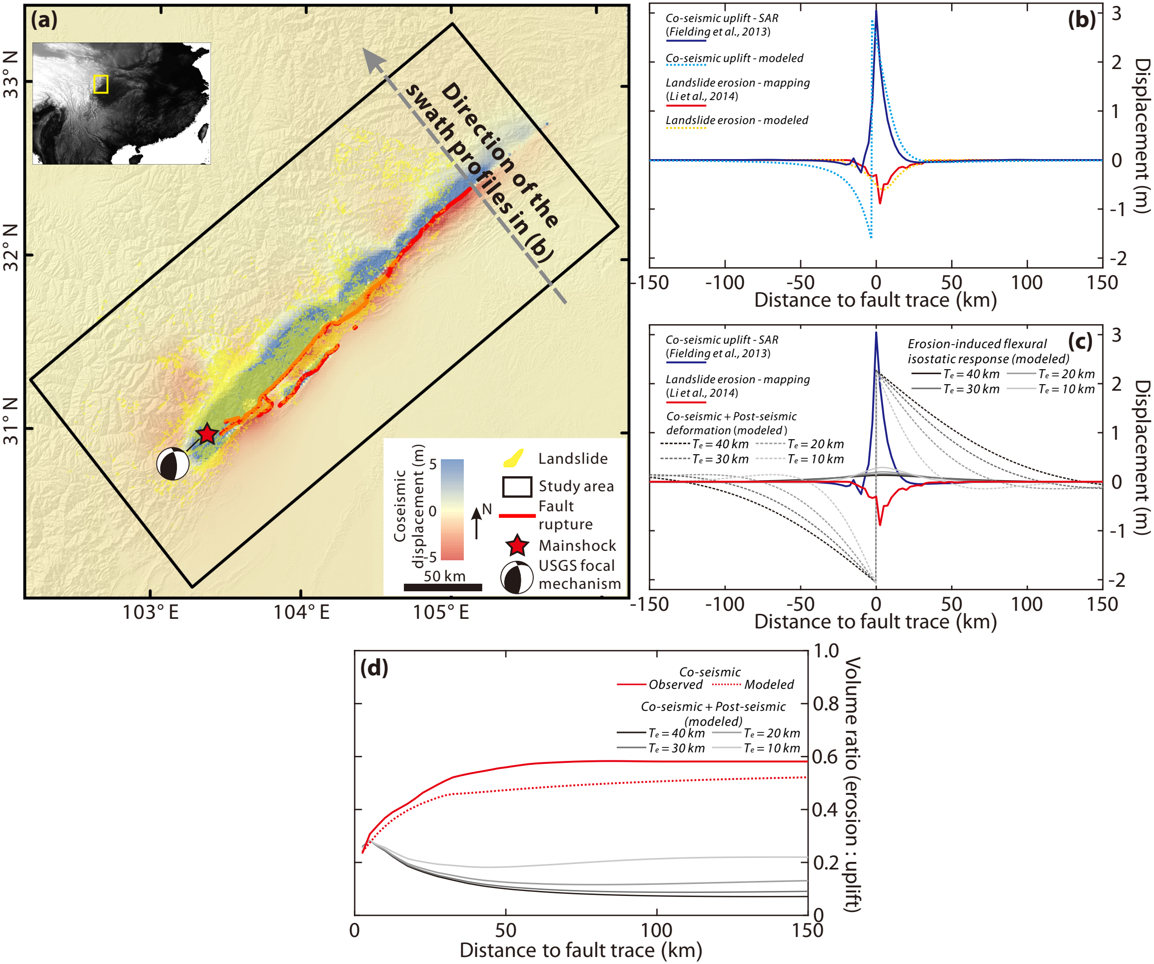

(a)
33° N
32° N
31° N
103° E
104° E
105° E
Direction of the swath profiles in (b)
Coseismic displacement (m)
5
0
-5
N
50 km
Landslide
Study area
Fault rupture
Mainshock
USGS focal mechanism
(b)
Co-seismic uplift - SAR (Fielding et al., 2013)
Co-seismic uplift - modeled
Landslide erosion - mapping (Li et al., 2014)
Landslide erosion - modeled
Displacement (m)
Distance to fault trace (km)
(c)
Co-seismic uplift - SAR (Fielding et al., 2013)
Landslide erosion - mapping (Li et al., 2014)
Co-seismic + Post-seismic deformation (modeled)
T_e = 40 km
T_e = 20 km
T_e = 30 km
T_e = 10 km
Erosion-induced flexural isostatic response (modeled)
Displacement (m)
Distance to fault trace (km)
(d)
Co-seismic
Observed
Modeled
Co-seismic + Post-seismic (modeled)
T_e = 40 km
T_e = 20 km
T_e = 30 km
T_e = 10 km
Volume ratio (erosion : uplift)
Distance to fault trace (km)

Figure14.

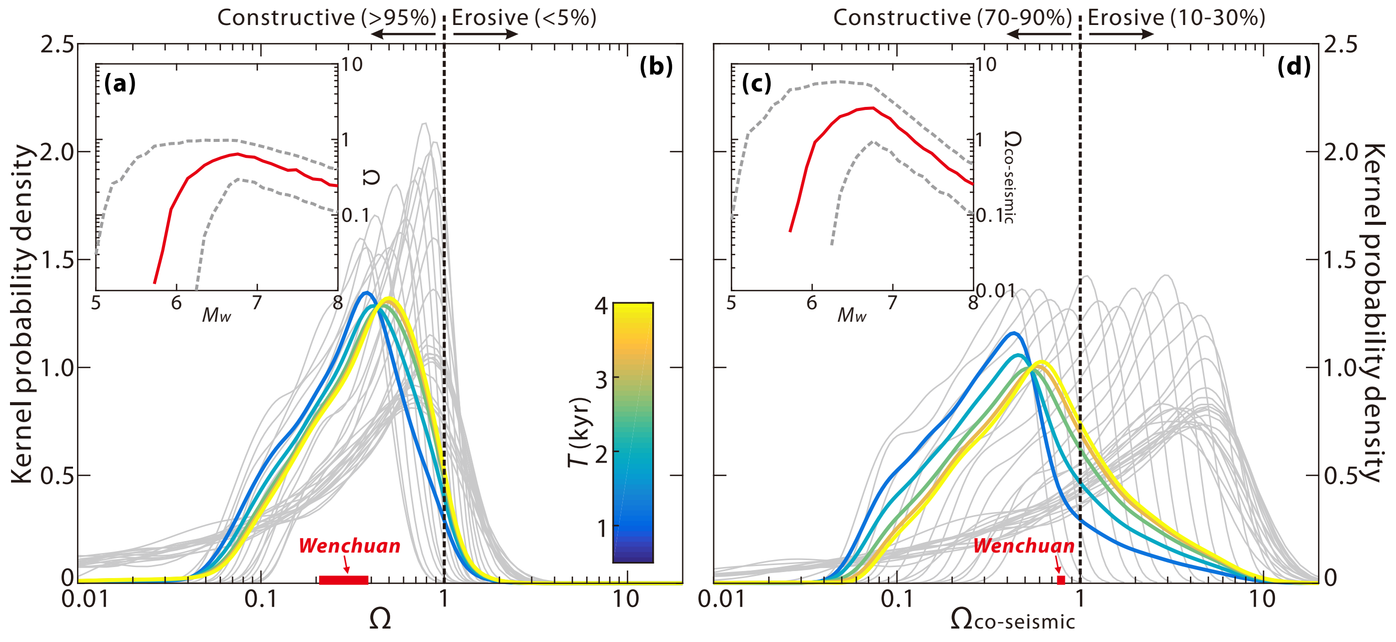

Constructive (>95%)
Erosive (<5%)
Constructive (70-90%)
Erosive (10-30%)
(a)
(b)
(c)
(d)
Kernel probability density
Ω
Ωco-seismic
Mw
T (kyr)
Wenchuan
Wenchuan

FigureA1.

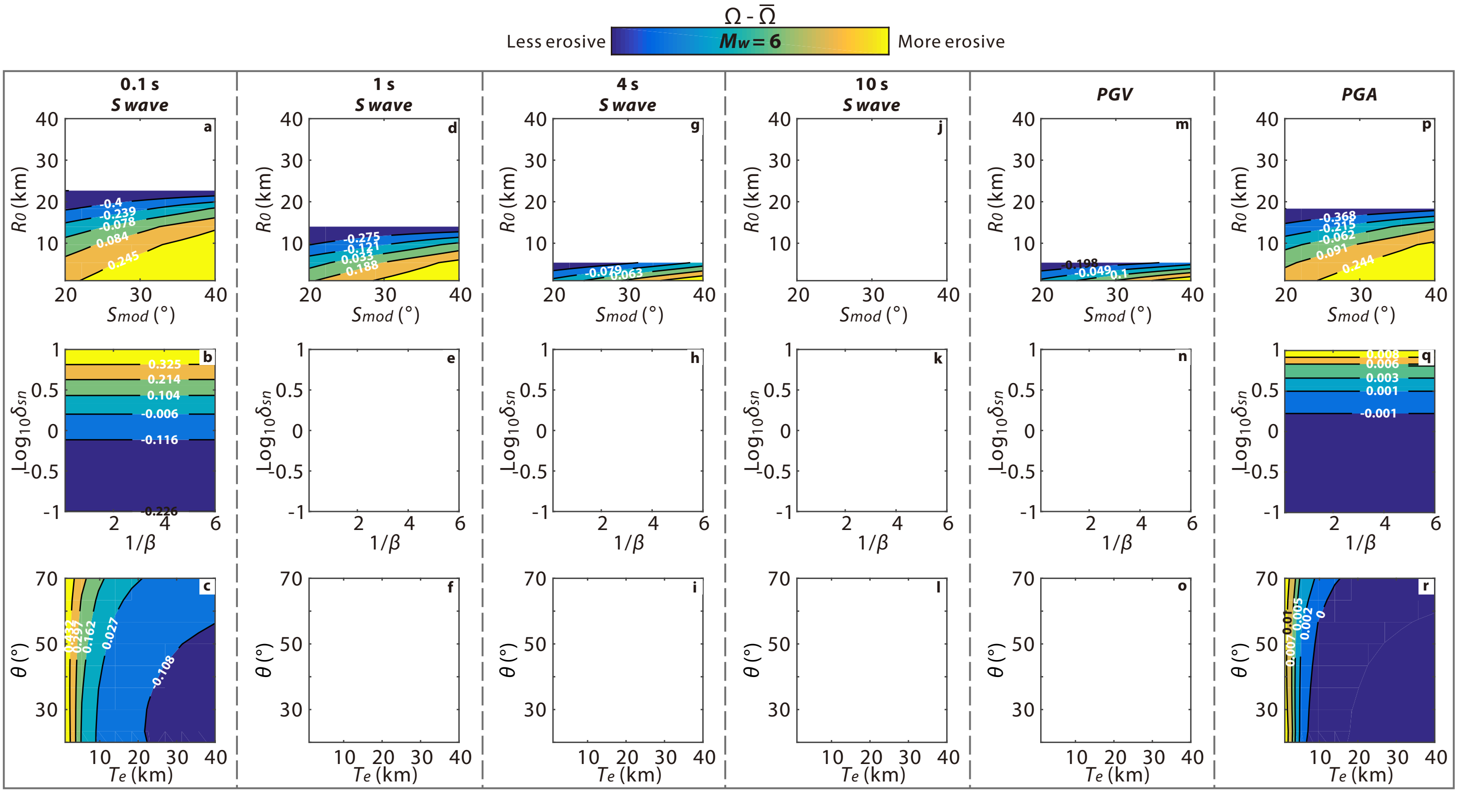

Ω - Ω̄
Less erosive
Mw = 6
More erosive
0.1 s
S wave
1 s
S wave
4 s
S wave
10 s
S wave
PGV
PGA
R0 (km)
Smod (°)
Log10δsn
1/β
θ (°)
Te (km)

FigureA2.

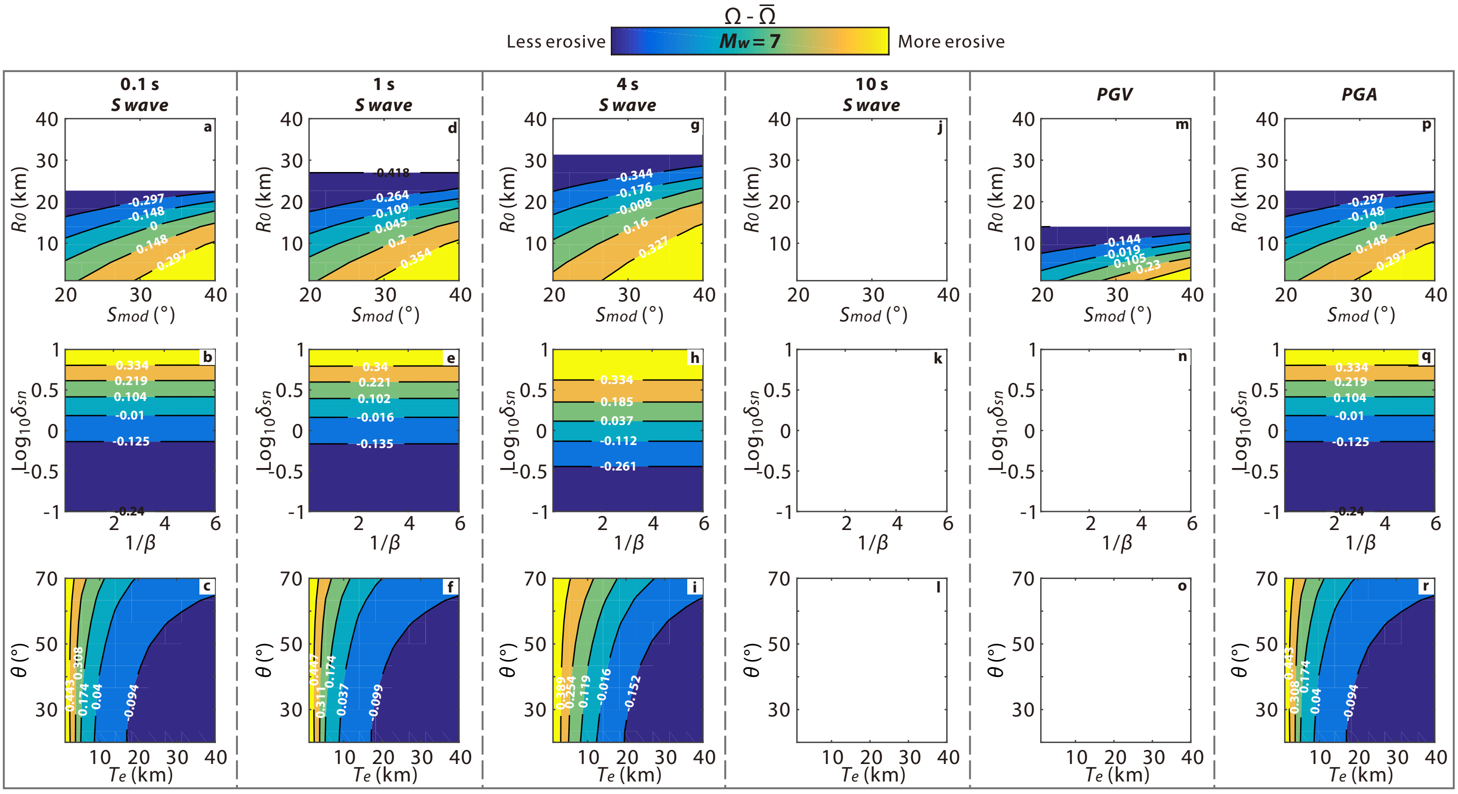
Ω - Ω̄
Less erosive
Mw = 7
More erosive
0.1 s
S wave
1 s
S wave
4 s
S wave
10 s
S wave
PGV
PGA
R0 (km)
Smod (°)
Log10δsn
1/β
θ (°)
Te (km)
a
b
c
d
e
f
g
h
i
j
k
l
m
n
o
p
q
r

FigureA3.

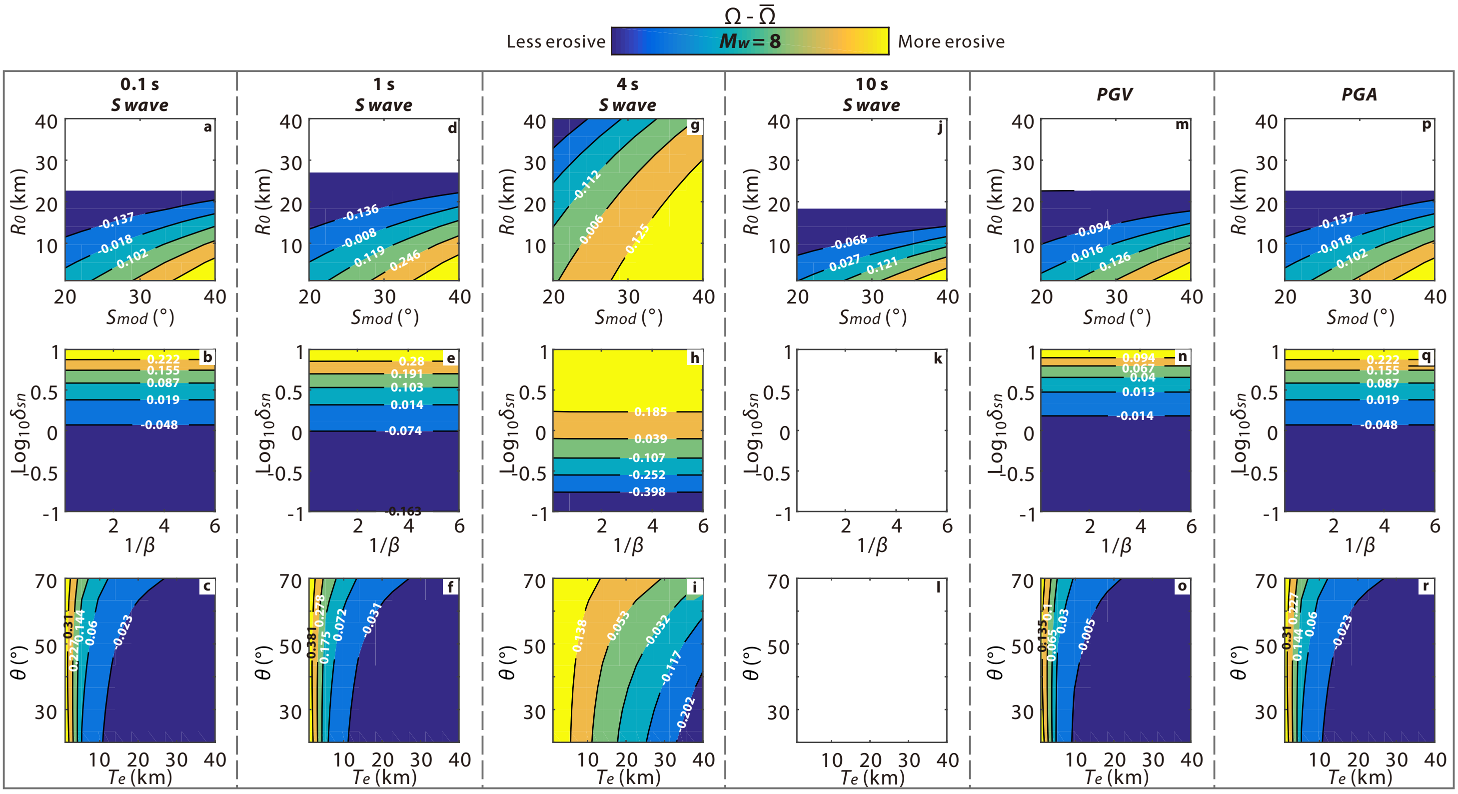

Ω - Ω̄
Less erosive
Mw = 8
More erosive
0.1 s
S wave
1 s
S wave
4 s
S wave
10 s
S wave
PGV
PGA
R0 (km)
Smod (°)
Log10δsn
1/β
θ (°)
Te (km)
a
b
c
d
e
f
g
h
i
j
k
l
m
n
o
p
q
r

FigureA4.

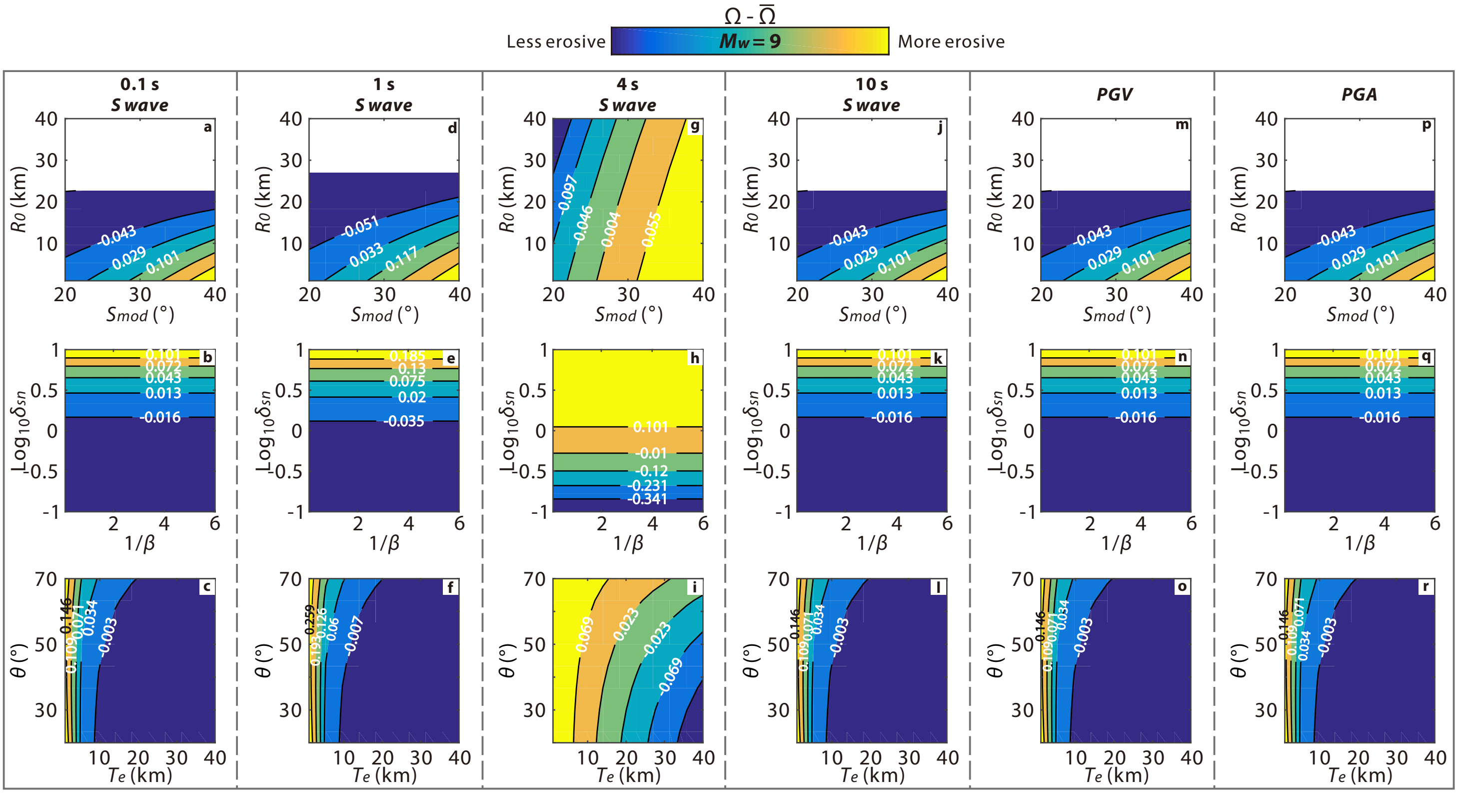
Ω - Ω̄
Less erosive
Mw = 9
More erosive
0.1 s S wave
1 s S wave
4 s S wave
10 s S wave
PGV
PGA
R0 (km)
Smod (°)
Log10δsn
1/β
θ (°)
Te (km)